CHARACTERIZATION AND VISIBLE-LIGHT PHOTOCATALYTIC ACTIVITY OF METAL OXIDE/BISMUTH VANADATE POWDER SYNTHESIZED BY AN ETHANOL-ASSISTED HYDROTHERMAL METHOD

PRADUDNET KETWONG

A DISSERTATION SUBMITTED IN PARTIAL FULFILLMENT
OF THE REQUIREMENTS FOR THE DEGREE OF
DOCTOR OF PHILOSOPHY IN APPLIED CHEMISTRY
GRADUATE SCHOOL MAEJO UNIVERSITY
2017

CHARACTERIZATION AND VISIBLE-LIGHT PHOTOCATALYTIC ACTIVITY OF METAL OXIDE/BISMUTH VANADATE POWDER SYNTHESIZED BY AN ETHANOL-ASSISTED HYDROTHERMAL METHOD

PRADUDNET KETWONG

THIS DISSERTATION HAS BEEN APPROVED IN PARTIAL FUFILLMENT
OF THE REQUIREMENTS FOR THE DEGREE OF DOCTOR OF PHILOSOPHY
IN APPLIED CHEMISTRY

APPROVED BY

Advisory Committee

Chair .....
(Assistant Professor Dr. Pusit Pookmanee)
10 / November / 2017

Committee .....
(Assistant Professor Dr. Supaporn Sangsrichan)
10 / November / 2017

Committee .....
(Dr. Pinit Kidkhunthod)
10 / November / 2017

Program Chair, Doctor of Philosophy in Applied Chemistry .....
(Assistant Professor Dr. Supaporn Sangsrichan)
10 / November / 2017

CERTIFIED BY GRADUATE SCHOOL .....
(Associate Professor Dr. Kriangsak Mengamphan)
Dean of Graduate School
10 / November / 2017

Title	CHARACTERIZATION AND VISIBLE LIGHT PHOTOCATALYTIC ACTIVITY OF METAL OXIDE/BISMUTH VANADATE POWDER SYNTHESIZED BY AN ETHANOL-ASSISTED HYDROTHERMAL METHOD
Author	Miss Pradudnet Ketwong
Degree	Doctor of philosophy in Applied Chemistry
Advisor Committee Chairperson	Assistant Professor Dr. Pusit Pookmanee

ABSTRACT

Bismuth vanadate ($BiVO_4$) is a semiconductor with a localized electronic structure that facilitates photocatalysis under visible light. The efficiency of such photocatalyst is not high due to physical and chemical properties limitations. This research presents the results of an ethanol-assisted hydrothermal synthesis of $BiVO_4$ as well as the effects of the $BiVO_4$ synthesis conditions; such as pH, temperature and reaction time, that affect the decomposition capacity of methyl orange (MO) and oxygen production. It was found that pH, reaction temperature and reaction time affects directly on the crystalline structure and crystallinity of $BiVO_4$. Single monoclinic structure could be synthesized at pH 7 and 8, and the crystallinity was increased by increasing the reaction temperature and reaction time. In addition, the parameters also contributed significantly to the morphology of $BiVO_4$ particles, including particle size, surface area, electronic structure and arrangement of atoms in the crystal structure. These characteristics significantly affected the photocatalytic efficiency of the $BiVO_4$. The $BiVO_4$ with monoclinic structure, high crystallinity, a great surface area and a distortion of the V–O bond is the most active photocatalyst for photocatalysis under visible light. Moreover, stability and sustainability of the photocatalytic rate are also important. Bismuth vanadate/bismuth tungstate ($BiVO_4/Bi_2WO_6$) composites in various molar ratios were synthesized in the same way as the $BiVO_4$. Photocatalytic activity results demonstrated that $BiVO_4$ powder had the highest efficiency. It was also found that, the $BiVO_4/Bi_2WO_6$ composites activities were

based on the fraction of $BiVO_4$ without synergetic effect. This finding was supported by results of energy resolved distribution of electron traps. However, after calcination at 600 °C for 4 h, photocatalytic oxygen liberation was enhanced by the combination of $BiVO_4$ (80%) and Bi_2WO_6 (20%) followed by calcination. Furthermore, the calcined $BiVO_4/Bi_2WO_6$ composite had superior advantages over $BiVO_4$ in stability and reusability. Based on this research, the $BiVO_4$ with highly efficiency visible-light absorption has been developed for future photocatalyst in order to overcome its disadvantages; such as low stability and rapid electron-hole recombination rate under light irradiation, which decrease photocatalytic activity of the $BiVO_4$.

Keywords: bismuth vanadate, bismuth tungstate, photocatalysis, stabilization

ชื่อเรื่อง คุณลักษณะเฉพาะและความสามารถในการเร่งปฏิกิริยาด้วยแสงของผงโลหะออกไซด์/บิสมัธวานาเดตที่สังเคราะห์ด้วยวิธีเอทานอลร่วมกับไฮโดรเทอร์มอล

ชื่อผู้เขียน นางสาวประดุจเนตร เกตุวงค์

ชื่อปริญญา ปรัชญาดุษฎีบัณฑิต สาขาวิชาเคมีประยุกต์

อาจารย์ที่ปรึกษาหลัก ผู้ช่วยศาสตราจารย์ ดร.ภูสิต ปุกมณี

บทคัดย่อ

บิสมัธวานาเดต ($BiVO_4$) เป็นสารกึ่งตัวนำที่มีคุณสมบัติทางโครงสร้างอิเล็กทรอนิกส์เอื้อต่อการเร่งปฏิกิริยาด้วยแสงภายใต้แสงวิสิเบิล ประสิทธิภาพของตัวเร่งปฏิกิริยาดังกล่าวไม่สูงนักเนื่องด้วยข้อจำกัดของคุณสมบัติทางกายภาพและทางเคมี งานวิจัยนี้นำเสนอผลการศึกษาการสังเคราะห์ $BiVO_4$ ด้วยวิธีไฮโดรเทอร์มอลร่วมกับเอทานอล รวมทั้งผลของสภาวะในการสังเคราะห์ $BiVO_4$ ได้แก่ ค่าพีเอช อุณหภูมิและเวลาในการทำปฏิกิริยาที่ส่งผลต่อความสามารถในการสลายตัวของเมทิลออเรนจ์ (MO) และการผลิตออกซิเจน พบว่า ค่าพีเอช อุณหภูมิและเวลาในการทำปฏิกิริยาส่งผลโดยตรงกับรูปแบบโครงสร้างผลึกและความเป็นผลึกของ $BiVO_4$ กล่าวคือ โครงสร้างแบบโมโนคลินิกสามารถสังเคราะห์ได้ที่ค่าพีเอช เท่ากับ 7 และ 8 และความเป็นผลึกเพิ่มขึ้นเมื่อเพิ่มอุณหภูมิและเวลาในการทำปฏิกิริยา นอกจากนี้พารามิเตอร์ดังกล่าวยังส่งผลอย่างชัดเจนต่อลักษณะสัณฐานวิทยาของอนุภาค $BiVO_4$ รวมถึงขนาดอนุภาค พื้นที่ผิว โครงสร้างทางอิเล็กทรอนิกส์และการจัดเรียงตัวของอะตอมในโครงสร้างผลึกอีกด้วย ซึ่งคุณลักษณะเฉพาะต่าง ๆ นี้ส่งผลอย่างมีนัยสำคัญต่อประสิทธิภาพในการเร่งปฏิกิริยาด้วยแสงของ $BiVO_4$ โดย $BiVO_4$ ที่มีโครงสร้างแบบโมโนคลินิก มีความเป็นผลึกสูง มีพื้นที่ผิวมากและมีการบิดตัวของพันธะ V–O มากเป็นตัวเร่งปฏิกิริยาด้วยแสงที่เร่งปฏิกิริยาด้วยแสงภายใต้แสงวิสิเบิลได้ดีที่สุด นอกเหนือจากนี้ ความเสถียรและการคงอัตราการเร่งปฏิกิริยาของตัวเร่งปฏิกิริยาด้วยแสงก็เป็นสิ่งสำคัญด้วย บิสมัธวานาเดต/บิสมัธทังสเตต ($BiVO_4/Bi_2WO_6$) คอมโพสิตในอัตราส่วนโดยโมลต่าง ๆ ถูกสังเคราะห์โดยวิธีเดียวกันกับ $BiVO_4$ ผลความสามารถในการเร่งปฏิกิริยาด้วยแสงแสดงให้เห็นว่าผง $BiVO_4$ มีประสิทธิภาพในการเร่งปฏิกิริยาด้วยแสงสูงสุด นอกจากนี้ยังพบว่าความสามารถในการเร่งปฏิกิริยาของ $BiVO_4/Bi_2WO_6$ คอมโพสิตนั้นขึ้นอยู่กับสัดส่วนของ $BiVO_4$ โดยไม่มีผลกระทบจากการทำงานร่วมกัน ซึ่งผลการศึกษานี้ได้รับการสนับสนุนจากผลการวิเคราะห์การกระจายของกับดักพลังงาน อย่างไรก็ตามหลังจากการเผาแคลไซน์ที่อุณหภูมิ 600 องศาเซลเซียสเป็นเวลา 4 ชั่วโมงแล้ว ปฏิกิริยาการสังเคราะห์ออกซิเจนเกิดดีที่สุดจากการรวมกันของ $BiVO_4$ (80%)

และ Bi_2WO_6 (20%) หลังการเผาแคลไซน์ นอกเหนือจากนี้ในการทดสอบการตกตะกอนและการใช้ซ้ำ $BiVO_4/Bi_2WO_6$ คอมโพสิตที่ได้รับการเผามีข้อได้เปรียบเหนือกว่า $BiVO_4$ อีกด้วย จากงานวิจัยนี้ $BiVO_4$ ซึ่งมีประสิทธิภาพในการดูดกลืนแสงช่วงวิสิเบิลสูงได้รับการพัฒนาขึ้นเพื่อเป็นแนวทางในการสร้างตัวเร่งปฏิกิริยาด้วยแสงในอนาคตเพื่อเอาชนะข้อจำกัดด้านต่าง ๆ เช่น ความเสถียรต่ำและอัตราการรวมตัวของอิเล็กตรอน–โฮลอย่างรวดเร็วภายใต้การฉายแสงซึ่งจะลดความสามารถในการเร่งปฏิกิริยาของ $BiVO_4$

คำสำคัญ: บิสมัธวานาเดต, บิสมัธทังสเตต, การเร่งปฏิกิริยาด้วยแสง, ความเสถียร

ACKNOWLEDGEMENTS

I would like to express my deepest appreciation to Assistant Professor Dr. Pusit Pookmanee, for his suggestion, assistant and encouragement throughout my research. My gratitude is also expressed to Associate Professor Dr. Siwaporn Meejoo Smith, Assistant Professor Supaporn Sangsrichan, Dr. Tanin Tanguaram and Dr. Pinit Kidkhunthod for their insightful comments and suggestions in completion of the thesis. My grateful acknowledgement is expressed to Associate Professor Dr. Sukon Phanichphant, the external examiner for her comments and suggestions.

I would like to express my sincere gratitude to Professor Bunsho Ohtani for great opportunity to work with him and staffs of Ohtani's laboratory at the Institute for Catalysis (ICAT), Hokkaido University, Japan. I greatly appreciate his encouragements, financial supports for poster and oral presentations, kind suggestions and valuable guidance on the research.

I am thankful to the Department of Chemistry, Faculty of Science, Maejo University for the opportunity to provide teaching assistantship. I am also very grateful for the financial support provided by the Science Achievement Scholarship of Thailand (SAST) and analytical instruments supported by Synchrotron light research institute (SLRI); Beamline 5.2, Nakhon Ratchasima, Department of Chemistry, Mahidol University, Bangkok and ICAT.

My sincere thankfulness is expressed to all staffs in; Applied Chemistry, Ohtani's Laboratory and Nano Material Chemistry MJU Laboratory; for their friendship, good messages and kind help for learning and research. In addition, I also would like to extend my sincere gratitude to all the staff members of the Department of Chemistry and Faculty of Graduate School for their generous help.

Finally, I would like to express my deepest gratitude to my parents and my sister for their understanding, encouragement and support throughout my life.

Pradudnet Ketwong

November 2017

TABLE OF CONTENTS

LIST OF TABLES

LIST OF FIGURES

Figure Page

Figure Page

Figure Page

LIST OF ABBREVIATIONS

Å	Angstrom
BET	Brunauer-Emmett-Teller
C	A photocatalyst
*C**	An excited photocatalyst
cm^2	Square centimeter
C_t	Concentration at time
C_0	Initial concentration
°C	Degrees Celsius
CB	Conduction band
CBB	Conduction band bottom
c-	Calcined
cfu	Colony-forming unit
D	Crystalline size
E_g	Optical band gap of the semiconductor
E_{CB}	Conduction band energy
E_{VB}	Valence band energy
ET	Ethanol-assisted hydrothermal
EtOH	Ethanol
EDTA	Ethylenediaminetetraacetic acid
e^-	Electron
eV	Electron volt
g	grams
Hg	Mercury
HT	Hydrothermal
h	Hour
$h\nu$	Photon energy
h^+	Hole
JCPDS	Joint Committee on Powder Diffraction Standards

K-M	Kubelka-Munk
kV	Kilovolt
L	liter
LED	Light-emitting diode
M	Mole per liter
MO	Methyl Orange
mg	Milligram
min	Minute
mL	Milliliter
mm	Millimeters
mmol	Millimole
mol	Mole
ms-	Monoclinic scheelite
m^2	Square meter
nm	Nanometer
NHE	Normal hydrogen electrode
ppm	Parts per million
R	Reflectance
RhB	Rhodamine B
RHE	Reversible hydrogen electrode
S	Substrate
$S^{\bullet+}$	Oxidized substrate
$S^{\bullet}$	Substrate radical
sec	Second (unit of time)
SEM	Scanning Electron Microscopy
SSA	Specific Surface Area
TCD	Thermal conductivity detector
t	Time
ts-	Tetragonal scheelite
tz-	Tetragonal zircon
UV	Ultraviolet

UV-Vis	Ultraviolet-Visible
V	Volume
VB	Valence band
VBT	Valence band top
Xe	Xenon
XRD	X-ray diffraction
W	Watt
α	Absorbance coefficient
β	The peak width measured at half height measured in radius
λ	Wavelength
μmol	Micromole
θ	The Bragg angle for the reflection
ν_{as}	Frequency asymmetric
ν_{s}	Frequency symmetric
ζ(a)	Degree of coincidence

CHAPTER 1

INTRODUCTION

Photocatalysis or photocatalytic reaction is a promising way for clean renewable energy (Chen *et al.*, 2017). It has received increased attention by many researchers around the world and has been applied in environmental treatment (Zhang *et al.*, 2010) and energy production (Ke *et al.*, 2009). The reaction can be driven by natural sunlight absorption of a photocatalyst and give small molecules such as oxygen (O_2), carbon dioxide (CO_2) and water (H_2O) as the final products. This clean chemical-reaction activity will be enhanced by a suitable photocatalyst. A famous photocatalyst, titania (titanium dioxide, TiO_2) semiconductor, has been reported its performance as a highly-active photocatalyst under ultraviolet (UV) light irradiation (Fujishima *et al.*, 2000). However, pristine TiO_2 cannot effectively absorb sunlight due to wide bang gap energy (E_g) of 3.2 eV and the entire solar energy observed on earth is only about 6% of UV light (Fig. 1).

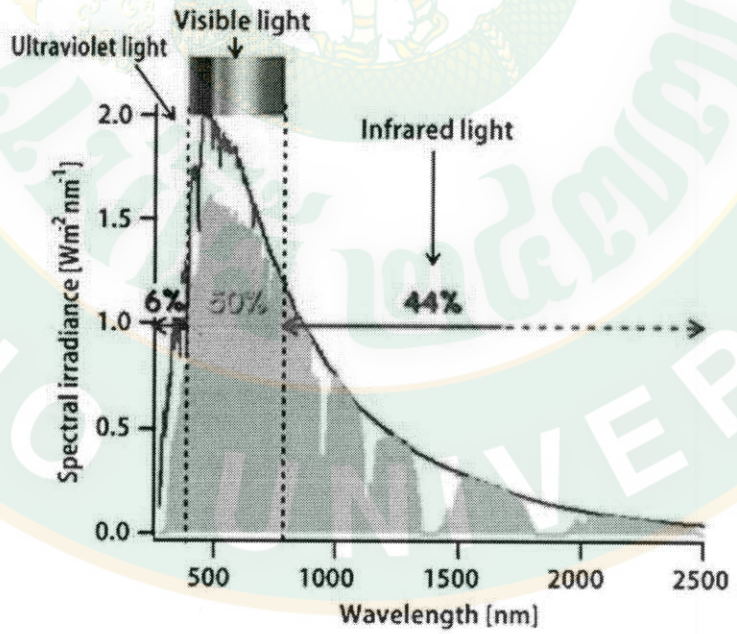

Figure 1 Solar radiation spectrum (Misawa, 2017).

Nevertheless, some visible light-responsive photocatalysts have been proposed and studied. Visible-light active photocatalysts can be spontaneously effective under natural sunlight such as bismuth vanadate ($BiVO_4$) (Lai *et al.*, 2014) and bismuth tungstate (Bi_2WO_6) (Kudo and Hijii, 1999) due to their narrow E_g. Although a relatively narrow E_g of the $BiVO_4$ (2.4 eV) and Bi_2WO_6 (2.7 eV) leading to high photoabsorption performance under visible light, these gaps accelerate generated electron/positive-hole recombination rate which reduces photocatalytic activity. Moreover, morphology of a photocatalyst's particle also plays important role in its photocatalytic activity. Hence, it is necessary to modify the $BiVO_4$ and Bi_2WO_6 photocatalysts for more stable and higher activity photocatalysts.

1. Background and signification of the Research

1.1 Principal and application of photocatalysis

An acceleration of chemicals conversion by solar energy using a photocatalyst is called "photocatalysis". Well-known photocatalytic reactions are photodegradation of organic compounds and water splitting photocatalysis which oxygen and/or hydrogen can be produced (Fan *et al.*, 2012; Yang *et al.*, 2013). General photocatalysis process is shown in Fig. 2. Firstly, (1) sufficient absorption of light ($h\nu$) by surface of a semiconductor photocatalyst (C) generates hole (h^+) at valence band (VB) and electron (e^-) at conduction band (CB). Then, (2) h^+ and e^- migrate to the semiconductor's surface allowing (3) redox reaction of substrates (S) with h^+ and e^- at VB and CB, respectively. Theoretically, reduction will occurs if redox potential of CB is more negative than the substrates while oxidation reaction will occurs if redox potential of VB is more positive than that of substrates. Meanwhile, a simple recombination of electron-hole pair can be happened (4) with releasing of thermal energy. This process reduces amount of separated h^+ and e^- for redox reaction so that photocatalytic activity is also decreased.

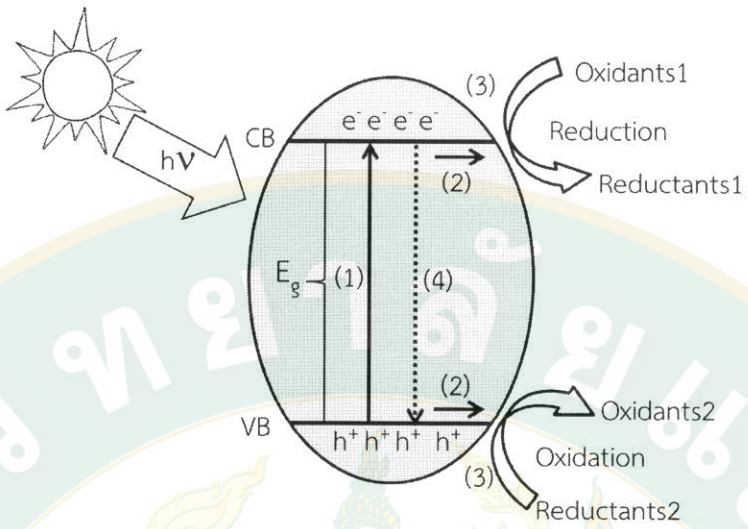

Figure 2 Schemes of photocatalysis process on a semiconductor photocatalyst: (1) photoinduced electron-hole generation, (2) migration, (3) redox reaction on photocatalyst surface and (4) electron-hole recombination.

In principle, oxidation reaction for photodegradation of organic compounds can take place in two ways: directly oxidation of organic material by C and oxidation of water for formation of highly reactive hydroxyl radicals ($OH^{\bullet}$) as show as follow equation (Jackson and Hargreaves, 2009):

(Light absorption) $C + h\nu(\geq E_g) \longrightarrow C^*(h^+ + e^-)$

(Oxidation) $S + h^+ \longrightarrow S^{\bullet+} \longleftrightarrow S^{\bullet} + H^+$

$H_2O + h^+ \longrightarrow OH^{\bullet} + H^+$

Main reduction occurring on C surface is reduction of oxygen which give superoxide radicals ($O_2^{\bullet-}$) as a product. The $O_2^{\bullet-}$ can give rise of additional $OH^{\bullet}$ as showed in these equation (Jackson and Hargreaves, 2009):

(Reduction) $O_2 + e^- \longrightarrow O_2^{\bullet-}$

$O_2^{\bullet-} + H^+ \longleftrightarrow HO_2^{\bullet}$

An example for water splitting photocatalysis is showed as follows equation (Kim and Lee, 2014):

(Light absorption) $C + h\nu\ (\geq E_g) \longrightarrow C^*\ (h^+ + e^-)$

(Water oxidation) $2H_2O + 4h^+ \longrightarrow O_2 + 4H^+$

(Hydrogen reduction) $4H^+ + 4e^- \longrightarrow 2H_2$

(Overall reaction) $2H_2O \longleftrightarrow 2H_2 + O_2$

1.2 Semiconductor as a photocatalyst

Photocatalysis requires a suitable photocatalyst which must enables wide light absorption, charge separation, migration and transfer to the solution for redox reactions, suitable band edge energy, strong photocatalytic activity, good stability, sustainability and low cost (Li and Wu, 2015). From these requirments, $BiVO_4$ is a good candidate that having been considered.

1.2.1 Physical and chemical properties of $BiVO_4$

$BiVO_4$ is a bright yellow semiconductor which is nontoxic, stable, environmental friendly material and has good chemical and physical properties for applying in color pigment (Wood and Glasser, 2004) and a photocatalyst under visible light (Lai *et al.*, 2014; Li *et al.*, 2013; Sun *et al.*, 2014). Physical and chemical properties of commercial $BiVO_4$ are reported by a LTS Research Laboratories, Inc. and showed in Table 1.

Table 1 Physical and chemical properties of $BiVO_4$ (Chen *et al.*, 2017; Marta Castellote, 2011)

Properties	Information
Mineral name	Clinobisvanite
Molecular formula	$BiVO_4$
CAS No.	14059-33-7
Appearance	Yellow solid
Molecular weight	323.92 g mol^{-1}
Density	6.95 g cm^{-3}
Water solubility	Insoluble
Melting point	>1000 °C

1.2.2 Chemical structure of $BiVO_4$

Chemical structure of $BiVO_4$ which represents its crystalline structure and electronic structure plays important role in its photocatalytic activity. There are three crystalline structures of synthetic $BiVO_4$ (Fan *et al.*, 2012); tetragonal zircon (tz), tetragonal scheelite (ts) and monoclinic scheelite (ms) as shows in Fig. 3. Among these crystal types, the ms-$BiVO_4$ has the highest photocatalytic activity under visible irradiation for hydrogen or oxygen evaluation and organic pollutants degradation. This is due to the narrow band gap energy of the monoclinic structure $BiVO_4$ ranging from 2.4 to 2.5 eV. This small band gap allowed the catalyst to absorb energy in the visible light region (Kudo *et al.*, 1999).

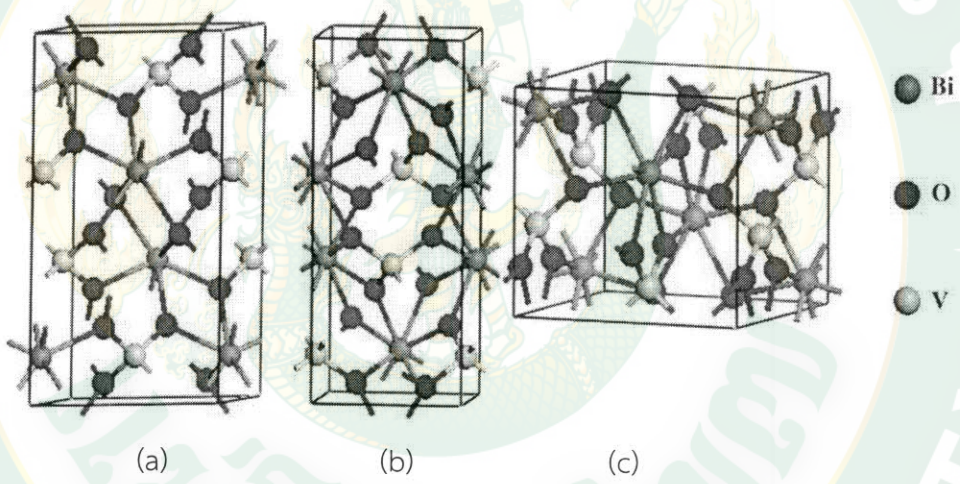

Figure 3 $BiVO_4$ crystalline phases: (a) monoclinic, (b) tetragonal scheelite and (c) tetragonal zircon $BiVO_4$ (Ding *et al.*, 2013).

In addition, electronic structure of the ms-$BiVO_4$ composes of CB formed by V 3d atomic orbitals and VB formed by means of the hybridization of Bi 6s and O 2p atomic orbitals are presented in Fig. 4 (with respect to vacuum) (Cooper *et al.*, 2014; He *et al.*, 2014). Moreover, Fermi energy (ϕ_f) is 2.0 eV different from VB. Band edge positions of CB and VB are 4.79 and 7.27 eV, respectively, below the vacuum level (or 0.34 and 2.74 eV, respectively, with respect to natural hydrogen electrode (NHE) (He *et al.*, 2014)).

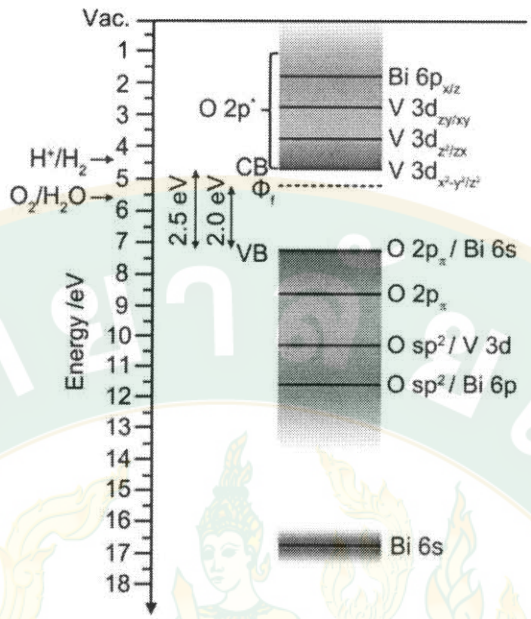

Figure 4 Energy level diagram for the electronic structure of ms-$BiVO_4$ thin film. Equilirium redox potential for H^+/H_2 and O_2/H_2O relative to reversible hydrogen electrode (Cooper *et al.*, 2014).

Moreover, another important property that makes ms-$BiVO_4$ suitable for photocatalysis is band edge position. Diagram of band edge positions of $BiVO_4$ comparing to other semiconductors with the vacuum level and the NHE is showed in Fig. 5.

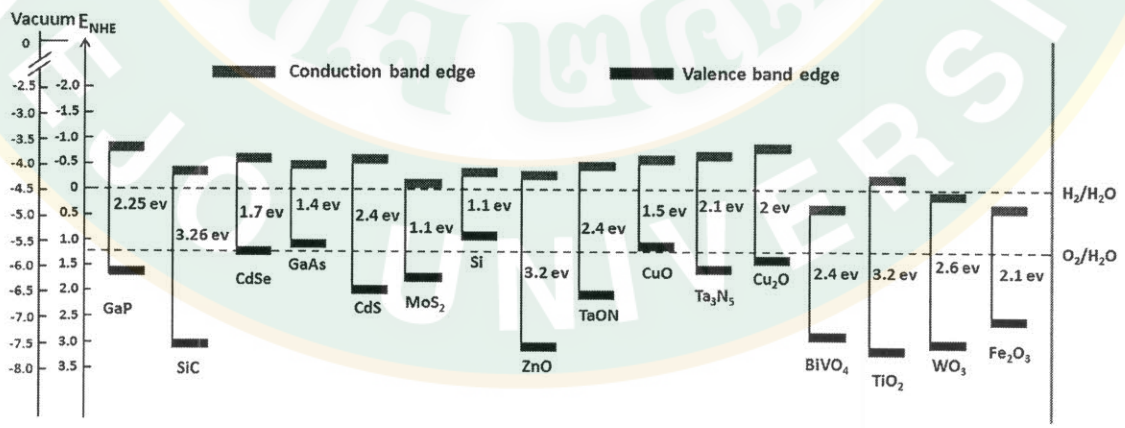

Figure 5 Band edge positions with respect to the vacuum level and the NHE for selected semiconductors at pH = 0 (Tamirat *et al.*, 2016)

1.2.3 Physical and chemical properties of Bi_2WO_6

Bi_2WO_6 is a pale yellow semiconductor. It has been interested because of its excellent photocatalytic activity under visible light with its band gap energy of 2.7 eV (Fu *et al.*, 2005; Fumiaki *et al.*, 2007). Physical and chemical properties of the Bi_2WO_6 are shown in Table 2.

Table 2 Physical and chemical properties of Bi_2WO_6 (Barthelmy, 2014; Dumrongrojthanath, 2015)

Properties	Information
Mineral name	Russellite
Molecular formula	Bi_2WO_6
CAS No.	13595-86-3
Appearance	Pale yellow solid
Molecular weight	697.81 g mol^{-1}
Density	7.35 g cm^{-3}
Water solubility	Insoluble
Melting point	>300 °C

1.2.4 Chemical structure of Bi_2WO_6 (Fu *et al.*, 2006)

Orthorhombic structure of a Bi_2WO_6 crystal includes Bi atoms layers sandwiched between WO_6 octahedral layers. Lattices parameters of the Bi_2WO_6 crystal were a = 0.5437 nm, b = 1.643 nm and c = 0.5458 nm.

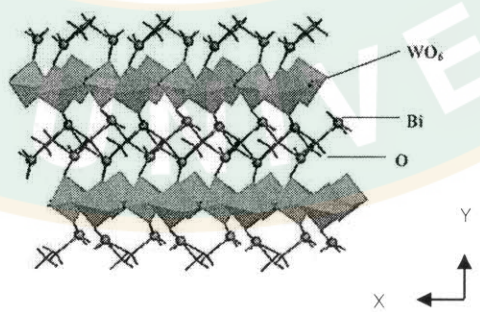

Figure 6 Crystal structure of Bi_2WO_6.

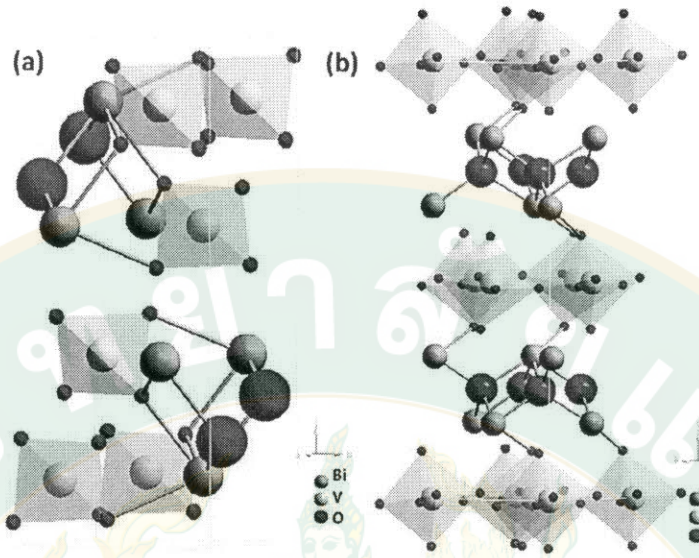

Figure 7 Schematic crystal structure of (a) monoclinic $BiVO_4$ and (b) orthorhombic Bi_2WO_6 in the polyhedron mode (Sun and Wang, 2014).

1.3 Synthesis methods

ms-$BiVO_4$ structure is successful synthesis via various methods including solid-state reaction (Venkatesan *et al.*, 2012), co-precipitation (Martínez-de la Cruz and Perez, 2010; Ravidhas *et al.*, 2015), sonochemical (Zhou *et al.*, 2006) and hydrothermal or solvothermal treatment (Guo *et al.*, 2010; Ma *et al.*, 2013). In comparison, the hydrothermal and solvothermal methods are a soft-chemical process. More than that, effective morphology can be manipulated by controlling some synthesis condition parameters such as pH value, reaction temperature, reaction time and mixture medium. Photocatalytic efficiency of $BiVO_4$ synthesized by solvothermal method using binary green solvent of water and ethanol comparing with pure water was studied and published in 2009 (Lu *et al.*, 2009). The results showed that the crystalline phase of both conditions were pure monoclinic phase. However, the binary solvent exhibited extremely higher photocatalytic degradation of rhodamine B (RhB) under visible-light irradiation. This is due to ethanol played an important role in $BiVO_4$ crystal formation process.

To improve photocatalytic activity of $BiVO_4$, a lot of researchers have tried to describe parameters related to photocatalytic efficiency under visible light.

Many publications showed that the photocatalytic activity of the $BiVO_4$ depends on synthesized method, pH value (which contributes to differential morphology of $BiVO_4$ particle and surface area), heating temperature and reaction time. Some researchers believed that monoclinic scheelite $BiVO_4$ with narrow band gap energy (E_g) enhances the photocatalytic performance. However, the narrow band gap increases recombination probability of induced electron-hole.

Preparing heterojunction of $BiVO_4/Bi_2WO_6$ composite becomes a promising way to retain electron-hole separation life-time by migration of the electron and hole to different materials. Thus, photocatalytic activity of $BiVO_4$ as well as Bi_2WO_6 will be enhanced.

Therefore, in this research, monoclinic $BiVO_4$, flake-ball like Bi_2WO_6 and $BiVO_4/Bi_2WO_6$ composites in various $BiVO_4$ fractions were synthesized by ethanol-assisted hydrothermal method. They were studied deeply in their characteristics and photocatalytic activity relationship.

2. Objectives

2.1 To synthesize monoclinic scheelite $BiVO_4$ powders by ethanol-assisted hydrothermal method.

2.2 To synthesize a flake-ball liked Bi_2WO_6 powder by hydrothermal method.

2.3 To characterize monoclinic scheelite $BiVO_4$ powders that synthesized by ethanol-assisted hydrothermal method.

2.4 To investigate photocatalytic activity of $BiVO_4$ powder under visible light.

2.5 To study parameters affect photocatalytic activity of $BiVO_4$ powder.

2.6 To enhance photocatalytic activity of $BiVO_4$ powder under visible light by adding Bi_2WO_6 powder to form a composite.

2.7 To study $Bi_2WO_6/BiVO_4$ composites structure for photocatalytic enhancement for further applications using $BiVO_4$ based composite.

3. Expected benefits

3.1 Monoclinic scheelite $BiVO_4$ powder can be synthesized by ethanol-assisted hydrothermal method.

3.2 Stable structure of flake-ball like Bi_2WO_6 powder can be obtained by hydrothermal method.

3.3 Characteristics of monoclinic scheelite $BiVO_4$ powder can describe their relationship with synthesized conditions.

3.4 Synthesized $BiVO_4$ powder can drive photocatalysis under visible light.

3.5 Parameters affected photocatalytic activity of $BiVO_4$ powder can be investigated and evaluated for their relationship.

3.6 $BiVO_4/Bi_2WO_6$ composite enhances photocatalytic activity under visible light.

3.7 An idea of powerful $BiVO_4/Bi_2WO_6$ composite design is proposed for high-level photocatalytic enhancement for energy and environmental applications.

CHAPTER 2

LITERATURE REVIEWS

1. Synthesis of monoclinic $BiVO_4$ powder by ethanol assisted-hydrothermal method

Various synthesize methods of monoclinic scheelite $BiVO_4$ powder have been reported as mentioned in Chapter 1. However, ethanol assisted-hydrothermal method is an interesting strategy.

Lu *et al.* (2009) studied relationship between $BiVO_4$ structure synthesized by ethanol assisted-hydrothermal method and photocatalytic activity for rhodamine B degradation under visible light. 1 mmol Bismuth nitrate ($Bi(NO_3)_3{\cdot}5H_2O$) and 1 mmol ammonium meta vanadate (NH_4VO_3) solutions were used as starting materials. After mixing, pH of the mixture was adjusted to 4 and transferred into 100 mL Teflon-lines stainless-steel autoclave for heat treatment at 140 or 160 °C for 12 h. The X-ray diffraction (XRD) patterns in Fig. 8 showed that monoclinic $BiVO_4$ was obtained by using both pure-water and binary solvent (ethanol:water = 3:1) as a solvent in synthesis reaction comparing to JCPDS card No. 14-0688. However, $BiVO_4$ which synthesized by binary solvent had higher surface area and photocatalytic activity than pure water. The binary solvent played important role in crystal formation leading to different in morphology which affected photocatalytic activity of the $BiVO_4$. Moreover, morphology of $BiVO_4$ was depended on synthesize conditions such as concentration of precursors and reaction temperature. $BiVO_4$ with two-dimensional (2D) morphologies (platelike and disclike structures) had better photocatalytic activity than three-dimensional (3D) morphologies (flowerlike superstructures and hexagonal-prismatic nanotubes).

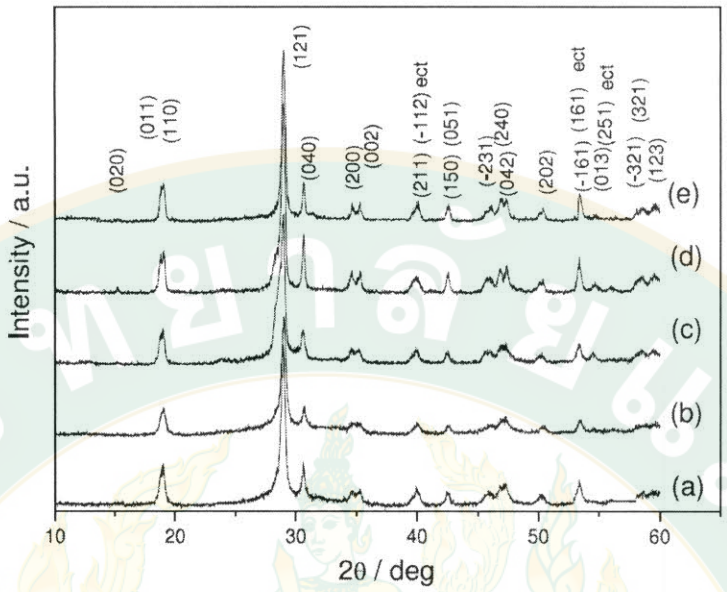

Figure 8 XRD patterns of $BiVO_4$ (a)-(d) ethanol+water and (e) pure water (Lu *et al.*, 2009).

Sun *et al.* (2009) studied methylene blue (MB) removal by photocatalysis of $BiVO_4$ synthesized by hydrothermal method using ethanol-ethylenediamine tetraacetic acid (EtOH-EDTA) as a mixed solvent. In synthesis process, 2.5 mmol Bismuth nitrate ($Bi(NO_3)_3{\cdot}5H_2O$) and 2.5 mmol ammonium meta vanadate (NH_4VO_3) were used as starting materials. After co-precipitation, it was heated in a 50 mL Teflon-lines stainless-steel autoclave at 120 °C for 12 h. Characterize results showed various morphologies of $BiVO_4$ by adding EDTA with different molar ratio of EDTA to Bi. These due to adding chelate EDTA had an influence in crystal formation. Photocatalytic efficiency of obtained $BiVO_4$ was evaluated by investigation of degradation of MB comparing with $BiVO_4$ synthesized by solid state reaction. It was found that 91% degradation of MB under visible light was achieved after 25 min irradiation by using starlike $BiVO_4$ prepared by EtOH-EDTA-assisted hydrothermal (EDTA/Bi = 0.75). This was much higher than hydrothermal without EDTA and the solid state reaction even though its surface area was smallest. These suggested that nanoplate structure with large atom density of (010) plan on surface led photogenerated electrons and hole to diffuse easily on the surface and reacted efficiently to MB.

Jiang *et al.* (2011) studied morphology-dependent photocatalytic activity of $BiVO_4$ monoclinic scheelite structure by investigation of methyl orange (MO) degradation under visible light. Monoclinic $BiVO_4$ was synthesized by ethanol-assisted hydrothermal method which triblock copolymer (P123: poly(ethylene glycol)-poly(propylene glycol)-poly(ethylene glycol)) was added as a surfactant. 10 mmol bismuth nitrate ($Bi(NO_3)_3{\cdot}5H_2O$) and 10 mmol ammonium meta vanadate (NH_4VO_3) were used as starting materials. Mixture's pH value was adjusted to 2, 7 and 10 and reaction temperature was controlled at 180 °C for 12 h. The characterization results showed that morphology of $BiVO_4$ was significantly influenced by pH of mixture and surfactant. In addition, Bi^{3+}, V^{4+}, V^{5+} and oxygen species were determined and summarized that high surface V^{4+}/V^{5+} molar ratio contained high amount of surface oxygen vacancies. The highest V^{4+}/V^{5+} molar ratio and the highest photocatalytic activity for degradation of MO was occurred by using $BiVO_4$ synthesized at pH 2 with P123 surfactant (rodlike morphology). It was suggested that fabrication of $BiVO_4$ particle with high surface area, high surface oxygen vacancy, high intensity of (040) planes enhanced photocatalytic activity.

2. Effect of pH adjustment, reaction temperature and time

Dong *et al.* (2014) studied shape-controlled synthesis and photocatalysis under natural light of $BiVO_4$ synthesized by solvothermal method (ethanol : acetic acid : water = 1 : 1 : 3). 2 mmol bismuth nitrate ($Bi(NO_3)_3{\cdot}5H_2O$) and 2 mmol ammonium meta vanadate (NH_4VO_3) were used as starting materials. pH value of mixture was adjusted to 1.7–7.98. Then it was heated at 80 °C for 3 h. X-ray diffraction (XRD) pattern showed that relative intensities of (110) and (040) diffraction peaks increased with increasing pH value of the mixture. Hierarchical structure of $BiVO_4$ including peanut, dumbbell, flower, sphere, olive and rod-sheaves was obtained differently by pH adjustment using ammonium hydroxide ($NH_3{\cdot}H_2O$) or sodium hydroxide (NaOH). Moreover, morphology of $BiVO_4$ at the same pH was differenced due to basic solvent used for pH adjustment. pH value also influenced on electronic structure of $BiVO_4$. Band gap energy (E_g) was declined with decreasing of pH value. Photocatalytic performance of $BiVO_4$ was determined in terms of

degradation of Rhodamine B (RhB) dye. The greatest photocatalytic performance could be obtained by using $BiVO_4$ synthesized at pH 6.26 (dumbbell shape and olive-like shape adjustment by using $NH_3 \cdot H_2O$ (A6.26) and NaOH (S6.26), respectively). These suggested that perfect and unique 3D shape played important role in photodegradation of RhB. However, results showed that photocatalytic efficiency was not related to surface area and aspect ratios of the fabricated photocatalyst.

Ke *et al.* (2009) studied effects of hydrothermal temperature on the microstructures of $BiVO_4$ and its photocatalytic O_2 evolution activity under visible light. 2.9100 g (7 mmol) bismuth nitrate ($Bi(NO_3)_3 \cdot 5H_2O$) and 0.7204 g (6 mmol) ammonium meta vanadate (NH_4VO_3); in 30 mL of a 0.5M nitric acid, were used as starting materials. Next, 30 mL of 0.03 M cetyltrimethylammonium bromide (CTAB) solution was added to the mixture of the starting materials. Then, pH of the mixture was controlled at 6 by adding ammonium solution. After aging for 12 h, it was transferred into Teflon-lines stainless-steel autoclave and reaction temperature was controlled at 80, 120, 160 and 200 °C for 72 h. XRD patterns of $BiVO_4$ synthesized at different temperatures were showed in Fig. 9. It was clearly that mixed phase of tetragonal and monoclinic $BiVO_4$ was obtained at reaction temperature of 80–160 °C but tetragonal phase transform to pure monoclinic phase at 200 °C. However, prolonging the hydrothermal time from 72 to 96 h, a pure monoclinic phase $BiVO_4$ could also be obtained at 160 °C. Photocatalytic activity was showed that lamellar $BiVO_4$ synthesize at 200 °C had better photocatalyst than microsphere $BiVO_4$ with mixed phases synthesized at lower temperature. So that, phase and morphology of the $BiVO_4$ was significant depended on hydrothermal temperature as well as oxygen evolution by photocatalysis under visible light.

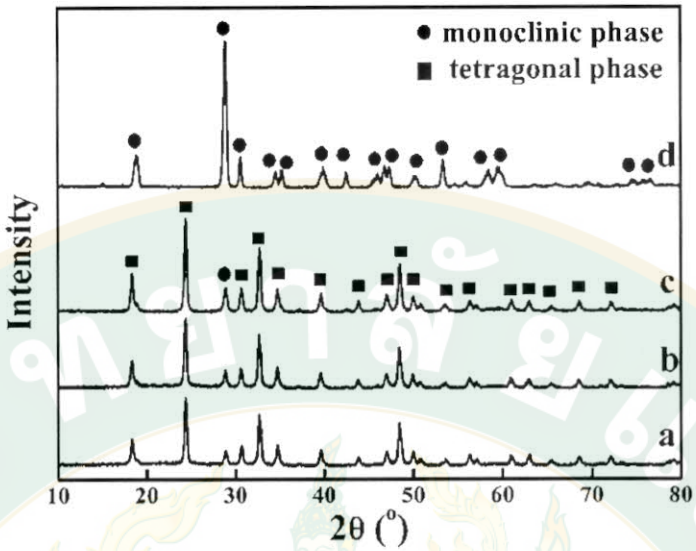

Figure 9 XRD patterns of $BiVO_4$ synthesized at different hydrothermal temperatures for 72 h in the presence of 0.03 M CTAB. (a) 80 °C, (b) 120 °C, (c) 160 °C, and (d) 200 °C (Ke *et al.*, 2009).

Lu *et al.* (2014) reported core-shell structured (CSS) $BiVO_4$ hollow spheres synthesized by ethanol and acetic acid-assisted hydrothermal method. 1 mmol Bimuth nitrate ($Bi(NO_3)_3{\cdot}5H_2O$) and 1 mmol ammonium meta vanadate (NH_4VO_3) were used as starting materials. Mixture' pH value was kept at 2. It was heated at temperature of 180 °C for 1–15 h. XRD results showed that amorphous compound was obtained before hydrothermal treatment but pure crystalline monoclinic phase of $BiVO_4$ was presented after 1h heating. Intensity of diffraction peak was increased by prolonging reaction time from 1 to 15 h. Morphologies of $BiVO_4$ synthesized at various times were observed by scanning electron microscopy (SEM) and showed in Fig. 10. It revealed that after hydrothermal heating, microsphere was formed and shell of $BiVO_4$ was separated after 5 h of heat treatment. Furthermore, the shell became thinner as reaction time was extended to longer time. Band gap energy (E_g) of CSS $BiVO_4$ was 2.43 eV with large surface area was 13.09 $m^2{\cdot}g^{-1}$. Photocatalytic activity of the CSS $BiVO_4$ was evaluated as degradation of RhB dye under visible light. 99% of RhB was degraded after 4.5 h by using 0.5 $g{\cdot}L^{-1}$ of CSS $BiVO_4$ photocatalyst.

The CSS $BiVO_4$ photocatalyst presented excellent photocatalytic activity and stability that less than 5% decrease of activity after five recycling.

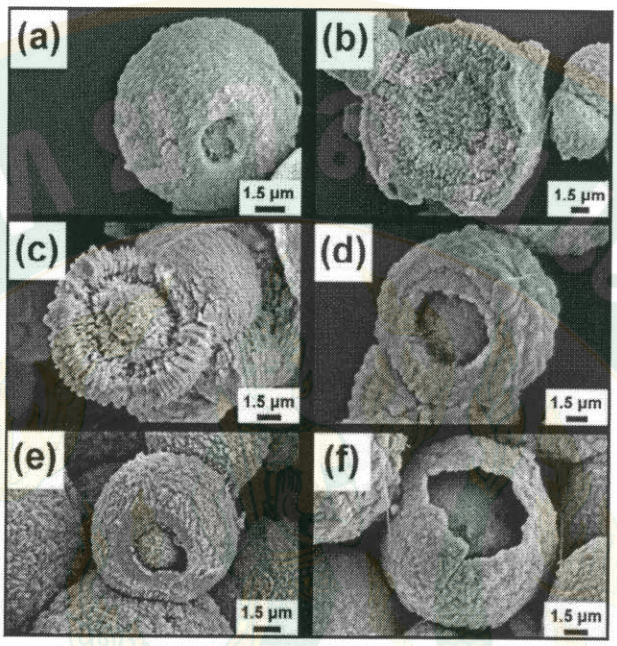

Figure 10 SEM images of CSS $BiVO_4$ hollow spheres: (a) 1, (b) 3, (c) 5, (d) 8, (e) 10 and (f) 15h (Lu *et al.*, 2014).

Thalluri *et al.* (2013) studied parameters affect visible-light-induced photocatalytic activity of monoclinic $BiVO_4$ for water oxidation. The $BiVO_4$ was synthesized by coprecipitation method and then it was calcined at different temperatures. 5 mmol of ammonium metavanadate (NH_4VO_3) solution was added into 5 mmol of bismuth nitrate pentahydrate, ($Bi(NO_3)_3{\cdot}5H_2O$) solution. Precipitate was collected and calcined in air at temperatures of 350, 450, 550, 700, and 800 °C for 3 h. XRD pattern of all $BiVO_4$ samples were exhibited monoclinic scheelite structure. Crystalline size calculated by Scherrer equation was increased after increased calcination temperature from 450 to 800 °C due to aggregation of particles. Surface area was decreased as temperature increased. Raman peaks of V–O bond were shifted to higher frequency related to V–O bond length that was shortened at higher calcination temperature. These demonstrated that shorter V–O bond length, stronger packing and larger lone pair distortion around the Bi cation. Furthermore,

photocatalytic activity of O_2 evolution on $BiVO_4$ was enhanced by calcination temperature increased. It can be summarized that crystalline size, band gap, V–O bond length, and O_2 evolution had a good correlation as shown in Fig. 11.

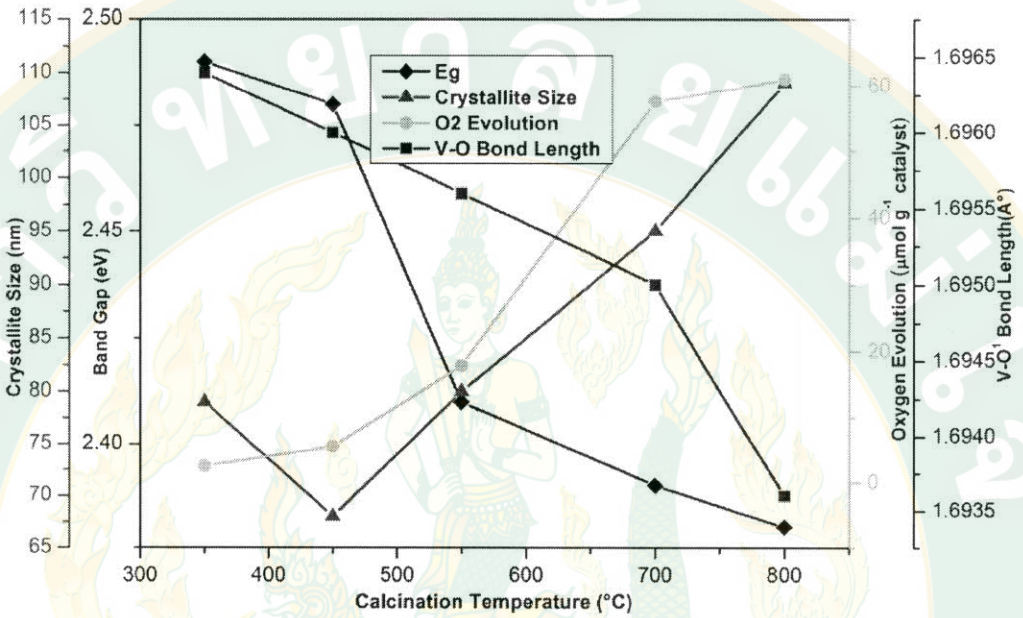

Figure 11 Correlation of characteristic parameters of $BiVO_4$ and O_2 evolution (Thalluri *et al.*, 2013).

3. Synthesis of $BiVO_4/Bi_2WO_6$ composite

Ju *et al.* (2014) studied synthesis and characterization of calcined $Bi_2WO_6/BiVO_4$ (C-$Bi_2WO_6/BiVO_4$) heterojunction photocatalyst as well as its photocatalytic activity (Ju *et al.*, 2014). The C-$Bi_2WO_6/BiVO_4$ was synthesized by hydrothermal method followed by the calcination at 600 °C. In hydrothermal process, $Bi(NO_3)_3{\cdot}5H_2O$ (3 mmol in 30 mL of 2 M HNO_3) and NH_4VO_3 (1 mmol in 30 mL of 1 M NaOH) were used as starting materials for $BiVO_4$ synthesis. $Na_2WO_4{\cdot}2H_2O$ (1 mmol) was added at the same time in NH_4VO_3 solution for $Bi_2WO_6/BiVO_4$ synthesis. Moreover, sodium dodecyl benzene sulfonate (SDBS) was used as surfactant. After coprecipitation, the pH value of the final suspension was adjusted to 7 by 2 M NH_3H_2O and transferred into a 100 mL Teflon-lined autoclave and heat at 160 °C for

12h. Then it was naturally cooled down, filtered, washed and dried. Next, the precipitate was calcined at 600 °C for 4 h to remove all organic compounds. Photocatalytic activities of the $Bi_2WO_6/BiVO_4$ samples were determined as the degradation of RhB under visible light irradiation using a 300W Xe lamp with a 420 nm cutoff filter. XRD patterned confirmed that C-$Bi_2WO_6/BiVO_4$ and $Bi_2WO_6/BiVO_4$ were consisted of Bi_2WO_6 and $BiVO_4$ fractions without an impurity peak was observed. However, it can be seen that the calcined product was better crystallized than non-calcined. Specific surface area of C-Bi_2WO_6, C-$BiVO_4$, $Bi_2WO_6/BiVO_4$, and C-$Bi_2WO_6/BiVO_4$ are 7.67, 3.62, 20.78, and 2.69 $m^2 \cdot g^{-1}$, respectively. This means that calcination decreased surface area. The band gaps of C-Bi_2WO_6, C-$BiVO_4$, $Bi_2WO_6/BiVO_4$, and C-$Bi_2WO_6/BiVO_4$ were estimated to be 2.69, 2.30, 2.18, and 2.08 eV, reapectively. Photocatalytic result in Fig. 12 showed that C-$Bi_2WO_6/BiVO_4$ exhibited higher photocatalytic activity than C-Bi_2WO_6, C-$BiVO_4$, and uncalcined $Bi_2WO_6/BiVO_4$.

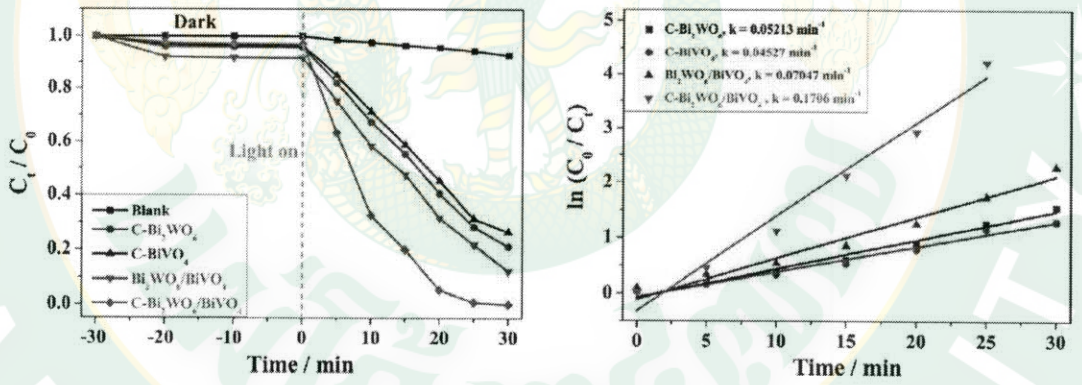

Figure 12 (a) Photocatalytic degradation efficiency of RhB by different photocatalysts under visible light irradiation and (b) the dynamics of RhB degradation reaction (Ju *et al.*, 2014).

In addition, trapping experiments were performed to explain the photocatalytic mechanism of C-$Bi_2WO_6/BiVO_4$ composite. Quenchers were added to the photocatalytic reaction (1.0 mM IPA (a quencher of ·OH), BQ (a quencher of $\cdot O_2$), and TEOA (a quencher of h^+), respectively) to investigate hydroxyl radicals (·OH), superoxide radical ($\cdot O_2$) and holes (h^+). Possible mechanism of C-$Bi_2WO_6/BiVO_4$

photocatalysis was showed in Fig. 13. C-Bi_2WO_6/$BiVO_4$ composite exhibits enhanced photocatalytic activities due to Bi_2WO_6 accelerating the separation of photoinduced electron–hole pairs which reduce the recombination of the photoinduced charge carriers.

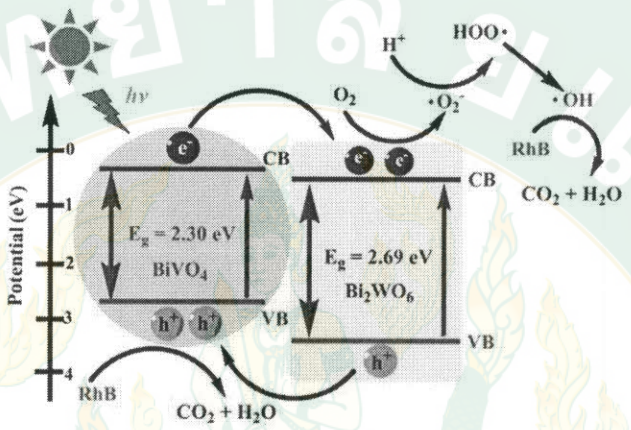

Figure 13 Photocatalytic mechanism of Bi_2WO_6/$BiVO_4$ photocatalyst (Ju *et al.*, 2014).

Ju *et al.* (2016) studied a synthesis of a novel nest-like Bi_2WO_6/$BiVO_4$ photocatalyst and its enhancement in photocatalytic antifouling activity under visible light. The Bi_2WO_6/$BiVO_4$ in difference W/V mole ratios of 1:0.25, 1:0.5, 1:0.75 and 1:1 were synthesized by hydrothermal method. Investigation of morphologies by field-emission scanning electron microscope showed that construction of nanoplates on a flower-like structure was increased as $BiVO_4$ contents increased. Moreover, the more $BiVO_4$ contents increased, more perfect structure of Bi_2WO_6/$BiVO_4$ could be observed as showed in Fig. 14. Photocatalytic antifouling activities showed in Fig. 15 that Bi_2WO_6/$BiVO_4$-1 exhibited the best activity. It was clearly seen that photocatalysis by the Bi_2WO_6/$BiVO_4$-1 proceeded to killing almost of bacteria cells in 60 min with the highest rate over pristine Bi_2WO_6, $BiVO_4$ and other Bi_2WO_6/$BiVO_4$. In addition, photocatalytic antifouling mechanism of the Bi_2WO_6/$BiVO_4$-1 was suggested and showed in Fig. 16.

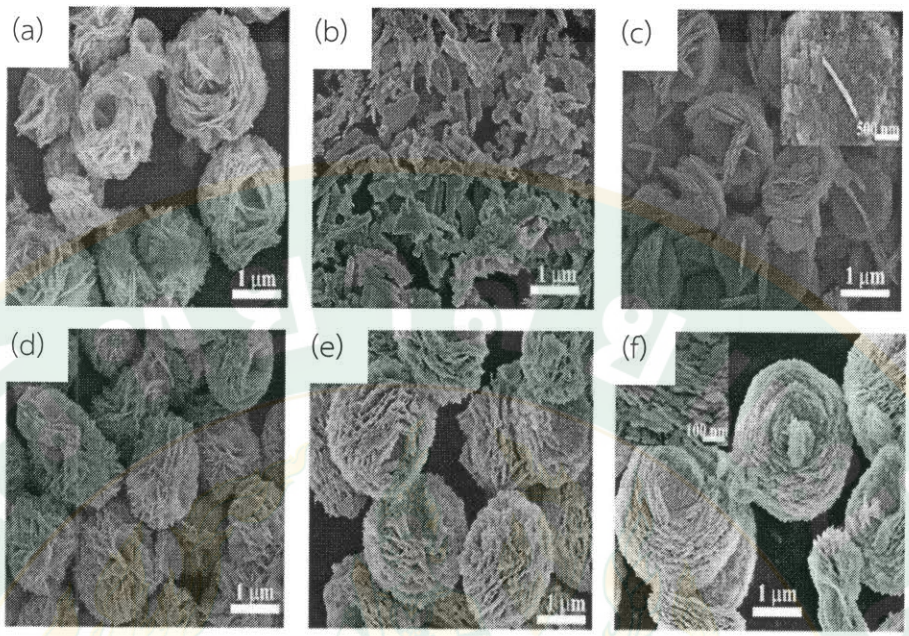

Figure 14 FESEM images of the as-prepared photocatalysts: (a) Bi_2WO_6, (b) $BiVO_4$, (c) $Bi_2WO_6/BiVO_4$-0.25, (d) $Bi_2WO_6/BiVO_4$-0.5, (e) $Bi_2WO_6/BiVO_4$-0.75, and (f) $Bi_2WO_6/BiVO_4$-1.

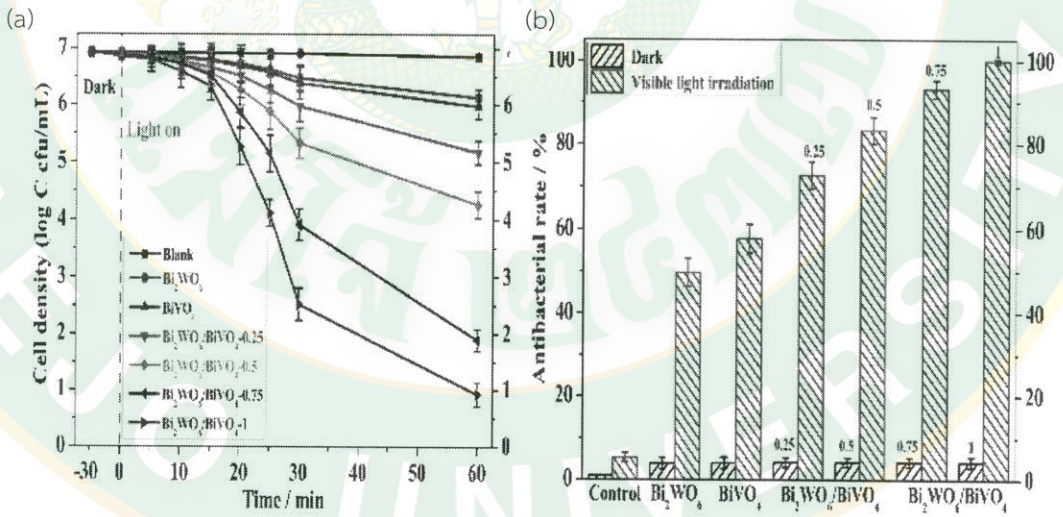

Figure 15 (a) Temporal course of P. aeruginosa (8.5 × 106 cfu mL^{-1}) survival curves in aqueous dispersions containing 1 $mg{\cdot}mL^{-1}$ photocatalyst under visible light and (b) photocatalytic antibacterial rate of different photocatalysts in the dark and irradiated by visible light.

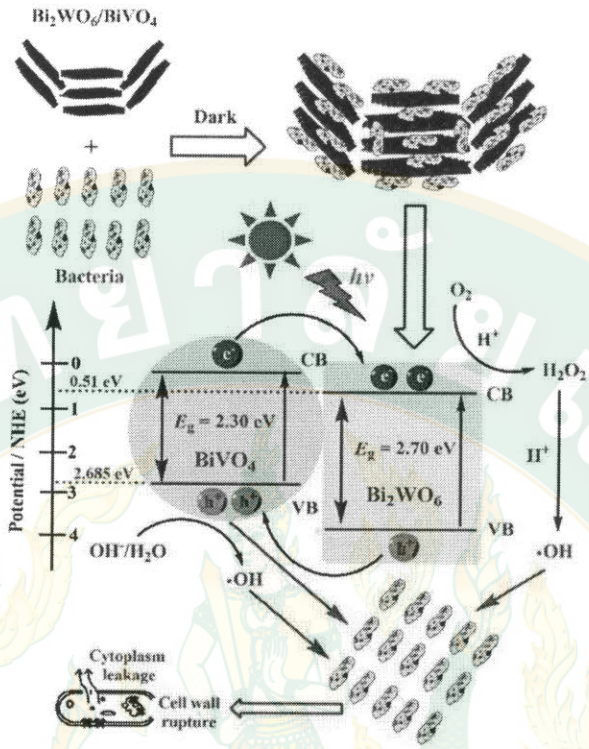

Figure 16 Photocatalytic antifouling mechanism of the $Bi_2WO_6/BiVO_4$-1 composite.

4. Visible driven photodegradation of methyl orange

Zhang *et al.* (2009) studied effects of pH on hydrothermal synthesis and photocatalytic activities of the $BiVO_4$ evaluated by the decolorization of methyl orange (MO) in aqueous solution under visible light irradiation. 0.02 mol $Bi(NO_3)_3{\cdot}5H_2O$ and 0.02 mol NH_4VO_3 were used as starting materials. These two solutions were mixed and the pH values were adjusted to be 1.7, 3.2, 5.3, 6.9, 8.8 and 11.5 by diluted NaOH and HNO_3 solutions. Characterization results showed that crystalline phase, morphology, surface area and electronic structures of obtained $BiVO_4$ were significantly influenced by pH used in hydrothermal synthesis. Mixed phases of tetragonal and monoclicnic structrues could be occurred at low pH and pure monoclinic phase could be selectively synthesis by increasing pH value. Photocatalytic activity of $BiVO_4$ samples were studied by decolorization of MO under visible light irradiation using a 500-W Xe-lamp with UV cut-off. 0.2 g of $BiVO_4$ photocatalyst was added into 100 mL of 10 ppm MO solution. The solution was

stirred for 10 min in darkness in order to reach the adsorption–desorption equilibrium. At a certain irradiation time, each 5 mL suspension was taken, and solution was collected by centrifugation to determined concentrations of the MO by checking the absorbance of solutions at 464 nm. Percentage of degradation in Fig. 17 showed that $BiVO_4$ synthesized at pH 6.9 (d) was sharply increased in first 5 min and the highest of 98.5% MO degradation could be obtained in 60 min. This rapid high photocatalytic activity of the $BiVO_4$ synthesized at pH 6.9 was because of strong absorption of visible light due to the narrow band gap (2.29 eV) and large surface area (4.98 $m^2 \cdot g^{-1}$).

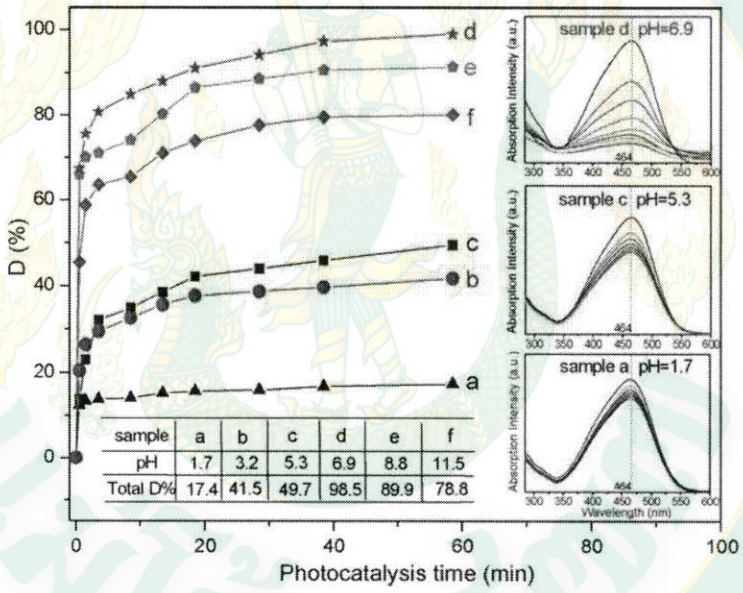

Figure 17 Photodegradation of MO by $BiVO_4$ samples prepared at different pHs: (a) 1.7; (b) 3.2; (c) 5.3; (d) 6.9; (e) 8.8; (f) 11.5 (Zhang *et al.*, 2009).

Jiang *et al.* (2012) studied synthesis of multiple morphologies of $BiVO_4$ powders via hydrothermal method and their visible-light-driven photocatalytic properties for methyl orange (MO) degradation. 10 mmol of well-ground $Bi(NO_3)_3 \cdot 5H_2O$ and 10 mmol NH_4VO_3 were used as starting materials. The starting materials were dissolved in 50 mL of 2 M HNO_3. Hydrothermal treatment was controlled at 100 or 160 °C for 30 h. Yellow precipitate was obtained and calcined at

550 °C for 4 h. Characterization results showed that spherical $BiVO_4$ with porous structures was fabricated by hydrothermal treatment at 100 °C with poly(vinyl pyrrolidone) (PVP) and urea pH = 2. On the other hand, flower-cluster-like $BiVO_4$, and flower-bundle-like $BiVO_4$ were generated hydrothermally at 100°C without PVP at 160°C with $NaHCO_3$ adjustment of pH = 7 and 8, respectively. XRD patterns and Raman spectra of all conditions confirmed that $BiVO_4$ samples were monoclinic structure. Photocatalytic activities of the $BiVO_4$ samples were studied by evaluation of the MO degradation under visible-light generated by a 300-W Xe lamp with an UV optical cut-off filter. 0.1 g of the $BiVO_4$ or P25 (TiO_2) sample was added to 200 mL of 10 ppm MO solution. Then mixture was sonicated for 30 min and stirred in dark for 3h to reach absorption equilibrium. 4 mL of reactant was taken every 20 min and solution was separated by centrifugation. The concentration of MO solution was analyzed by UV-Vis equipment. Photocatalytic performance of $BiVO_4$ samples showed in Fig. 18 and the spherical $BiVO_4$ presented the best activity with a surface area of 8.4 $m^2 \cdot g^{-1}$ was associated with its higher surface area, narrower band gap energy, higher surface oxygen vacancy density, and unique porous architecture.

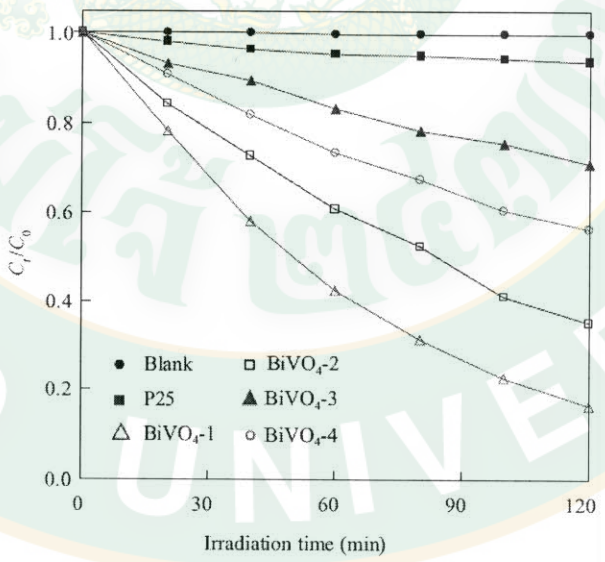

Figure 18 Photocatalytic performance of $BiVO_4$ samples: $BiVO_4$-1 spherical, $BiVO_4$-2 porous spherical, $BiVO_4$-3 flower-cluster-like and $BiVO_4$-4 flower-bundle-like (Jiang *et al.*, 2012).

5. Visible driven photocatalysis oxygen liberation

Soma *et al.* (2014) reported photocatalytic oxygen (O_2) liberation (evolution) performance of high crystallinity $BiVO_4$ under visible light. The $BiVO_4$ was synthesized with a short synthetic time by a homogeneous-precipitation urea method using microwave as the internal heating (MW-urea method). Photocatalytic O_2 liberation from an aqueous silver nitrate solution over various synthesized method $BiVO_4$ showed in Table 3 that photocatalytic activity increased by heating time due to the increasing of ms- phase. Moreover, small amount of defect and clear crystal facets of the single crystal like particle also contributed to high photocatalytic activity Fig. 19.

Table 3 Sacrificial O_2 liberation over $BiVO_4$ photocatalyst prepared by various methods (Soma *et al.*, 2014)

Preparation method	Preparation condition	Crystal form	Surface area ($m^2 \cdot g^{-1}$)	Rate of O_2 evolution ($\mu mol\ h^{-1}$)
MW-urea	373 K, 5 min	z-t[a], s-m[b]	1.1	31
MW-urea	373 K, 30 min	z-t[a], s-m[b]	0.2	318
MW-urea	373 K, 45 min	s-m[b]	0.3	466
MW-urea	373 K, 60 min	s-m[b]	0.4	597
MW-urea	373 K, 120 min	s-m[b]	0.3	481
Urea	348 K, 60 min	z-t[a], s-m[b]	0.7	285
Urea	348 K, 300 min	s-m[b]	0.4	373
MW-LSR	373 K, 240 min	s-m[b]	1.5	625
LSR	R.T., 3 days	s-m[b]	1.8	142

*Photocatalyst: 0.5 g; reactant solution: 0.05 mol L^{-1} $AgNO_3$ aq., 120 mL; light source: 300 W Xe lamp with a cut-off filter (λ > 420 nm)

a z–t: zircon structure tetragonal system

b s–m: scheelite structure monoclinic system

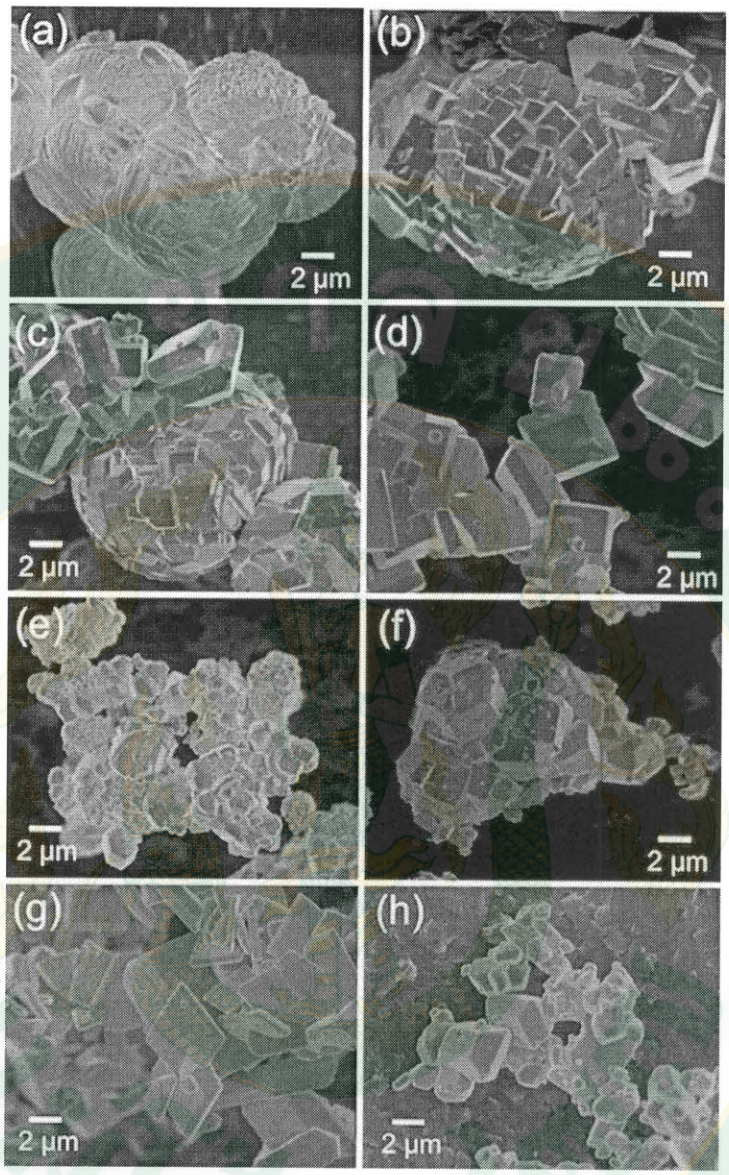

Figure 19 SEM images of $BiVO_4$ prepared by (a)-(d) MW-urea method, (e), (f) Urea method (g) MW-LSR, and (h) LSR. Each preparation time is (a) 5 min, (b) 30 min, (c) 45 min, (d) 60 min, (e) 60 min, (f) 300 min, (g) 240 min and (h) 3 days.

In addition, $BiVO_4$ prepared by microwave-urea method was reported its performance in Z-schematic solar water splitting with Fe^{3+}/Fe^{2+} electron mediator. In the system, 0.2 g of $Ru/SrTiO_3$:Rh and 0.4 g of $BiVO_4$ photocatalysts were used for H_2-evoling and O_2-evolving, respectively. Reactant solution was prepared: 2 mmol L^{-1}

$FeCl_3$ aq. 120 mL (pH 2.4), light source: solar simulator (AM-1.5, 100 mW cm^{-2}), irradiated area: 33 cm^2. It was resulted in Fig. 20 that solar water splitting steadily proceeded and gave activities of 354 and 171 mL h^{-1} for H_2 and O_2 evolution, respectively, for 1 m^2 irradiation area.

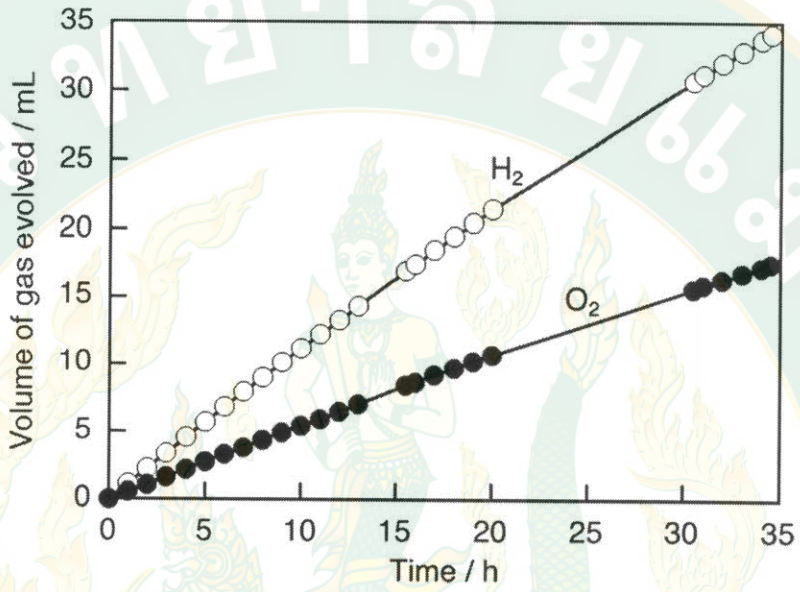

Figure 20 Z-schematic solar water splitting using $Ru/SrTiO_3$:Rh and $BiVO_4$ photocatalysts for H_2 and O_2 evolution, respectively. (Soma *et al.*, 2014).

CHAPTER 3

RESEARCH METHODOLOGY

Research methodology is separated into four main parts. The first part is synthesis of $BiVO_4$ powder by ethanol-assisted hydrothermal (ET) method. The second part is synthesis of $BiVO_4/Bi_2WO_6$ composites by ET method. The third part is characterization of products obtained from the first and second parts. The last part is a study of photocatalytic activity of the $BiVO_4$ powders and $BiVO_4/Bi_2WO_6$ composites.

1. Synthesis of $BiVO_4$

1.1 Chemicals

Analytical grade chemical used through these experiments are shown in Table 4.

Table 4 Chemicals used for $BiVO_4$ synthesis and methyl orange photodegradation

Chemical lists	assay	Manufacturer	Country
1. Ammonium hydroxide (NH_4OH)	29.5 % v/v	J.T. Baker	USA
2. Ammonium vanadate (NH_4VO_3)	99.5 % w/w	Ajax	New Zealand
3. Bismuth nitrate pentahydrate ($Bi(NO_3)_3{\cdot}5H_2O$)	98.0 % w/w	Fluka	England
4. Ethanol (C_2H_5OH)	99.8 % v/v	Liquor Distillery Organization Excise Department	Thailand
5. Methyl orange ($C_{14}H_{14}N_3NaO_3S$)	AR grade	RCI Labscan	Thailand
6. Nitric acid (HNO_3)	65.0 % v/v	RCI Labscan	Thailand

1.2 Instruments

Table 5 Instruments used for $BiVO_4$ synthesis and methyl orange photodegradation

Instrument	Manufacturer	Country
1. Analytical balance	Mettler Toledo	Switzerland
2. Centrifuge machine	Labquip Centurion 1000 series	England
3. Energy dispersive X-ray spectrometer	Oxford IncaPentaFETx3	England
4. Fine coater	JEOL JFC 1200	Japan
5. Fourier transform infrared spectrophotometer	AB304-5 PerkinElmer SpectrumRX I	USA
6. LED Lamp 14 Watt (cool daylight)	Philips Electronic	China
7. Mortar	-	-
8. Oven	Memmert	Germany
9. Scanning electron microscope	JEOL JSM-6335F	Japan
10. Surface area analyzer	Quantachrome Autosorb 1 MP	USA
10. Ultrasonic bath	Labquid 136H	England
11. UV-Vis spectrometer	Hitachi U2900	Japan
12. UV-Vis diffuse reflectance spectrometer	Shimadzu UV2600	Japan
13. X-ray diffractometer	Bruker D8 Advance	Germany
14. X-ray absorption spectroscope	SUT-NANOTEC-SLRI XAS beamline (BL. 5.2)	Thailand

1.3 Experimental

1.3.1 $BiVO_4$ was synthesized by Bi and V ratio of 1:1. Solution A was prepared by dissolving 10 mmol $Bi(NO_3)_3 \cdot 5H_2O$ in 20 mL of 6 M HNO_3. Solution B was prepared by dissolving 10 mmol NH_4VO_3 in 40 mL of 5 M NH_4OH.

1.3.2 After that, solution B was slowly and carefully dropped into solution A while continuously stirring.

1.3.3 The pH of the mixture was adjusted to 6–8. The mixture became yellow slurry.

1.3.4 Then, 100 mL of absolute C_2H_5OH was poured into the mixture. It was stirred for 60 minutes before adding some absolute C_2H_5OH to make the final volume 200 mL and transferred to a 1,000 mL Teflon-lined stainless steel reactor.

1.3.5 The ET conditions were controlled by heating at temperature of 100–200 °C for 2–6 h as showed in Table 6 and 7.

1.3.6 Finally, yellow precipitate was obtained and then it was separated by a centrifuge at 3000 rpm for 10 min, washed with deionized water three times and dried in an oven at 100 °C for 24 h.

1.3.7 The obtained powder was ground before characterization and photocatalysis study.

Table 6 Ethanol-assisted hydrothermal conditions at 200 °C for 4 h

pH	Temperature (°C)	Time (h)
6	200	4
7	200	4
8	200	4

Table 7 Ethanol-assisted hydrothermal conditions at pH 7

pH	Temperature (°C)	Time (h)
7	100	2
7	100	4
7	100	6
7	200	2
7	200	4
7	200	6

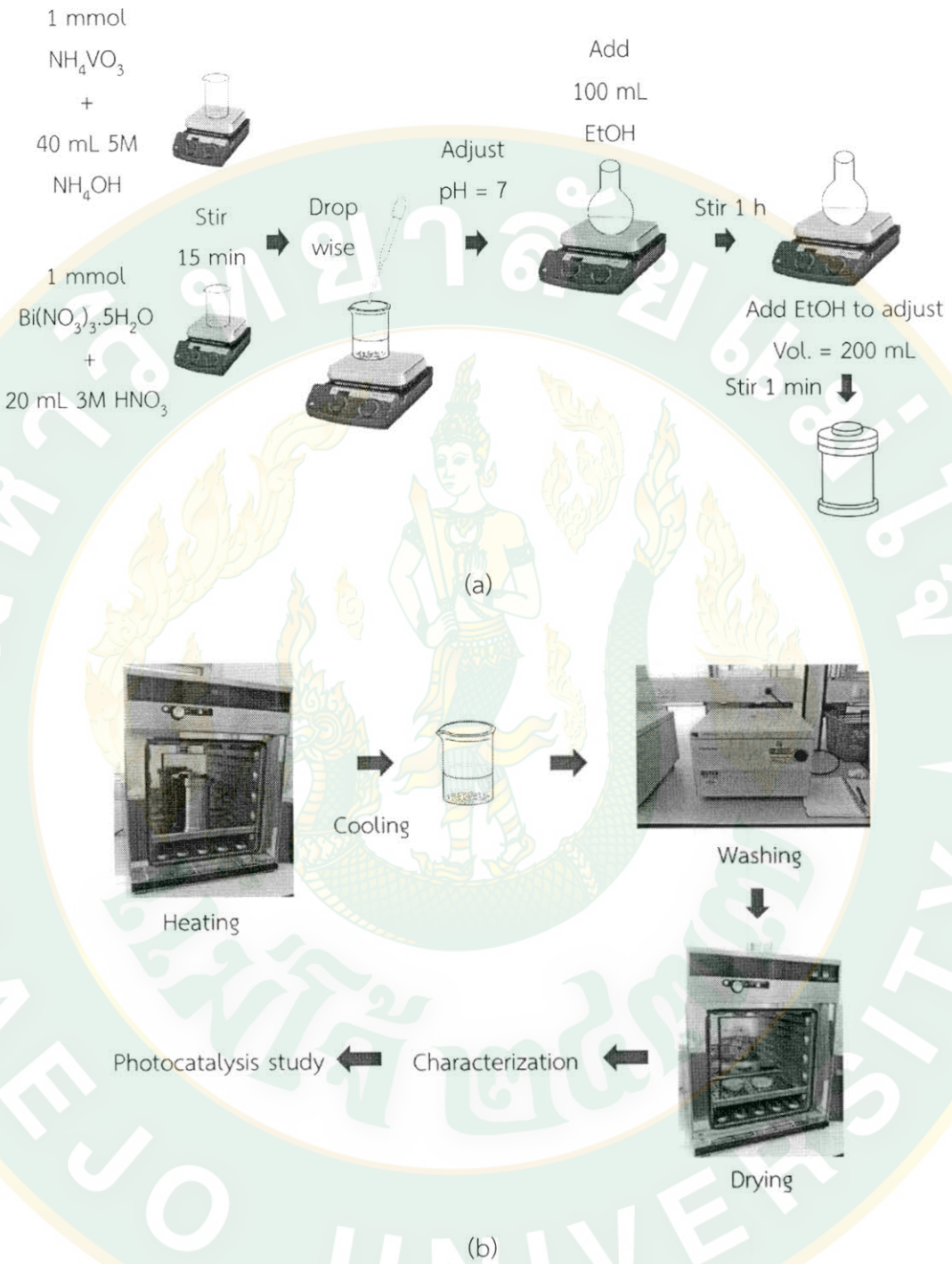

Figure 21 Scheme of synthesis of $BiVO_4$ via ethanol-assisted hydrothermal method: (a) co-precipitation and (b) hydrothermal reaction.

2. Synthesis of $BiVO_4/Bi_2WO_6$ composites

2.1 Chemicals

$BiVO_4/Bi_2WO_6$ composites were synthesized in OHTANI's laboratory at Hokkaido University, Japan. So that, all chemicals use in this part are totally different manufacturer. However, all chemical used are analytical grade as shows in Table 8.

Table 8 Chemicals used for $BiVO_4/Bi_2WO_6$ synthesis and photocatalytic oxygen liberation

Chemical lists	assay	Manufacturer	Country
1. Ammonium solution (NH_3)	25.0 % w/w	Wako Pure Chemical	Japan
2. Ammonium vanadate (NH_4VO_3)	99.0 % w/w		
3. Bismuth nitrate pentahydrate ($Bi(NO_3)_3 \cdot 5H_2O$)	99.9 % w/w		
4. Ethanol (C_2H_5OH)	99.5 % w/w		
5. Iron(III) chloride hexahydrate ($FeCl_3 \cdot 6H_2O$)	99.9 % w/w		
6. Nitric acid (HNO_3)	60 % v/v		
7. Sodium tungstate (VI) dihydrate ($Na_2WO_4 \cdot 6H_2O$)	99.0 % v/v		

2.2 Instruments

Table 9 Instruments used for $BiVO_4/Bi_2WO_6$ synthesis and photocatalytic oxygen liberation

Instrument	Manufacturer	Country
1. Analytical balance	SHIMADZI	Japan
2. Centrifuge machine	KUBOTA 2010	Japan
3. Centrifuge machine (micro centrifuge)	Eppendorf 5424	Germany
4. Electric furnace	SHIROTA DENKI ROZAI Super series	Japan

Table 9 (Continued)

Instrument	Manufacturer	Country
5. Energy dispersive X-ray spectrometer (EDS)	Oxford IncaPentaFETx3	Japan
6. Gas chromatograph (GC-8A)	Shimadzu	Japan
7. Magnetic stirrer	ASONE HS-30D	Japan
8. Oven (drying oven)	ADVANTEC VR420	Japan
9. Oven (hydrothermal oven)	Yamato DKN 302	Japan
10. Photoacoustic spectroscopy (PAS)	Household	Japan
11. Scanning electron microscope (SEM)	JEOL JSM-7400F	Japan
12. Surface area analyzer	Quantachrome NOVA1200e	Japan
13. Ultrasonic bath	YAMATO BRANSON 5800	Japan
14. UV-Vis diffuse reflectance spectrometer (UV-Vis DRS)	Jasco V-670	Japan
15. X-ray absorption spectrometer (XAS)	SUT-NANOTEC-SLRI XAS beamline (BL. 5.2)	Thailand
16. X-ray diffractometer (XRD)	Rigaku Smart lab	Japan
17. X-ray photoelectron spectrometer (XPS)	XPS beamline (BL. 5.3)	Thailand

2.3 Experimental

$BiVO_4/Bi_2WO_6$ was synthesized via ethanol-assisted hydrothermal method using the same synthesis process as $BiVO_4$ (10 times smaller in batch size) and Bi_2WO_6 powder was added into suspension before heating.

2.3.1 Synthesis of Bi_2WO_6 powder

Firstly, flake-ball like (FB) Bi_2WO_6 powder was synthesized by hydrothermal method at 200 °C for 20 h according to the previous report (Hori *et al.*, 2017). In the synthesis process, $Bi(NO_3)_3{\cdot}5H_2O$ and $Na_2WO_4{\cdot}2H_2O$ were used as starting materials as shown in Fig. 22. In solution A, 5.0 mmol (2.4202 g) of the $Bi(NO_3)_3{\cdot}5H_2O$ was easily dissolved in 10 mL pure water under magnetic stirring at 500 rpm. Separately, solution B was 2.75 mmol (0.9072 g) of $Na_2WO_4{\cdot}2H_2O$ which was completely dissolved in 40 mL pure water. Then, the solution B was slowly added drop wise into the solution A under continuous stirring. After that, 10 min stirring followed by 10 min sonication were applied to the suspension. Consequently, water was added to adjust the final volume to 70 mL before hydrothermal heating at 200 °C for 20 h. After natural cooling, pale yellow precipitate was obtained. It was wash with 50 mL water 3 times until pH of liquid phase was 7 and dried at 120 °C for 4 h. Finally, dried Bi_2WO_6 cake was ground and its powder was collected and keeps in a dry glass bottom.

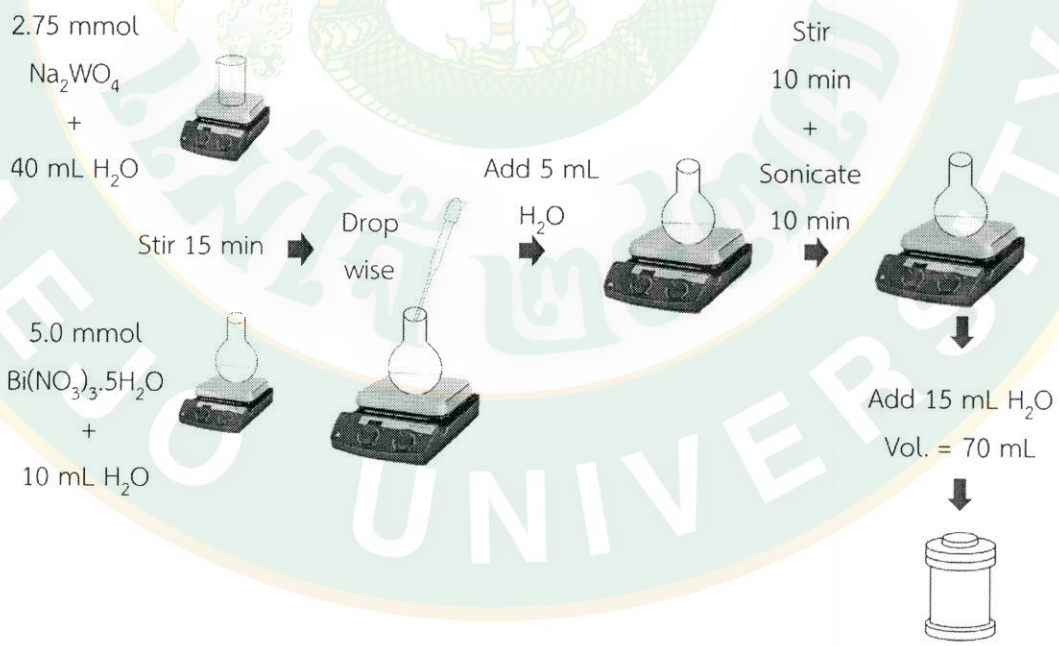

Figure 22 Scheme of synthesis of Bi_2WO_6 via hydrothermal method.

2.3.2 Synthesis of $BiVO_4/Bi_2WO_6$ composites

$BiVO_4/Bi_2WO_6$ composites were synthesized in various $BiVO_4$ mole fractions (Fig. 23(b)) by the same process as in the synthesis of $BiVO_4$ (Fig. 23(a)) which pH value was controlled at 7. After continuously stirring for 1 h, a certainly weight of Bi_2WO_6 powder was added into the mixture. Then, the suspension was stirred for 15 min. After mixing well, some absolute ethanol was added into the mixture to make the final volume 20 mL and transferred to a 100 mL Teflon-lined stainless steel reactor. The ethanol-assisted hydrothermal conditions were controlled by heat treatment at 200 °C for 2 h as showed in Table 10.

Table 10 Synthesis conditions of $BiVO_4/Bi_2WO_6$ composites

Sample	$BiVO_4$: Bi_2WO_6 (mol : mol)	Temperature (°C)	Time (h)
Bi_2WO_6	0 : 1	200	2
$BiVO_4/Bi_2WO_6$_0.5	1 : 1	200	2
$BiVO_4/Bi_2WO_6$ _0.67	1 : 0.50	200	2
$BiVO_4/Bi_2WO_6$ _0.80	1 : 0.25	200	2
$BiVO_4/Bi_2WO_6$ _0.91	1 : 0.10	200	2
$BiVO_4$	1 : 0	200	2

Finally, all synthesized samples were characterized and evaluated their photocatalytic oxygen liberation performance.

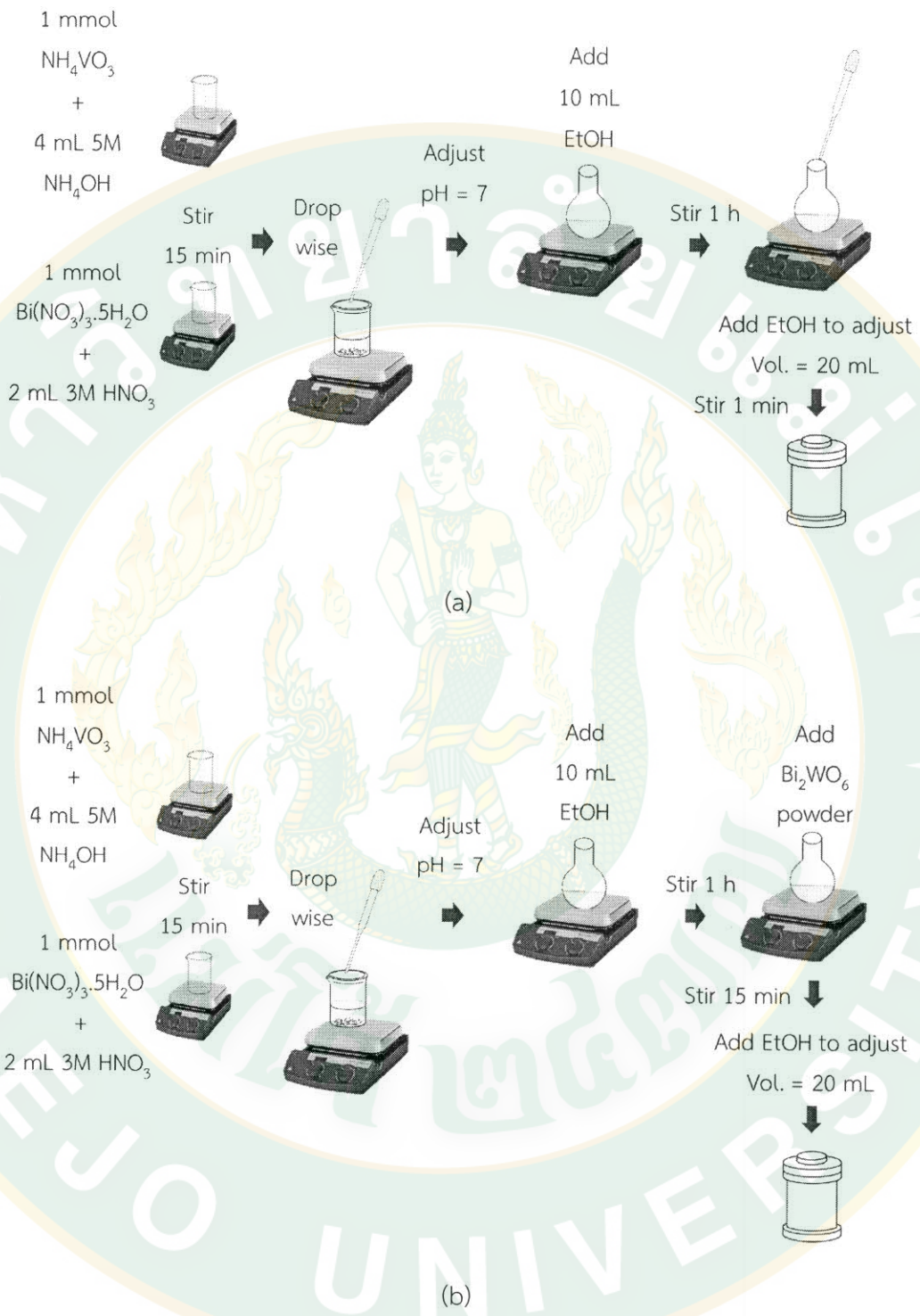

Figure 23 Scheme of synthesis of (a) $BiVO_4$ and (b) $BiVO_4/Bi_2WO_6$ composites via ethanol-assisted hydrothermal method.

3. Characterizations

3.1 X-ray diffraction spectrometry (XRD)

Crystalline structures were analyzed by using XRD. Synthesized sample power was placed on sample holder and pressed with glass slide to make its surface smooth before analysis. The crystalline phase of $BiVO_4$ was determined by X-ray diffractometer using CuK_α radiation (λ = 0.15418 nm), scanning step of 0.02° (2/step/sec) and the monoclinic and tetragonal structure of the $BiVO_4$ and orthorhombic of Bi_2WO_6 were confirmed by comparing JCPDS file no. 14-0688, 14-0133 and 79-2381, respectively.

3.2 Fourier transform infrared spectroscopy (FT-IR)

Synthesized sample power was ground with potassium bromide (KBr) with the ratio of sample: KBr = 1:100. Next, the mixture powder was pressed into a pellet. The pellet was placed on sample holder and analyzed.

3.3 Scanning electron microscopy (SEM)

Morphologies of obtained powders were observed by SEM. Synthesized sample power was ground and dispersed in ethanol by sonication for 10 min. Next, the mixture was dropped on a stup and quickly dried. After that, it was coated by goal at a voltage of 15 kV, placed on sample holder and analyzed. Some samples were observed by another instrument, a field-emission scanning electron microscope (FE-SEM) in secondary-electron image (SEI) mode. The FE-SEM was operated at 5.0 kV electron-acceleration voltage, 10.0 μA current and 5–6 mm working distance. Dried sample powder was placed onto a carbon tap (Okenshoji #15-1096) sticked on a stub (12 mm in diameter; 10 mm in height).

3.4 Surface area analysis

Synthesized sample power were weight to 500 mg in a sample vassel. Pre-heating at 150 °C for 90 min was applied to remove some moisture before measuring surface area of the particles by nitrogen absorption and calculated by Bruauer-Emmett-Teller (BET) method.

3.5 Diffuse reflectance spectroscopy (DRS)

Absorption spectrum was recorded by UV-Vis absorption spectrometer. Barium sulfate was used as white reflectance standard. Then, band gap energy (E_g) was calculated by a Tauc plot from the Kubelka-Munk equation.

3.6 Photoacoustic spectroscopy (PAS)

Energy-resolved density of electron traps (ERDT) and conduction band-bottom position (CBB) were measured by reversed double-beam photoacoustic spectroscopy (RDB-PAS) and single-beam PAS, respectively using home-made RDB-PAS apparatus. The experiment was processed in a glove box under nitrogen gas.

3.7 X-ray absorption spectroscopy (XAS)

Oxidation state of vanadium atoms and mean bonding distance between vanadium and oxygen atoms were studied by X-ray absorption spectroscopy (XAS) technique at the SUT-NANOTEC-SLRI XAS beamline (BL. 5.2), Synchrotron Light Research Institute (SLRI, Nakhon Ratchasima, Thailand). XAS measurements were collected at V K-edge energy (5465 eV) and Bi M_5-edge energy (2580 eV) in transmission mode. The measured XAS data were analyzed using Athena software as implement in the IFEFFIT package (Newville, 2001; Ravel *et al.*, 2005).

4. Photocatalysis studies

4.1 Photodegradation of MO

Photocatalytic activity of $BiVO_4$ samples were studied by decolorization of MO under visible light irradiation using 14W LED lamps as showed in Fig. 24. 0.05 g of $BiVO_4$ photocatalyst was added in 100 mL MO solution (10 ppm) and sonicated for 15 min. After that, it was stirred in dark for 60 min to allow the absorption-desorption equilibrium. Then, a 5 mL of suspension was taken (marked as C_0), centrifuged and filtered. Liquid phase was collected to determined concentrations of the MO by measured absorbance using UV-Vis spectrometer (scanning mode). Next, each 5 mL of the reactant suspension was sampled very 30 min and the absorbance was recorded. Finally, concentration of MO at time, t, was calculate and marked as C_t.

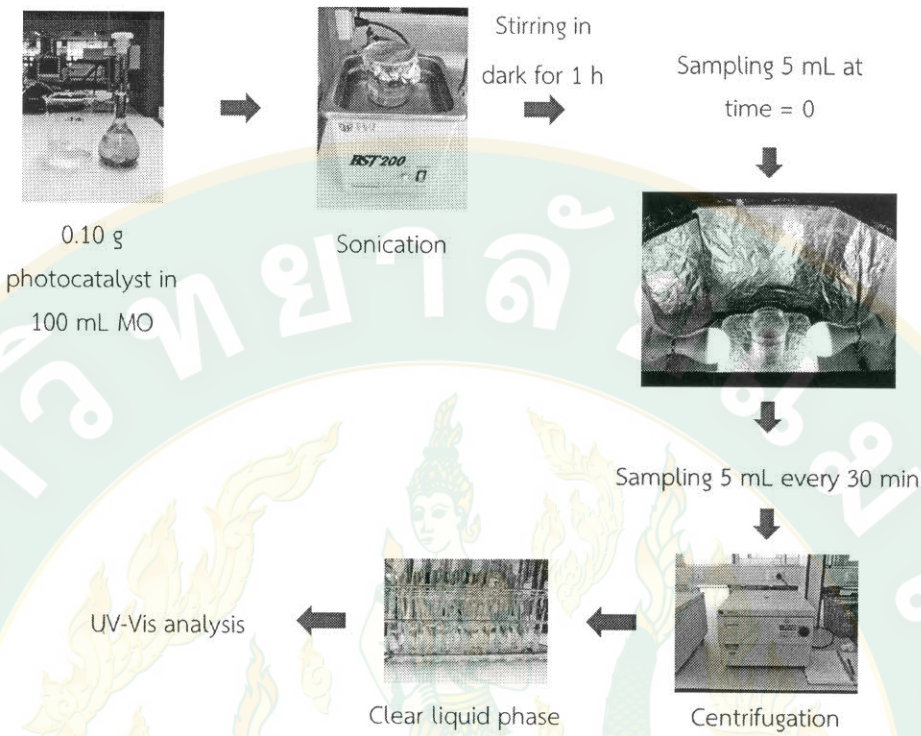

Figure 24 Scheme of photocatalytic methyl orange degradation study.

4.2 Photocatalytic oxygen liberation

Photocatalytic oxygen liberation over $BiVO_4$, Bi_2WO_6 and $BiVO_4/Bi_2WO_6$ composites also studied following the process showed in Fig. 25. A photocatalys was weight for 50 mg and suspended in an aqueous solution of $FeCl_3$ (5.0 mL; 0.25 mmol) in a glass tube. Consequently, sonication for 15 min and argon bubbling for 15 min to purge off air were applied. Next, the suspension was photoirradiated by a UV-Vis lamp (a 400-W high pressure Hg arc lamp) or visible-light (a 300-W Xe lamp with a Y44 cut-off glass filter (Hoya, Japan) transmitting light of wavelength > ca. 420 nm) in a thermostatic bath (25 °C). At every 15 min reaction time, amount of liberated oxygen in the gas phase of a glass tube was measured by a thermal conductivity detector-gas chromatograph (GC-TCD) with a molecular sieve 5A column to calculate the rate of oxygen liberation.

GC conditions:

Injection/Detector	100 °C
Column	80 °C
Current	70 mA
Argon flow	40 mL min^{-1}
Detector	TCD

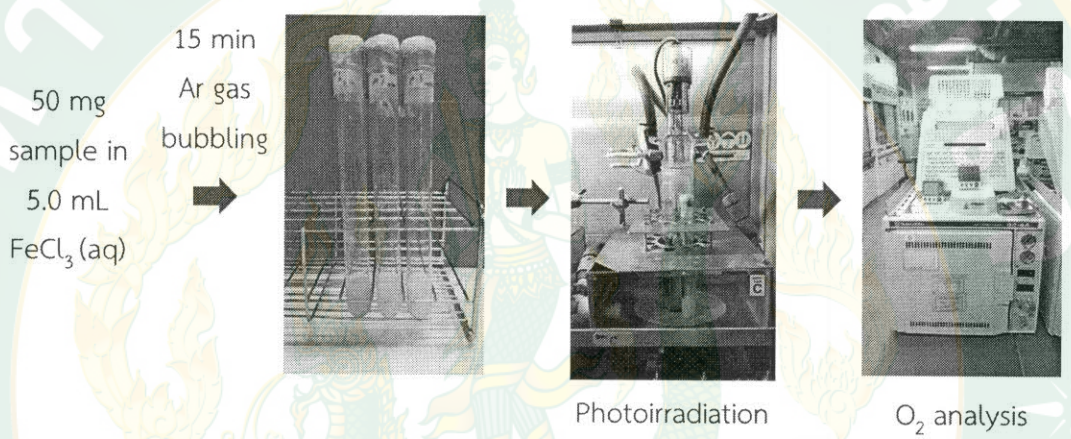

Figure 25 Scheme of photocatalytic oxygen liberation study.

CHAPTER 4

RESULTS AND DISCUSSION

There are mainly two parts described in this chapter. In the first part, effects of synthesis parameters on characteristics of $BiVO_4$ and its photocatalytic degradation of methyl orange (MO) dye are showed and discussed. The optimum synthesis condition is chosen for the next experiments. For another part, characterizations of $BiVO_4/Bi_2WO_6$ composites and their photocatalytic oxygen liberation comparing to pristine $BiVO_4$ and Bi_2WO_6 are subsequently discussed.

Theoretically, synthesis conditions; such as pH of suspension, reaction temperature and reaction time, will impact on crystalline structure as well as morphology of a photocatalyst product. These properties relate to its photocatalytic activity (Dong, Feng *et al.*, 2014; Tan *et al.*, 2013; Zhang *et al.*, 2006). Hence, it is necessary to study some optimize parameters of the synthesis conditions.

1. Effect of pH on characteristic of $BiVO_4$ powder

1.1 Crystalline structure of synthesized $BiVO_4$

During the synthesis of $BiVO_4$, VO_4^{3-} and Bi^{3+} precursors are formed depending on pH values of the suspension. The forming of these precursors influenced crystal structure of the obtained products. Initially, there was no precipitate formed because mixture of the precursors was in strong acid solution (pH = 0). As pH value was increased, red-orange precipitates were formed. Finally, yellow mixture was obtained after pH adjustment to 7. XRD patterns of obtained $BiVO_4$ synthesized by adjusting the before-heating pH values to 6, 7 and 8 were shown in Fig. 26. It was shown that tetragonal structure preferred to obtain in acidic synthesized condition. However, crystalline phase transformed from tetragonal to monoclinic structure by increasing the pH value to 7 and 8. In another word, fraction of ms-phase was increased by increased pH values and the ms-phase usually

obtained at neutral pH. This result related to the previous reports (Wan *et al.*, 2012; Zhang *et al.*, 2012).

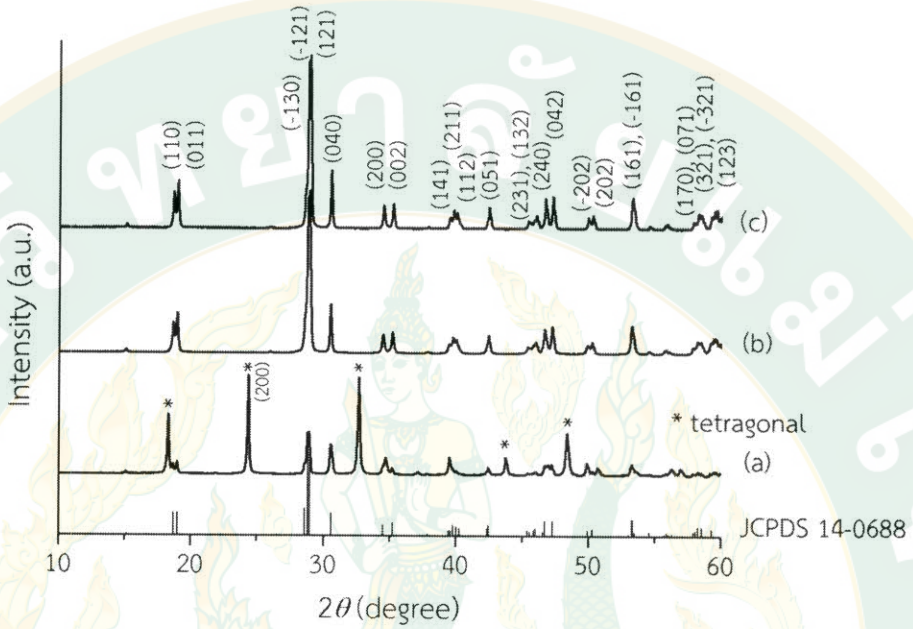

Figure 26 XRD patterns of $BiVO_4$ powder synthesized by ET method at 200 °C for 4 h by adjusting pH to (a) 6, (b) 7 and (c) 8.

1.2 Morphology of synthesized $BiVO_4$

Moreover, the initial pH value has significantly influences morphology of $BiVO_4$ as has been reported by other researchers (Lu *et al.*, 2015; Wan *et al.*, 2012; Zhang *et al.*, 2009). SEM images in Fig. 27 showed morphologies of $BiVO_4$ particles synthesized at pH 6, 7 and 8. Ball-like particles mixed with rod- and plate-like particles were obtained by adjusting pH value to 6 (Fig. 27 (a-b)). The morphology of the $BiVO_4$ particles was changed to nano rod-like particles by adding more ammonium hydroxide solution (NH_4OH (aq)) to adjust pH value to 7 (Fig. 27 (c-d)). In addition, at pH 7, some rods were growth to become bigger size particles. Further adding more NH_4OH until pH = 8, shape of particles were retained with a bigger particles (Fig. 27 (e-f)).

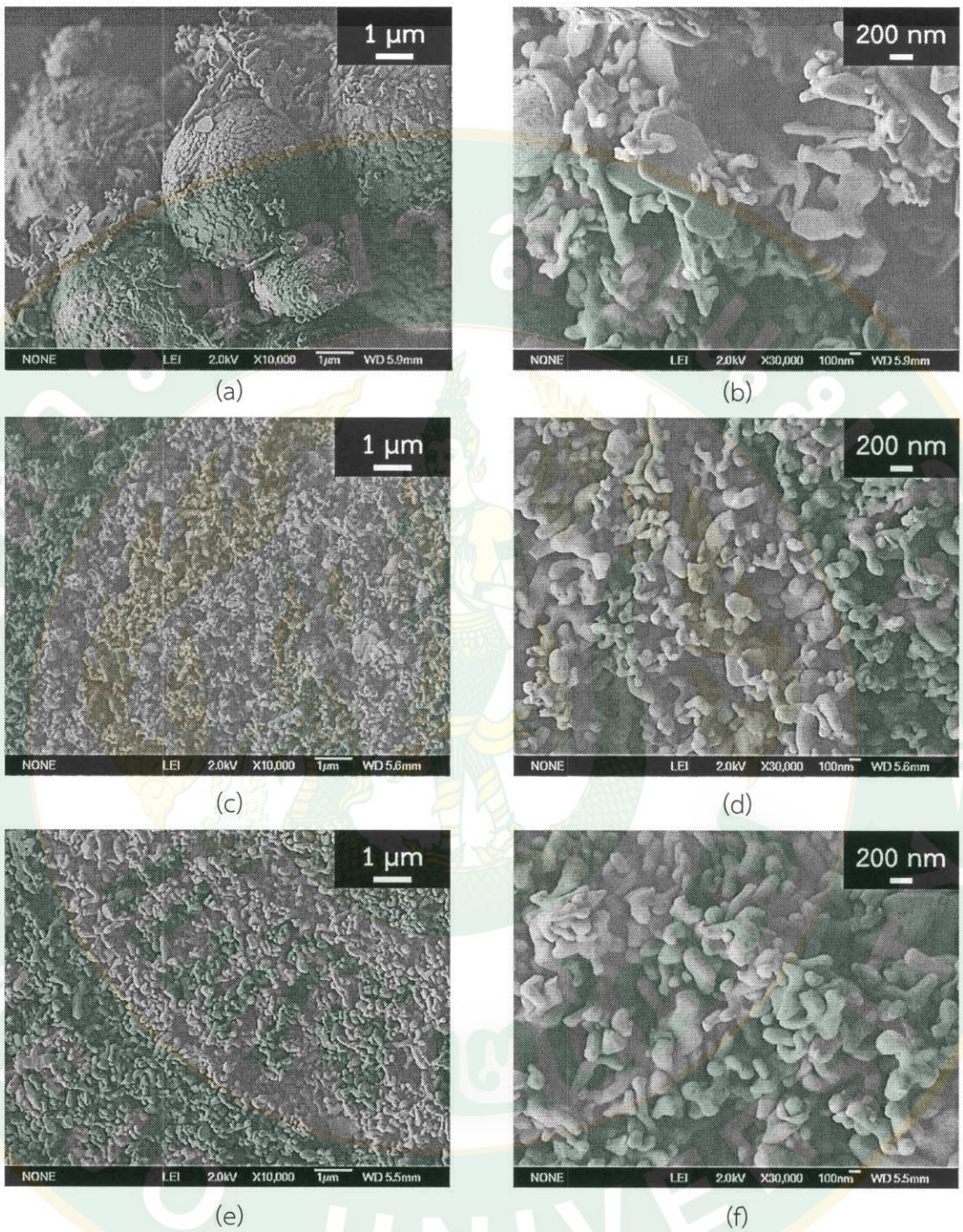

Figure 27 FE-SEM images of $BiVO_4$ synthesized by ET method at 200 °C for 4 h by adjusting pH to (a-b) 6, (c-d) 7 and (e-f) 8.

1.3 Electronic structure of synthesized $BiVO_4$

Optical properties of $BiVO_4$ powders synthesized at various pH conditions were determined by DRS. Kubelka-Munk (K-M) function spectra of the $BiVO_4$ powders in Fig. 28 showed absorption range covering UV and visible region. It could be noticed that curve of pH 6 spectrum had difference from spectra of pH 7 and 8 as well as XRD results that pH 6 showed mixed phases of tetragonal and monoclinic structure while pH 7 and 8 were both pure monoclinic phase.

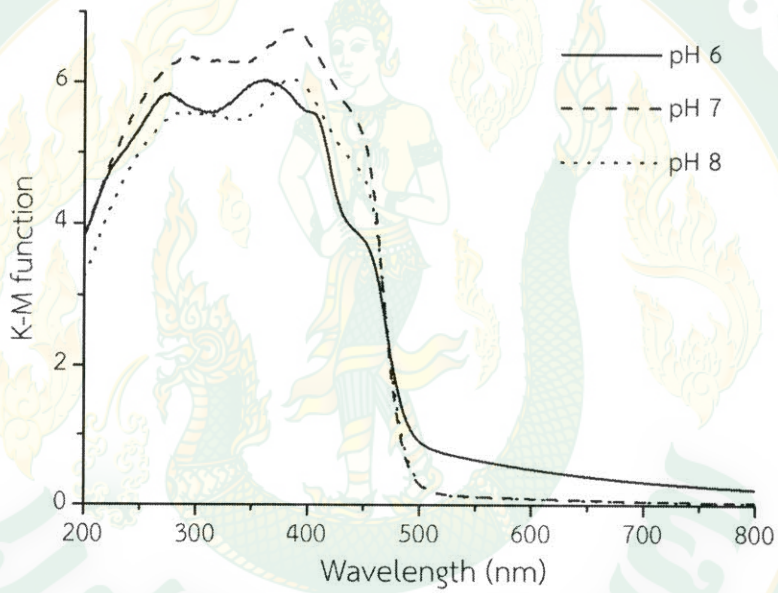

Figure 28 K-M function versus wavelength (nm) spectra of $BiVO_4$ powders synthesized by ET method at 200 °C for 4 h by adjusting pH to 6, 7 and 8.

Furthermore, E_g of $BiVO_4$ powders were determined from Fig. 29 which $(F(R)E)^2$ (calculated from K-M function) and E were plotted. It was found that E_g of the $BiVO_4$ powders were in range of 2.58–2.60 eV.

In addition, XANES spectra of Bi and V measured at M_5-edge and K-edge were shown in Fig. 30 and 31, respectively. Bi in all $BiVO_4$ structures synthesized at pH 6, 7 and 8 showed similar edges position as standards Bi^{3+} (Bi_2O_3) indicating that oxidation state of Bi in the samples were remained in +3 state by varying pH values.

In similar investigation way, edges of V K-edges XANES spectra of the $BiVO_4$ powders appeared near edge of standard V^{5+} (V_2O_5) suggesting the most vanadium in the samples were V in V^{5+} mixed with V^{4+} in minority (Chaurand *et al.*, 2007; Zhai *et al.*, 2013).

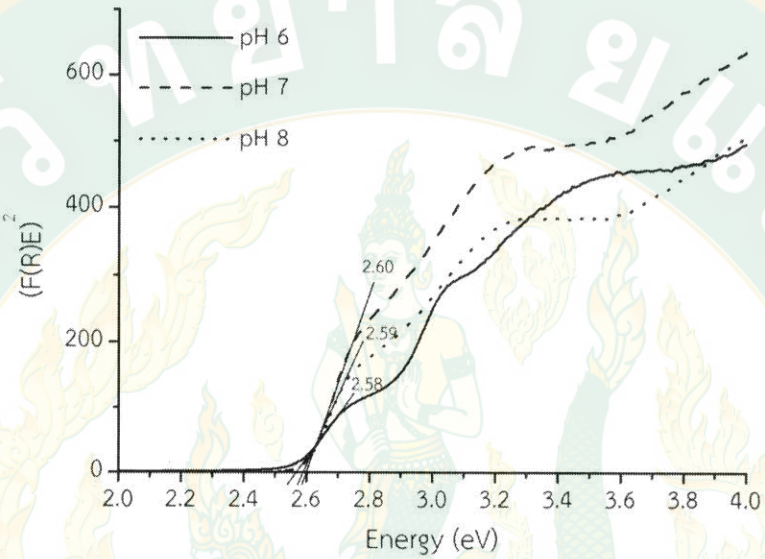

Figure 29 $(F(R)E)^2$ versus energy (eV) spectra of $BiVO_4$ powders synthesized by ET method at 200 °C for 4 h by adjusting pH to 6, 7 and 8.

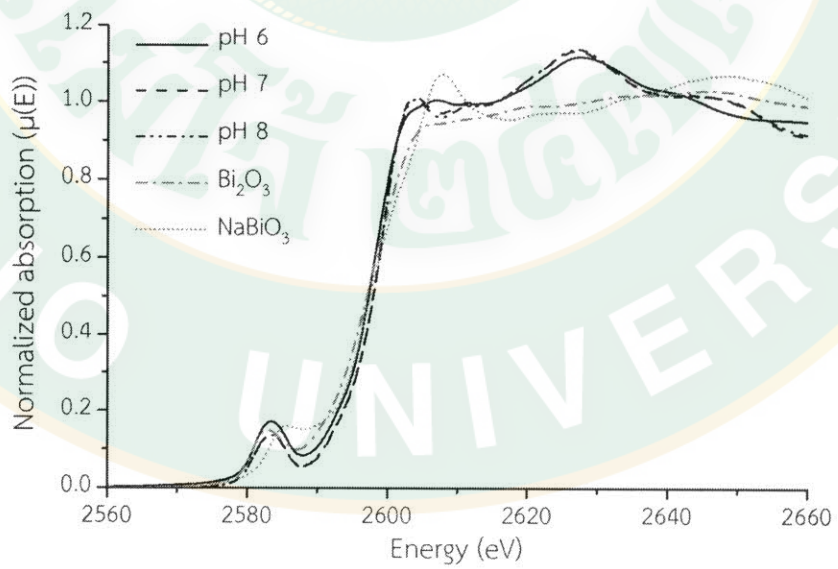

Figure 30 Normalization Bi M5-edge XANES spectra of $BiVO_4$ powders synthesized at 200 °C for 4 h by adjusting pH to 6, 7 and 8.

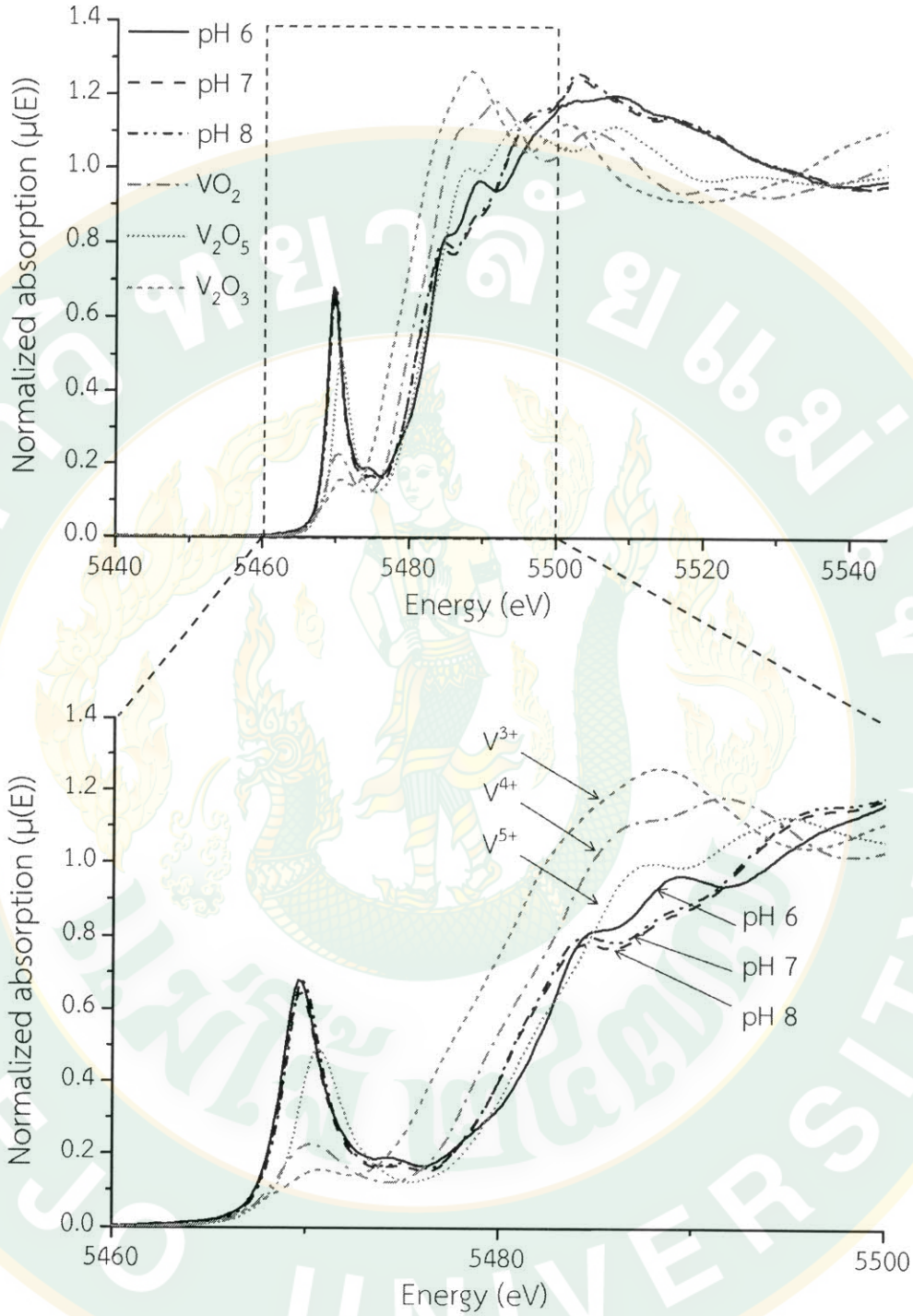

Figure 31 Normalization V K-edge XANES spectra of $BiVO_4$ powders synthesized at 200 °C for 4 h by adjusting pH to 6, 7 and 8 and compared with standard powders of V_2O_3, VO_2 and V_2O_5. The bottom figure is a scale up figure.

V K-edges XANES spectra in Fig. 31 showed that vanadium in pH 6 was composed of V^{5+} while pH 7 and 8 were mixing phases of V^{4+} and V^{5+}. It was also found that, oxidation state results from the V K-edge XANES spectra were corresponding to absorption spectra in Fig. 28. A shift of absorption edge from 520 nm to shorter wavelength described decreasing of V^{5+} concentration (Laorodphan *et al.*, 2016). Moreover, a slightly presence of V^{4+} mixed with V^{5+} on $BiVO_4$ surface with high V^{4+}/V^{5+} molar ratio suggesting high amount of surface oxygen vacancies that could be advantageous for photodegradation of MO (Jiang *et al.*, 2011).

Additionally, V K-edge EXAFS spectra in Fig. 32 showed local structures of the $BiVO_4$ powders synthesized at pH 6-8. It is clearly that the first shell positions of nearest atoms were shifted as increasing pH from 6 to 8. V–O bond distance of $BiVO_4$ synthesized at pH 6, 7 and 8 were 1.25, 1.29 and 1.31 Å, respectively, (no phase shift has been applied to the χ(R) functions). The $BiVO_4$ synthesized at pH 6 showed clearly different characteristic spectrum from pH 7 and 8 indicating different environment around interested V atom.

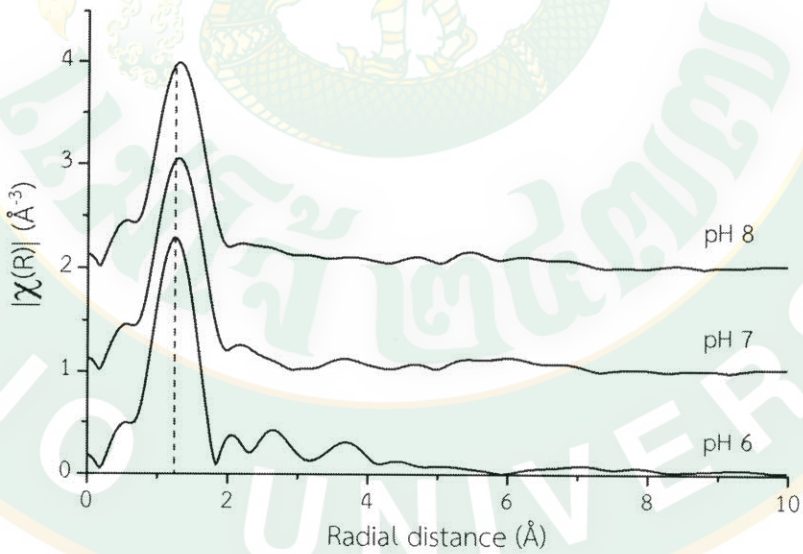

Figure 32 Normalized V K-edge EXAFS spectra of $BiVO_4$ powders synthesized at 200 °C for 4 h by adjusting pH to 6, 7 and 8.

According to above results, it was obviously that pH values affected formation of $BiVO_4$ structure and shape of $BiVO_4$ particles. At different pH values, concentration of precursor ions can be varied, the relevant chemical reactions can be formulated in the suspension. In the acidic condition (pH=1 and 4), the concentration of hydrogen ion (H^+) is high enough to restrain the hydrolysis of $Bi(NO_3)_3$ to $BiONO_3$ (1)-(2), thus Bi^{3+} is the main form (Lu *et al.*, 2015; Opimakh *et al.*, 2014; Zhang *et al.*, 2009). On the other hand, alkalization (in basic solution) of the vanadate solution caused the decavanadate ($V_{10}O_{28}^{6-}$) to decomposed to a lower degree of condensation (3) (Opimakh *et al.*, 2014):

$$Bi^{3+} + 2H_2O \longleftrightarrow Bi(OH)^{2+} + H^+ + H_2O \longleftrightarrow Bi(OH)_2^+ + 2H^+ \quad (1)$$

$$NO_3^- + Bi(OH)_2^+ \longrightarrow BiONO_3\downarrow + H_2O \quad (2)$$

$$V_{10}O_{28}^{6-}\text{ (brown-red)} + OH^- \longrightarrow V_4O_{12}^{4-} + OH^- \longrightarrow V_4O_7^{4-} + OH^- \longrightarrow VO_4^{3-} \quad (3)$$

$$BiONO_3 + VO_3^- \longrightarrow BiVO_4\downarrow + NO_3^- \quad (4)$$

Therefore, monoclinic phase was selectively synthesized by adjusting pH value during the synthesis process.

2. Effect of reaction temperature and reaction time on characteristic of $BiVO_4$ powder

2.1 Appearance of synthesized $BiVO_4$

Reaction temperature and reaction time for ET reaction were controlled at 100 and 200 °C and 2, 4 and 6 h, respectively. Variation in colors of $BiVO_4$ products were showed in Fig. 33. The $BiVO_4$ powder synthesized at 100 °C were bright yellow with no impact of reaction time. However, the bright yellow powder was changed to pale yellow and green-yellow as temperature increased and reaction time was prolonged. These various colors depended on the Bi content (black => low Bi; green yellow => high Bi content) which influenced chemical composition, crystal form, particle size, size distribution and particle morphology (Barreca *et al.*, 1999; Zhang *et al.*, 2006).

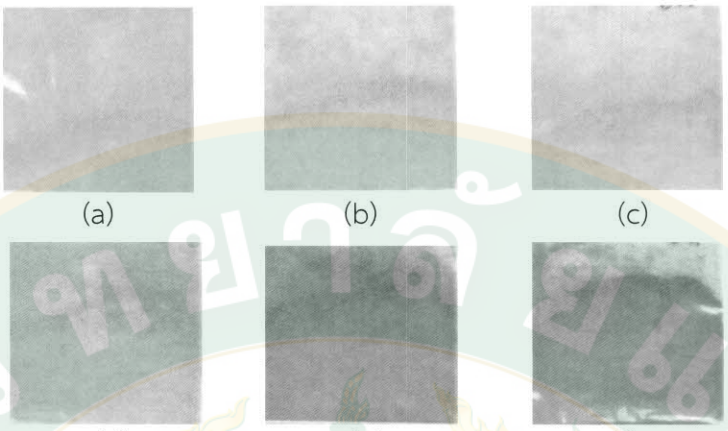

Figure 33 Color of $BiVO_4$ powder synthesized by ET method at 100 °C for (a) 2, (b) 4, (c) 6 h and 200 °C for (d) 2, (e) 4, (f) 6 h.

2.2 Crystalline structure of synthesized $BiVO_4$

Crystalline structure of synthesized $BiVO_4$ powders analyzed by XRD showed that reaction temperature and reaction time played an important role on their crystalline types. X-ray diffraction patterns of synthesized $BiVO_4$ were shown in Fig. 34 and the characteristic peaks were compared with the JCPDS Card No. 14-0133 and 14-0688. The rest of the peaks were assigned to monoclinic (m-) phase $BiVO_4$. It was clearly shown that almost all samples were pure ms-structure excepted the $BiVO_4$ synthesized at 100 °C for 2 h where a small peak at 2θ = 24.4° in Fig. 34(a) corresponded to tetragonal phase. However, the tetragonal phase was found to transfer to monoclinic phase when the synthesized time was increased from 2 h to 4 and 6 h as can be seen an absence of tetragonal peak at 24.4° in Fig. 34(b) and (c), respectively. For the synthesized temperature of 200 °C, crystalline single monoclinic phase of $BiVO_4$ nanoparticle was obtained for all hydrothermal reaction time of 2, 4 and 6 h as seen in Fig. 34(d), (e) and (f), respectively.

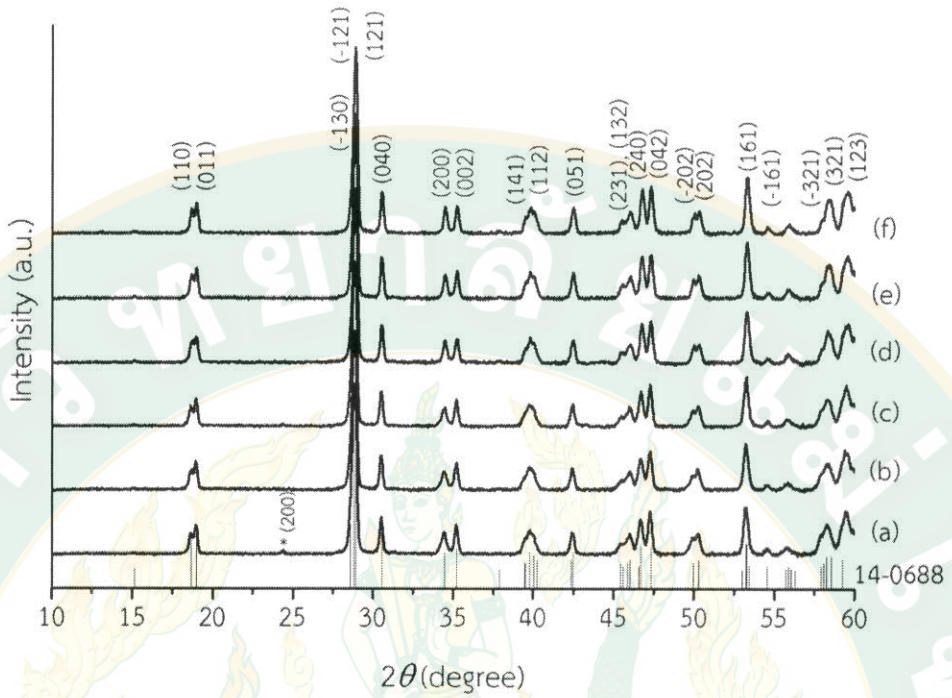

Figure 34 XRD patterns of $BiVO_4$ powder synthesized by ET method at 100 °C for (a) 2, (b) 4, (c) 6 h and 200 °C for (d) 2, (e) 4, (f) 6 h.

Crystalline characteristics of $BiVO_4$ powders synthesized by ET method were summarized in Tables 11. The percentage of the m-phase in the $BiVO_4$ structure was calculated by ratio of intensity of (121) peak of m-structure (I_{mono}) and summary of I_{mono} and intensity of (200) peak of t-structure (I_{tetra}). The $BiVO_4$ nanoparticle synthesized at 100 °C for 2 h consisted of 3 % of tetragonal phase while further increasing of reaction time and reaction temperature developed the crystalline structure to ms-strucuture. Approximate crystalline sizes of a single monoclinic phase of $BiVO_4$ synthesized at 100 °C and 200 °C were calculated by the Scherrer equation (Bhattacharya *et al.*, 1997; Ohtani, 2008). It was found that the crystalline sizes were increased at a higher temperature and prolonger processing time. In addition, the crystalline structures of $BiVO_4$ synthesized in this work were extremely smaller than other $BiVO_4$ crystals synthesized by other methods, e.g. homogeneous precipitation (Yu *et al.*, 2009) hydrothermal (HT) and surfactant-assisted hydrothermal (Zhang and Zhang, 2009a).

Table 11 Crystalline characteristic of $BiVO_4$ powder synthesized by ET method at 100 °C and 200 °C for 2–6 h

Temperature	Reaction time (h)	Percentage of ms-phase	Crystalline size (nm)	Stretching of V–O bond (cm^{-1})
100 °C	2	97	23	729
	4	100	23	737
	6	100	23	726
200 °C	2	100	24	735
	4	100	25	742
	6	100	25	744

IR spectrum showed in Fig. 35 that peak position and characteristic peaks were corresponded to ms-phase of $BiVO_4$ (Ke *et al.*, 2009) and related to XRD results. The IR characteristic peaks were summarized in Table 12. Small peaks at 474 cm^{-1} were corresponding to VO_4^{3-} stretching. Moreover, the sharp peaks (732–740 cm^{-1} and 828–836 cm^{-1}) were asymmetric and symmetric stretching of V–O bonding, respectively (Gotić *et al.*, 2005; Ke *et al.*, 2009). A minor shift of the V–O bands to higher frequency was suggested corresponding to distortion of VO_4 tetrahedral structure, thus changed electronic structure and photocatalytic activity of the $BiVO_4$ (Ding *et al.*, 2013; Thalluri *et al.*, 2013; Zhang and Zhang, 2009b).

In addition, the symmetric V–O frequencies were increased along with the asymmetric V–O by increasing heating temperature to 200 °C as shown in Fig. 35 (d)-(f). It has been reported that high temperature (180 °C, 24 h) solvothermal synthesis of the ms-$BiVO_4$ using polyethylene glycol (PEG 2000) with V–O band located at higher wavenumber trended to improve the photocatalytic performance. $BiVO_4$ with 732 cm^{-1} stretching were found to decolorize over 90% rhodamine B (RhB) under visible light in 180 min (Lin *et al.*, 2014). In addition, the band at 2345 cm^{-1} was assigned to carbon dioxide (CO_2) impurity from atmosphere. From results has discussed above, $BiVO_4$ nanoparticle synthesized via low temperature ET method may be a candidate for photocatalytic dye degradation. Further investigation of V–O

distance of $BiVO_4$ will be discussed in the part of electronic structure of synthesized $BiVO_4$ powder.

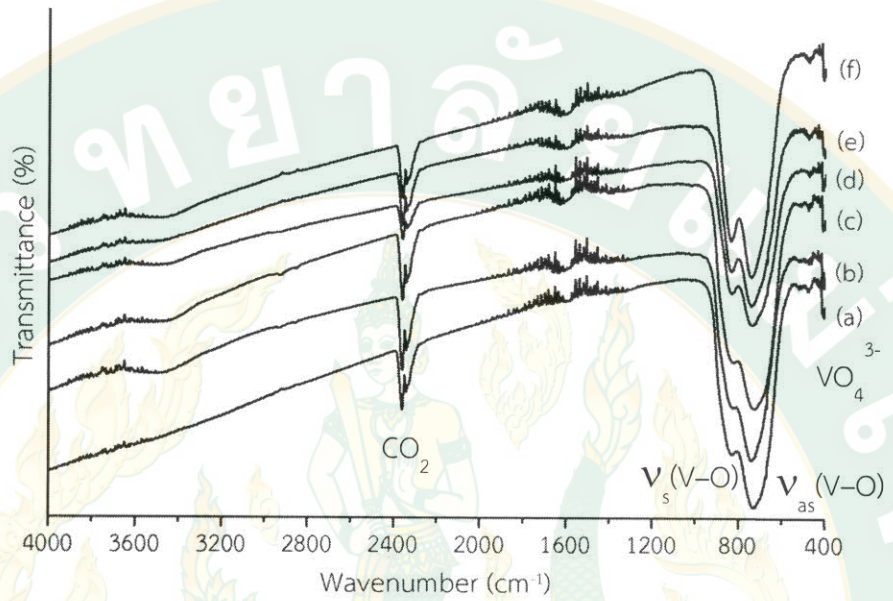

Figure 35 FT-IR spectra of $BiVO_4$ nanoparticle synthesized by ET method at 100 °C for (a) 2, (b) 4, (c) 6 h and 200 °C for (d) 2, (e) 4, (f) 6 h.

Table 12 IR characteristics of $BiVO_4$ powder synthesized by ET method

Molecular motion	Wavenumber (cm^{-1})					
	100 °C			200 °C		
	2 h	4 h	6 h	2 h	4 h	6 h
VO_3^{4-}	474	474	474	474	474	474
as(V-O)	732	736	734	738	740	733
s(V-O)	870	870	870	870	870	870
NO_3^-	1394	1394	1394	-	-	-

2.3 Morphology of synthesized $BiVO_4$

Morphology of synthesized $BiVO_4$ powder was showed in Fig. 36. FE-SEM images of $BiVO_4$ particles synthesized at 100 °C and 200 °C for 2–6 h were different in their particle size and shape. It can be seen that particle size of $BiVO_4$ was increased as the heat-treated time increased. The of $BiVO_4$ particle synthesized at 100 °C for 2 h were agglomerate and irregular in shapes. Fig. 36 (a) illustrated polygon large and thick particle with particle sizes range between 200 nm – 1 μm similar to the ms-$BiVO_4$ prepared precipitation method that need three-day crystallization (Saison *et al.*, 2011). Longer heating enhanced narrower particle size distribution and smaller particles as seen in Fig. 36 (b) due to rearrangement of crystalline structure to be the ms-crystal (Ke *et al.*, 2009; Zhang *et al.*, 2007). Continuously, the particles formed larger particles as the processing time increased to 6 h. Moreover, $BiVO_4$ nanoparticle synthesized at 200 °C for 2–6 h was showed rod-like particle growth with circular grain (Fig. 36 (d)-(f)). As prolong heat-treated time, the larger and longer particle could be obtained related to previous report (Zhang *et al.*, 2007). According to the morphology that played important role in photocatalytic activity (Jiang *et al.*, 2011; Lei *et al.*, 2014), controllable T-shape monoclinic $BiVO_4$ synthesized by structure-directing surfactant assisted hydrothermal were reported (Dong, Yu *et al.*, 2014). T-shape monoclinic $BiVO_4$ with 0.5 μm width and 2 μm length was obtained and showed higher decolorization rate of methylene blue (MB) solution than commercial P25 under visible-light irradiation. As this work, synthesis condition played important role on $BiVO_4$ morphology. The similar morphology and smaller particles of the $BiVO_4$ synthesized by ET method might be a high performance candidate for MB dye degradation application.

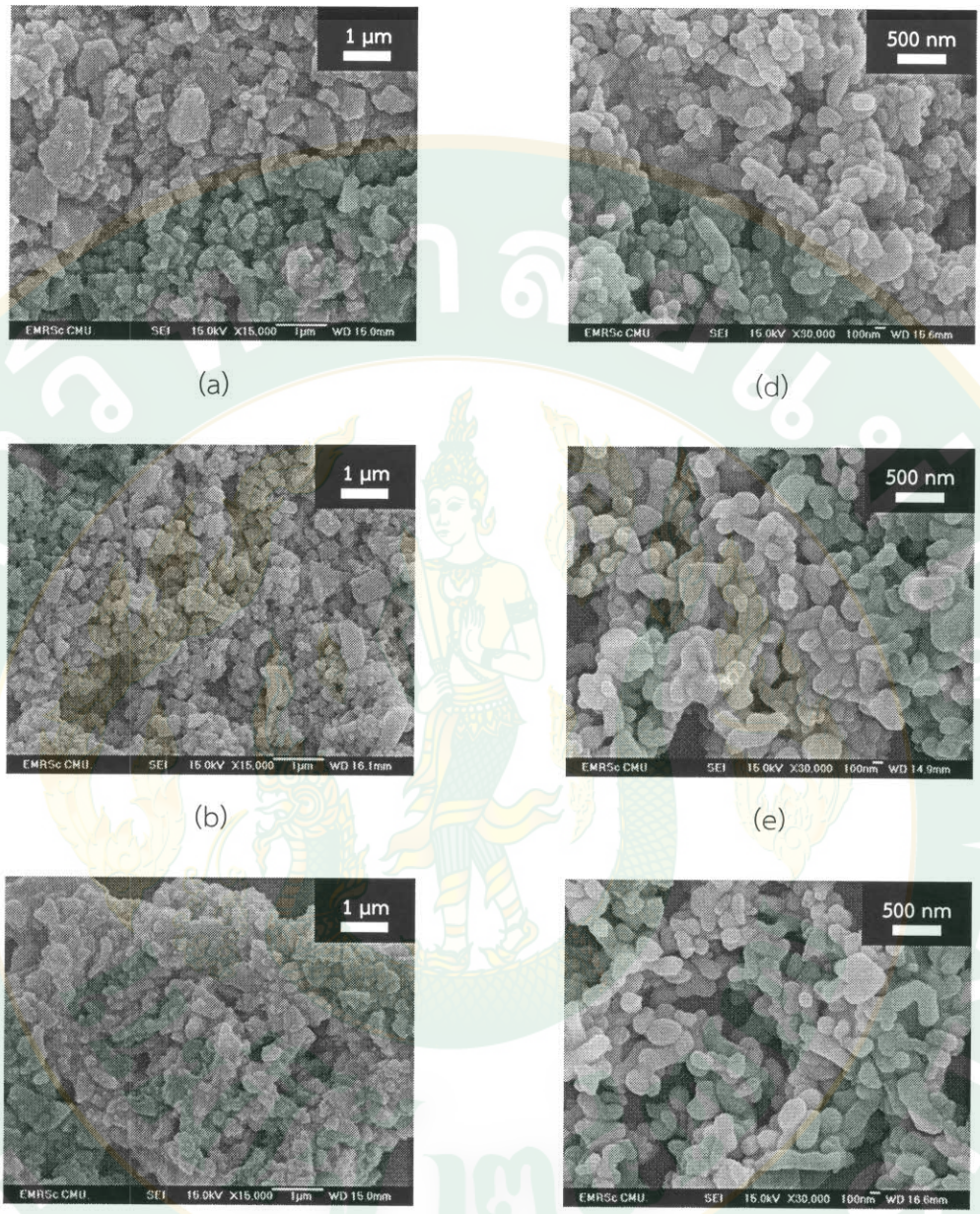

Figure 36 FE-SEM images of $BiVO_4$ synthesized by ET method at 100 °C for (a) 2, (b) 4, (c) 6 h and 200 °C for (d) 2, (e) 4, (f) 6 h.

2.4 Surface area of synthesized $BiVO_4$

Specific surface areas (SSA) of $BiVO_4$ powders synthesized by ET method were proved and showed in Table 13. The SSA increased as reaction time increased

and higher reaction temperature improved the surface area. However, decreasing of surface area for 200 °C 6 h was due to particle growth and became a larger particle.

Table 13 Physical properties of $BiVO_4$ synthesized by ET method in various synthesis conditions

Reaction Temperature (°C)	Reaction time (h)	Morphology	SSA[a] ($m^2 \cdot g^{-1}$)	E_g (eV)	V-O bond distance[b] (Å)
100	2	Irregular	6.80	2.58	1.28
	4	Irregular	5.69	2.59	1.45
	6	Irregular	7.56	2.58	1.32
200	2	Rod	8.79	2.59	1.24
	4	Rod	9.80	2.57	1.36
	6	Rod	7.74	2.57	1.38

[a] Specific surface area

[b] No phase shift (0.2–0.3 Å) was applied

NA = Not analysis

2.5 Electronic structure of synthesized $BiVO_4$

In order to study reaction temperature and reaction time effects on electronic structures of $BiVO_4$ powders synthesized by ET method, optical property of the $BiVO_4$ was determined. K-M function spectra of $BiVO_4$ powders in various synthesis conditions (Fig. 37) showed that the spectra covered UV and visible regions (200–500 nm). It can be suggested that these $BiVO_4$ powders were monoclinic structure related to XRD results (Tokunaga *et al.*, 2001). Band gap energy (E_g) of $BiVO_4$ was evaluated from Tauc plot by a Kubelka-Munk function. The E_g values of the $BiVO_4$ powders were ranged from 2.57 to 2.59 eV for ET synthesis as summarized in Table 13.

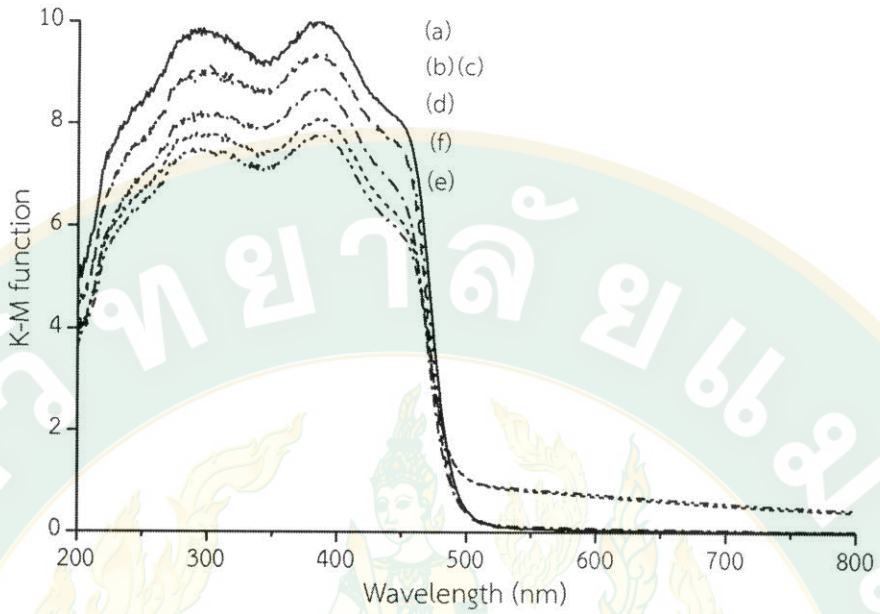

Figure 37 K-M function versus wavelength (nm) spectra of $BiVO_4$ powder synthesized by ET method at 100 °C for (a) 2, (b) 4, (c) 6 h and 200 °C for (d) 2, (e) 4, (f) 6 h.

Furthermore, oxidation state of vanadium (V) and bond length between vanadium atom and oxygen atom (V–O) were determined by XAS. X-ray absorption near-edge (XANE) characteristics of the $BiVO_4$ were compared with vanadium oxide standards (V_2O_3 and V_2O_5 for V^{3+} and V^{5+}, respectively) as showed in Fig. 38. Noticeably, shift of pre-edge positions represented different in energy states of excited electrons while the edge overlapped each other near V_2O_5 (V^{5+}) indicated that the oxidation state of vanadium in the $BiVO_4$ structures were reduced from +5 to +4 (Zhai *et al.*, 2013). These results were related to above-absorption spectrum in Fig. 37 as it had already described in the previous part.

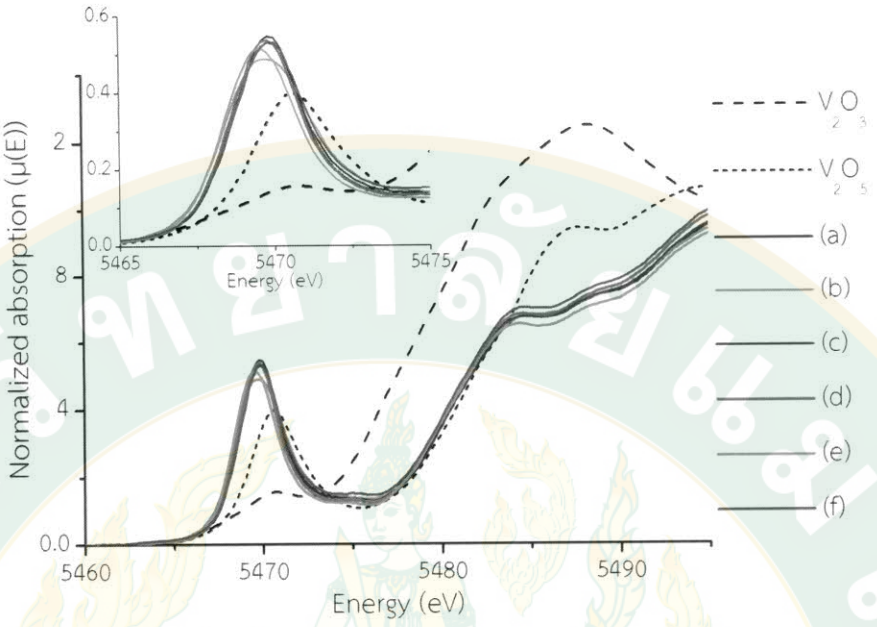

Figure 38 Normalization V K-edge XANES spectra of $BiVO_4$ synthesized at 100 °C for (a) 2, (b) 4, (c) 6 h and 200 °C for (d) 2, (e) 4, (f) 6 h. μ(E) is X-ray absorption coefficient.

On the other hand, V–O bond distances were calculated from Extended X-Ray Absorption Fine Structure (EXAFS) characteristics. A V–O bond distance was examined as the first shell distance from V atom in term of R-space. Figure 39 showed normalized V K-edge EXAFS spectra of $BiVO_4$ synthesized at 100 and 200 °C for 2–6 h. The first highest loop of spectrum was the distance between V and O atoms could be determined and showed in Table 13. It is noted that no phase shift has been applied to the χ(R) functions, thus the peak position of χ(R) functions will be shifted from the actual value by approximately 0.2–0.3 Å. The spectrum of $BiVO_4$ powder synthesized at 100 °C 2 h looked different from other synthesized conditions suggesting that environment of V atom in the $BiVO_4$ was different from other. This result corresponded to XRD diffraction pattern in Fig. 34 (a), where it showed an impurity peak of tetragonal phase which V atoms were located differently comparing to monoclinic phase (see Fig. 3). As prolonging reaction time, EXAFS spectrum of $BiVO_4$ powder synthesized at 100 °C 4 h showed similar pattern as 2 h (Fig. 39 (a)) but V–O bond distance was increased. Further increasing of reaction time to 6 h, EXAFS

characteristic was changed again. In addition, increasing of heating temperature to 200 °C showed other different patterns and lengthening occurred from 1.24 to 1.38 Å after prolongation from 2 to 6 h, respectively. Nevertheless, V–O bond lengths obtained from $BiVO_4$ powders synthesized at 200 °C resembled to previous report that V–O bond lengths of the monoclinic $BiVO_4$ from experimental value were 1.692 and 1.767 Å as well as from theoretical calculation using the density functional theory (DFT) were 1.718 and 1.769 Å (Ding *et al.*, 2013).

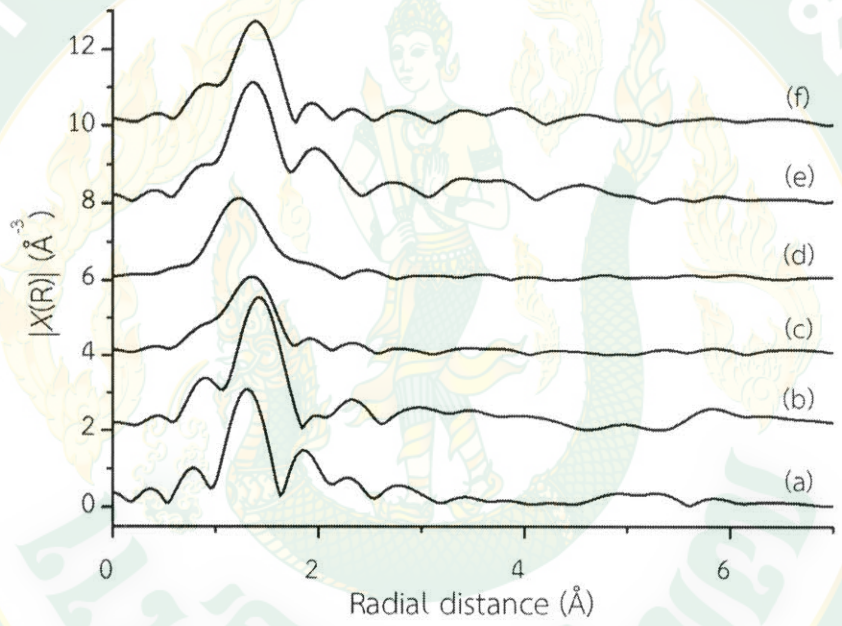

Figure 39 Normalized V K-edge EXAFS spectra of $BiVO_4$ synthesized at 100 °C for (a) 2, (b) 4, (c) 6 h and 200 °C for (d) 2, (e) 4, (f) 6 h.

3. Photocatalytic activity of $BiVO_4$

3.1 Photodegradation of MO dye over $BiVO_4$

Photocatalytic efficiency of $BiVO_4$ powders synthesized in various pH values on MO dye degradation showed in Fig. 40. Ratio of MO concentration at time (C_t) and initial concentration (C_0) was calculated and plotted with light irradiation time. As the results, It could be seen clearly that the $BiVO_4$ samples obtained at

different pH values exhibited different photocatalytic activities (Lu *et al.*, 2015). $BiVO_4$ obtained by adjusting pH to 7 was the most effective photocatalyst in this case.

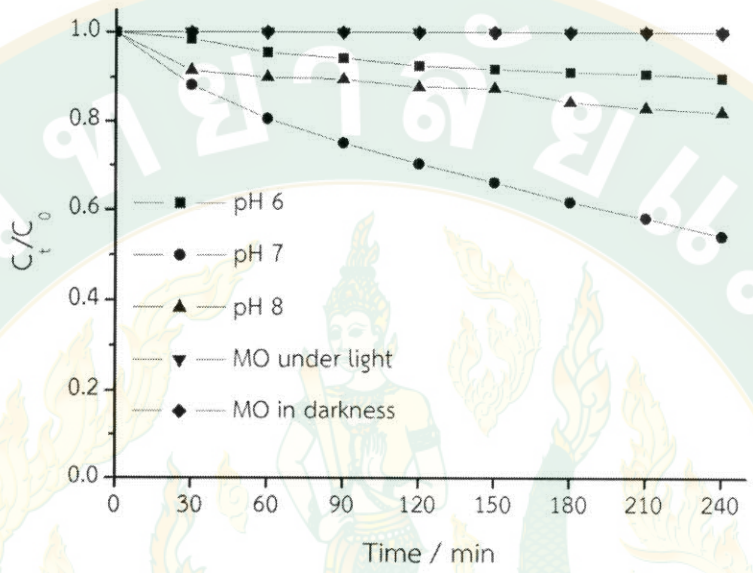

Figure 40 Photodegradation under LED lamps using $BiVO_4$ synthesized at pH 6–8 and heating at 200 °C for 4 h.

Characteristics of $BiVO_4$ photocatalysts were changed by pH adjustment in synthesis process. Influences of the characteristics on photocatalytic performance of the $BiVO_4$ powder were showed in Fig. 41. In summary, the highest photocatalytic activity was obtained by $BiVO_4$ with pure monoclinic structure, large SSA, small crystalline size and short V–O bond distance. Thus, photocatalytic activity could be controlled by adjusting pH.

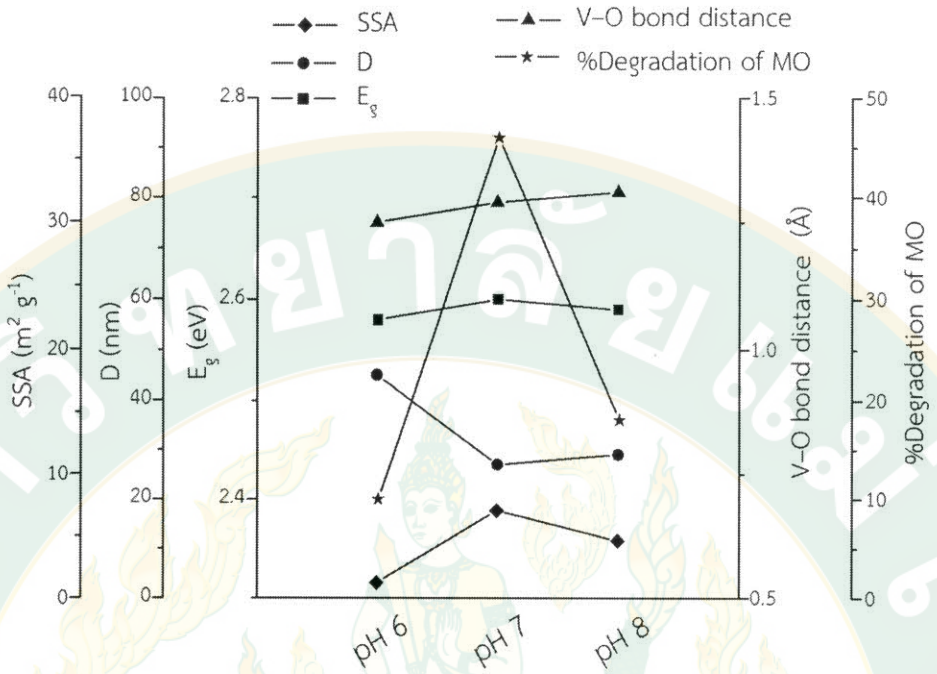

Figure 41 Characteristics and photocatalytic activities of $BiVO_4$ powders synthesized at pH 6–8.

Photocatalytic efficiency of $BiVO_4$ powders synthesized in various reaction temperatures and reaction times on MO dye degradation showed in Fig. 42. All photocatalyst samples were stirred in darkness for 60 min before light irradiation in order to make absorption equilibrium. It was clearly that the $BiVO_4$ synthesized by ET method showed significantly better photocatalytic activity than hydrothermal (HT) method (Fig. 42 (g)) at the same pH, reaction temperature and reaction time. Notably, no MO degradation in dark as well as MO solution with $BiVO_4$ in dark and MO with light were remained even after light irradiation for 240 min. Photocatalytic activities of ET-$BiVO_4$ were followed: 100 °C 2 h = 100 °C 4 h = 200 °C 2 h < 100 °C 6 h < HT < 200 °C 4 h < 200 °C 6 h. $BiVO_4$ synthesized at 200 °C for 6 h showed highest photocatalytic efficiency of 16% MO degradation in 240 min.

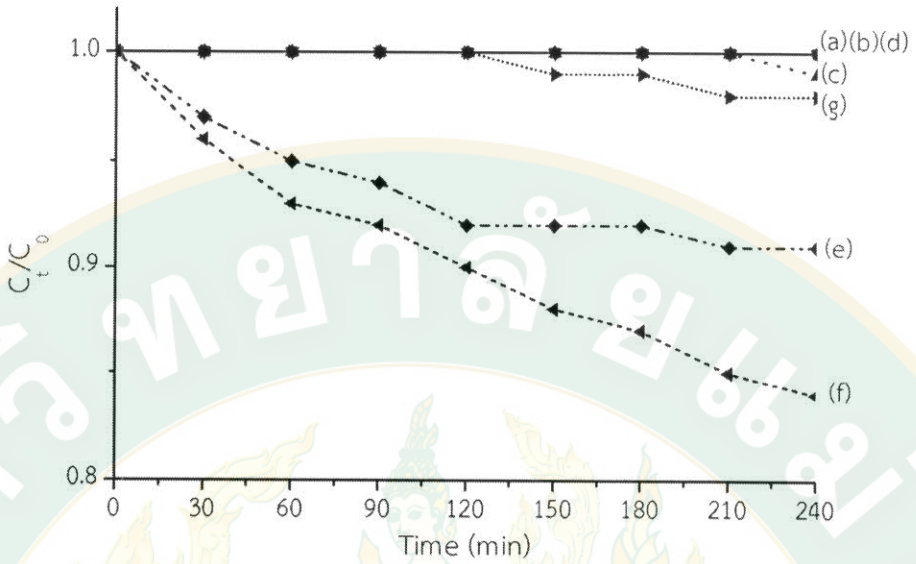

Figure 42 Photodegradation of MO under visible light using $BiVO_4$ synthesized at 100 °C (a) 2, (b) 4, (c) 6 h and 200 °C for (d) 2, (e) 4, (f) 6 h comparing with $BiVO_4$ synthesized by (g) HT method.

3.2 Photocatalytic oxygen liberation of $BiVO_4$

Photocatalytic oxygen liberation of $BiVO_4$ powder synthesized in various reaction temperatures and reaction times were also studied for the real photocatalysis through photoexcitation of a photocatalys, not electron injection from dye molecule through photoabsorption (Ohtani, 2016; Yan *et al.*, 2006). Figure 43 showed amount of oxygen liberation in average (number of data = 2) after UV-Vis light irradiation (400W Hg arc lamp) for 240 min that $BiVO_4$ synthesized at 200 °C for 2 h exhibited the highest amount of oxygen gas.

In Fig. 44, reaction temperature and reaction time played role on characteristics of synthesized $BiVO_4$ especially V–O bond distance. Correlation of photocatalytic activities of the as-prepared $BiVO_4$ samples and their characteristic parameters were clearly illustrated that the major factors influenced photocatalytic activity of the $BiVO_4$ were V–O bond distance and SSA. The best oxygen liberation efficiency was obtained by the $BiVO_4$ with the shortest V–O bond distance and large SSA.

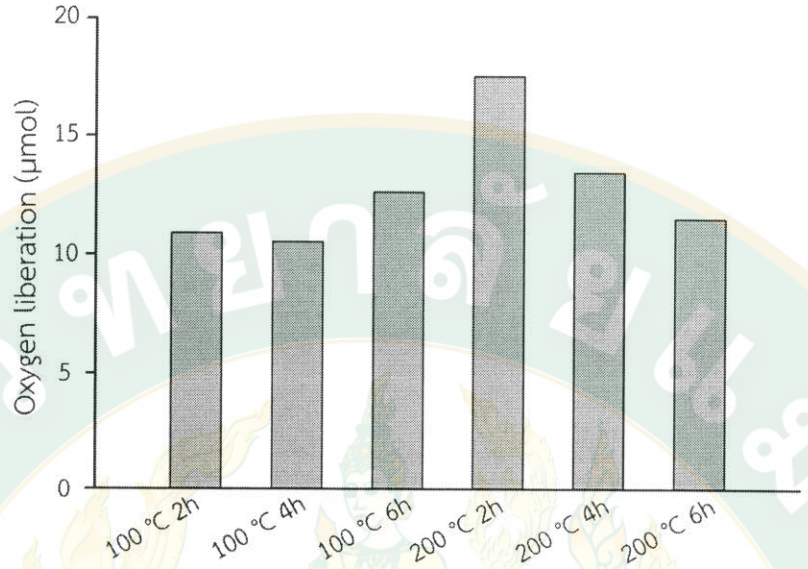

Figure 43 Photocatalytic oxygen liberations under UV-visible light using $BiVO_4$ synthesized by ET method at 100 °C and 200 °C for 2–6 h.

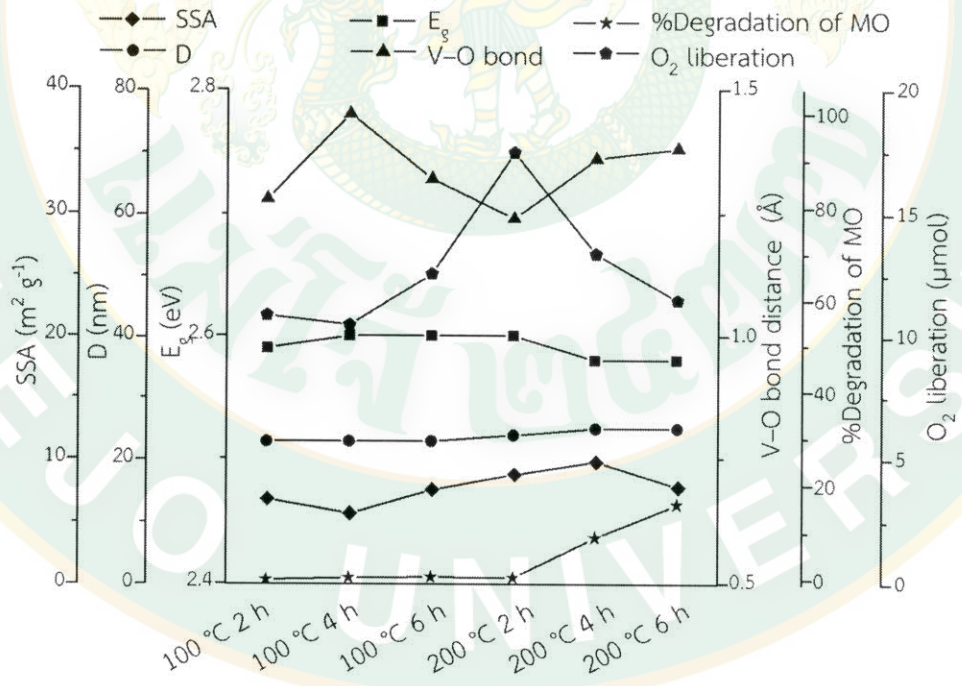

Figure 44 Characteristics and photocatalytic activities of $BiVO_4$ powders synthesized by ET method at 100 °C and 200 °C for 2–6 h.

All physical properties and photocatalytic activities results (numerical data) of the obtained $BiVO_4$ powders were summarized in Table 14. It could be concluded that crystalline structure, SSA and V–O bond distance had high impacts on photocatalytic activity of the $BiVO_4$. These factors were simply controlled by adjusting pH value of suspension before heating, reaction temperature and reaction time. However, photocatalytic activity of a $BiVO_4$ sample can be improved by modification such as adding other metal oxide to construct a composite.

Table 14 Physical properties and photocatalytic activities of $BiVO_4$ powder synthesized by ET method with various conditions

Sample	Heating time (h)	%ms-phase	D[a] (nm)	Stretching of V–O bond (cm^{-1})	Morphology	E_g (eV)	V-O bond distance (Å)	SSA[b] ($m^2 \cdot g^{-1}$)	%Degradation of MO	Oxygen liberation (μmol)
pH 6	4	30	45	NA	Ball	2.58	1.25	1.24	10[c]	NA
pH 7	4	100	27	NA	Rod	2.60	1.29	7.05	46[c]	NA
pH 8	4	100	29	NA	Rod	2.59	1.31	4.60	18[c]	NA
100 °C	2	97	23	732	Irregular	2.59	1.28	6.80	0	10.9
	4	100	23	736	Irregular	2.60	1.45	5.69	0.45	10.5
	6	100	23	734	Irregular	2.60	1.32	7.56	0.56	12.6
200 °C	2	100	24	738	Rod	2.60	1.24	8.79	0.45	17.5
	4	100	25	740	Rod	2.58	1.36	9.80	9.0	13.4
	6	100	25	733	Rod	2.58	1.38	7.74	16	11.5

[a] Crystalline size of $BiVO_4$ were calculated from (121) XRD peaks by the Scherrer equation. [b] Specific surface area. [c] Photocatalyst 1 g L^{-1} under 14W LED lamp. [d] Photocatalyst 0.5 g L^{-1} under 14W LED lamp for 4 h. [e] Photocatalyst 10 g L^{-1} under 300W Xe lamp with a Y44 UV cut-off window for 4 h.

4. Characterization of $BiVO_4/Bi_2WO_6$ composites

4.1 Appearance of $BiVO_4/Bi_2WO_6$ composite

Color of a $BiVO_4/Bi_2WO_6$ composite with *f*(V) of 0.8 was presented in brighten yellow while Bi_2WO_6 and $BiVO_4$ powder were pale yellow and brighten yellow, respectively, as shown in Fig. 45. Their color were not changed by calcination at 600 °C for 4 h, excepted the shade of c-$BiVO_4$ could became a little darker than uncalcined $BiVO_4$.

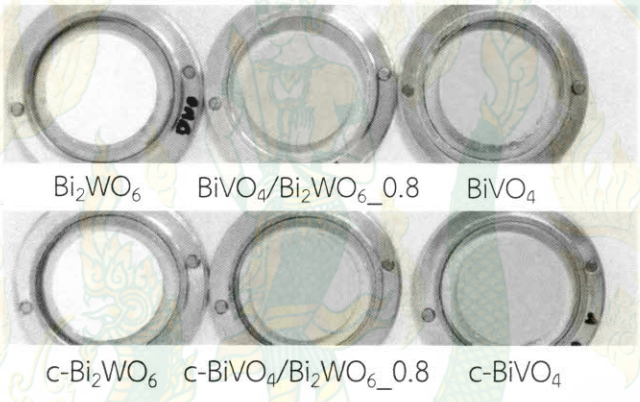

Figure 45 Colors of uncalcined and calcined Bi_2WO_6, $BiVO_4$ and $BiVO_4/Bi_2WO_6$_0.8 composites powder.

4.2 Crystalline structure

Crystalline phase structures of uncalcined and calcined pristine Bi_2WO_6, $BiVO_4$ and $BiVO_4/Bi_2WO_6$ composites were analyzed by XRD as shown in Fig. 46. As expected, XRD patterns of Bi_2WO_6 (Fig. 46A (a)) and $BiVO_4$ (Fig. 46A (f)) were defined as orthorhombic (JCPDS file No. 79-2381) and monoclinic (JCPDS file No. 14-0688) structure, respectively, without an impurity peak. Diffraction peaks of $BiVO_4/Bi_2WO_6$ composites showed that the structures of the composites were constructed of monoclinic phase of $BiVO_4$ and orthorhombic phase of Bi_2WO_6. Reasonably, peaks intensities respected to $BiVO_4/Bi_2WO_6$ mole ratio as shown in Fig. 46A (b)-(e). Crystalline phases after calcination at 600 °C for 4 h of all samples were unchanged as showed in Fig. 46B. In contrast, peak intensities were greatly increased indicating

that crystallinities of all samples were improved. Moreover, increasing of crystalline sizes after calcination as shown in Table 15 indicated crystalline growth by calcination.

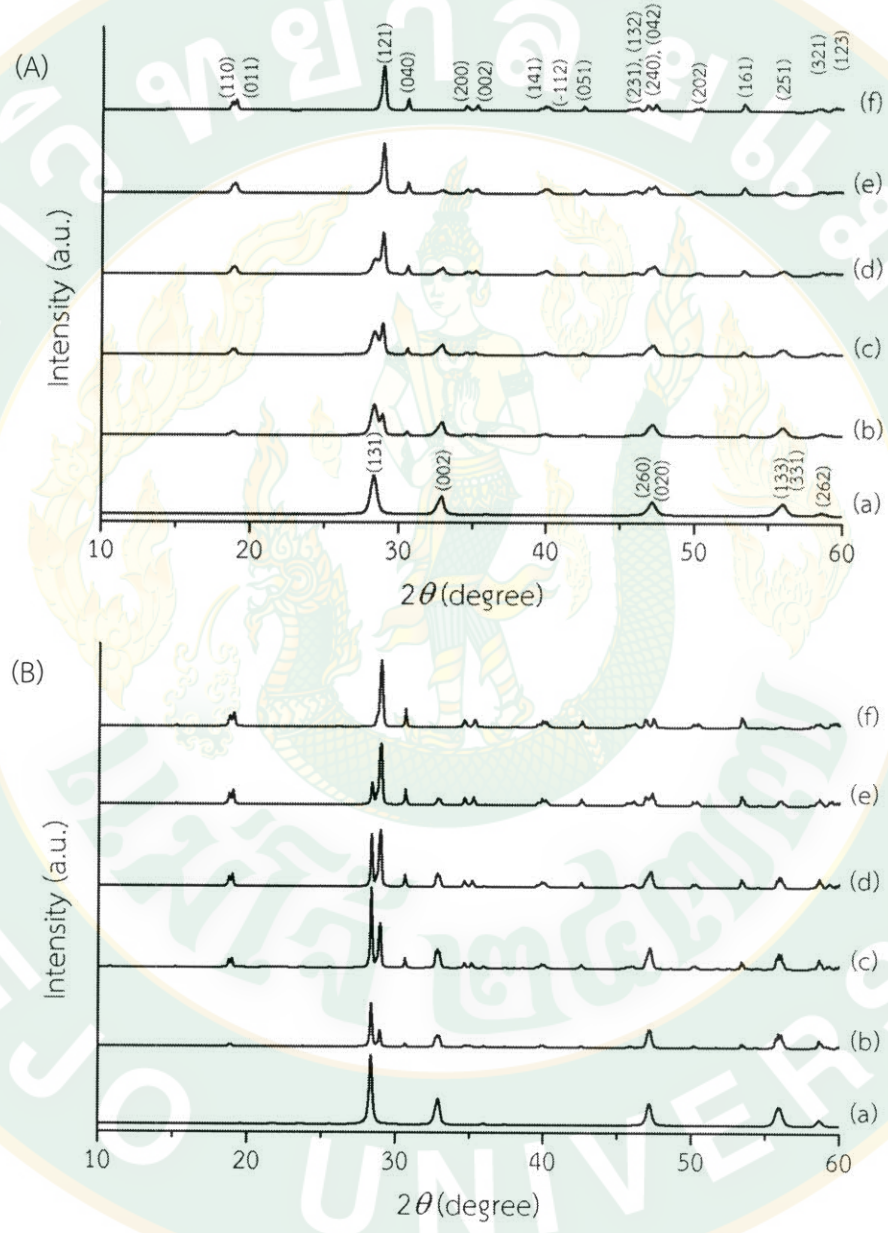

Figure 46 XRD patterns of (A) uncalcined and (B) calcined (a) Bi_2WO_6, (b)-(e) $BiVO_4/Bi_2WO_6$ composites with $f(V)$ = 0.50, 0.67, 0.80 and 0.91, respectively, and (f) $BiVO_4$.

Table 15 Physical properties and photocatalytic activities of uncalcined and calcined Bi_2WO_6, $BiVO_4$ and $BiVO_4/Bi_2WO_6$ composites under UV-visible and visible light

Samples	*f*(V)	Uncalcined							Calcined					
					UV-visible		visible					UV-visible		visible	
		D^a (nm)	E_g (eV)	SSA^b ($m^2 \cdot g^{-1}$)	Rate (μmol h^{-1})	R^2	Rate (μmol h^{-1})	R^2	D^a (nm)	E_g (eV)	SSA^b ($m^2 \cdot g^{-1}$)	Rate (μmol h^{-1})	R^2	Rate (μmol h^{-1})	R^2
Bi_2WO_6	0	16	2.65	19	1.91	0.9825	0.38	0.9440	29	2.65	4	2.71	0.9943	0.15	0.9523
$BiVO_4/Bi_2WO_6$	0.50	31	2.56	NA	8.64	0.9898	2.04	0.9734	47	2.49	NA	6.20	0.9908	1.84	0.9759
	0.67	26	2.56	NA	10.45	0.9952	5.08	0.9525	60	2.50	NA	7.79	0.9880	3.80	0.9847
	0.80	29	2.55	14	11.33	0.9932	4.82	0.9820	56	2.49	3	9.44	0.9909	4.10	0.9859
	0.91	36	2.54	NA	12.77	0.9929	6.73	0.9790	58	2.51	NA	8.64	0.9865	3.60	0.9940
$BiVO_4$	1	42	2.53	12	14.01	0.9932	7.90	0.9910	62	2.47	1	4.62	0.9912	1.90	0.9824

[a]Crystalline size of Bi_2WO_6 and $BiVO_4$ were calculated from (131) and (121) XRD peaks, respectively, by the Scherrer equation.

[b]Specific surface area

NA = Not analyzed

4.3 Morphology

Morphologies of synthesized $BiVO_4$ was small rod-like particles of ca. 100 nm in width and ca. 200 nm in length as shown in Fig. 47 (a). Additionally, the rod-like particles were agglomerated and densified by calcination at 600 °C for 4 h to produce large particles with grain boundaries (Fig. 47 (b)). Moreover, hydrothermally synthesized flake-ball-like (FB) Bi_2WO_6 in Fig. 47 (c) was confirmed by SEM images that all the Bi_2WO_6 particles were assemblies of flakes with their outer diameter of ca. 5 μm as has been reported previously (Hori *et al.*, 2015). The particle size of FB-Bi_2WO_6 particle was decreased by ca. 10–20% by calcination at 600 °C for 4 h (Fig. 47 (d)) presumably due to shrinkage and fusion of flakes.

On the other hand, calcined $BiVO_4/Bi_2WO_6$ composites showed different results. Figures 47 (e)-(h) show morphologies of $BiVO_4/Bi_2WO_6$ composites with $f(V)$ of 0.50, 0.67, 0.80 and 0.91, respectively, before calcination. As expectation based on the preparation process, it appeared that small $BiVO_4$ rods were partly deposited on and between flakes of FB-Bi_2WO_6 particles. It was also noteworthy that although $f(V)$ was increased, morphologies of the composites were similar while $BiVO_4/Bi_2WO_6$_0.80 particle was more covered by rod-like $BiVO_4$ particles than other composites. Furthermore, by calcination at 600 °C (Fig. 47 (i)-(l)), it was interesting that the deposited small $BiVO_4$ particles were interconnected with each other on the FB, but did not form large sintered particles (as was seen for c-$BiVO_4$). It was obviously that $BiVO_4$ particles were stabilized on FB-Bi_2WO_6 particles toward heat-induced sintering.

Elemental mapping analysis was shown in Fig. 48 in order to confirm that c-$BiVO_4/Bi_2WO_6$ composite was composted of Bi, O, V and W elements where the V atoms were partly distributed on the Bi_2WO_6 flake ball.

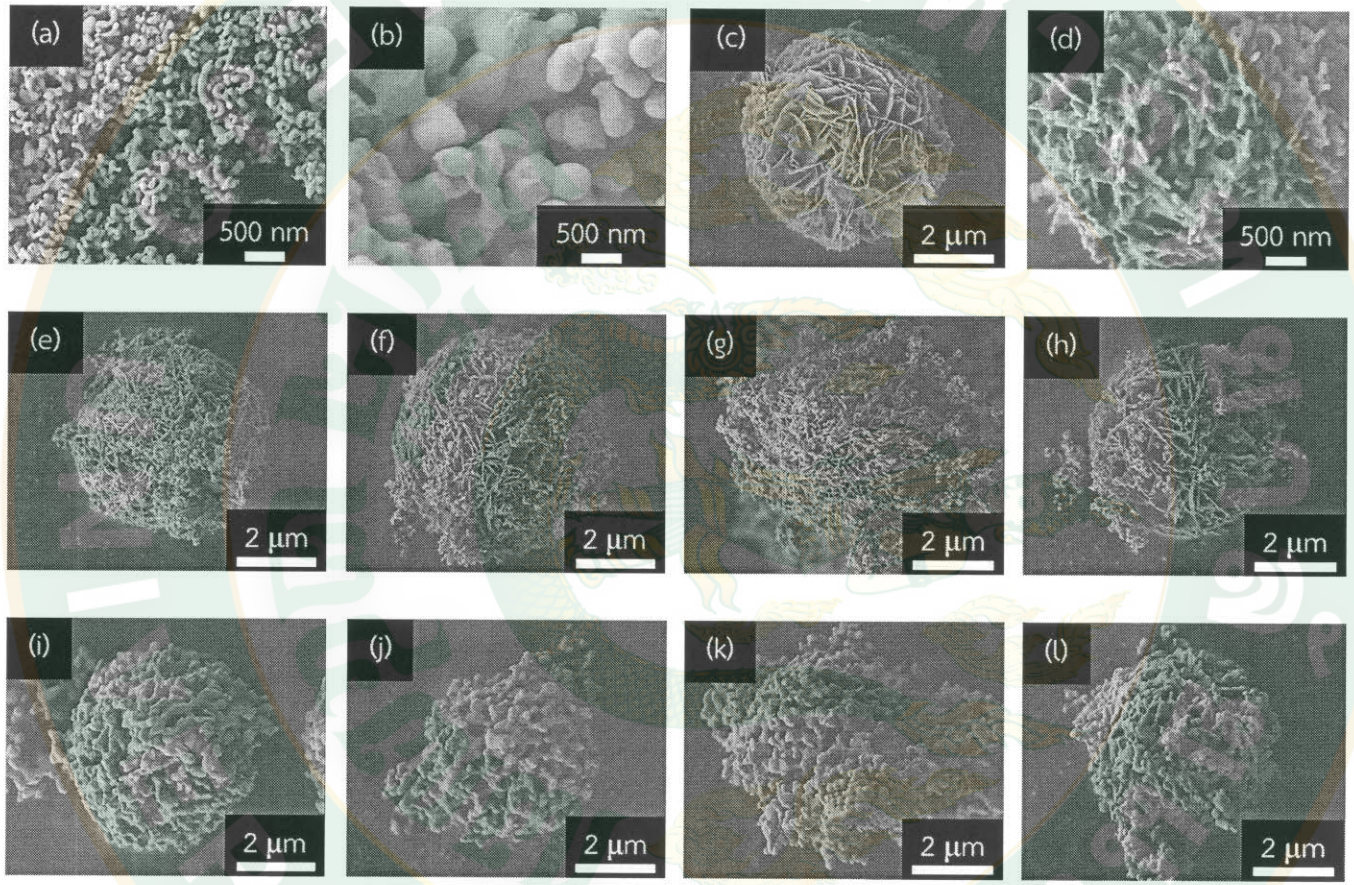

Figure 47 FE-SEM images of (a) $BiVO_4$, (b) c-$BiVO_4$, (c) Bi_2WO_6, (d) c-Bi_2WO_6, (e)–(h) $BiVO_4$/Bi_2WO_6 and (i)–(l) c-$BiVO_4$/Bi_2WO_6 with f(V) = 0.50, 0.67, 0.80 and 0.91, respectively.

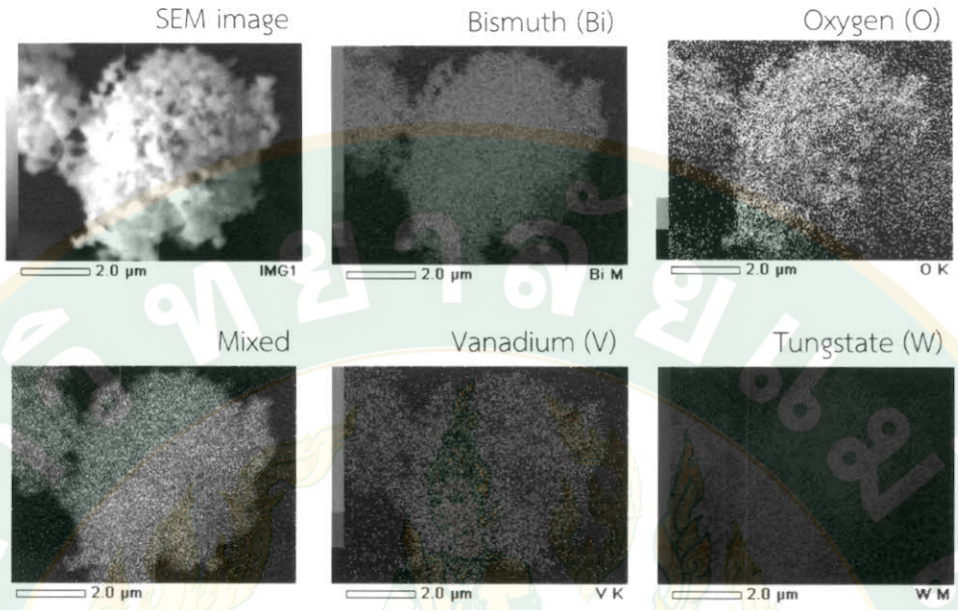

Figure 48 Elemental mapping of c-$BiVO_4$/Bi_2WO_6_0.8.

4.4 Surface area analysis

Specific surface area (SSA) of Bi_2WO_6, $BiVO_4$ and $BiVO_4$/Bi_2WO_6_0.8 composite were determined by nitrogen adsorption method. As showed in Table15, SSA of Bi_2WO_6, $BiVO_4$ and $BiVO_4$/Bi_2WO_6_0.8 composite were 19, 12 and 14 $m^2 \cdot g^{-1}$, respectively. However, SSA values were largely reduced by calcination. SSA of c-$BiVO_4$ was much decreased by ca. 92% from before calcination due to particle agglomeration while c-Bi_2WO_6 and c-$BiVO_4$/Bi_2WO_6_0.8 were ca. 78% reduction. This result related to FE-SEM images.

4.5 Electronic structure

Figure 49 shows KM spectra of uncalcined (Fig. 49 (A)) and calcined (Fig. 49 (B)) samples. It was found that all samples absorbed light in UV and visible region while $BiVO_4$ and $BiVO_4$/Bi_2WO_6 composites had wider light absorption in the visible region than Bi_2WO_6. As summarized in Table 15, E_g values of the $BiVO_4$ and Bi_2WO_6 were 2.53 and 2.65 eV, respectively. Moreover, E_g of composites were slightly wider (2.54–2.56 eV) than $BiVO_4$, but they were not significantly affected by varying *f*(V). From XRD results and E_g values, c-$BiVO_4$ and c-$BiVO_4$/Bi_2WO_6 should be promised to

be the most visible-light active photocatalysts due to narrow band gap energies (Ju *et al.*, 2014).

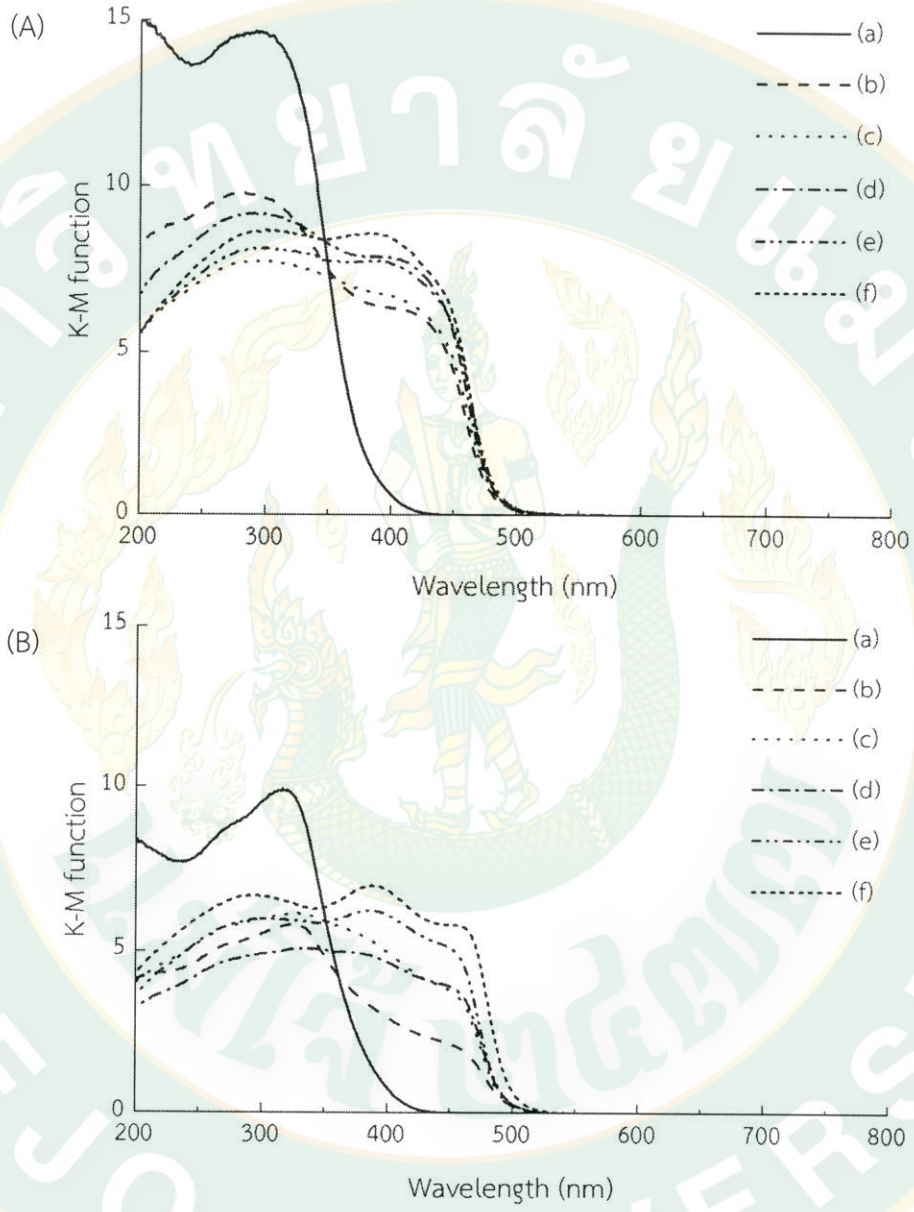

Figure 49 KM spectra of (A) uncalcined and (B) calcined (a) Bi_2WO_6, (b)-(e) $BiVO_4/Bi_2WO_6$ composites with f(V) = 0.50, 0.67, 0.80 and 0.91, respectively and (f) $BiVO_4$.

Figure 50 shows ERDT and CBB position of samples plotted as a function of energy (eV) from the top of valence band (VBT) of each sample. ERDT/CBB patterns represented surface properties of metal oxides (Nitta *et al.*, 2016). It could be seen that distribution of electrons were detected near CBB. In comparison, total ETs densities in < > of Bi_2WO_6 and $BiVO_4$ after calcination were significantly decreased. Moreover, it was found that ERDT pattern of $BiVO_4/Bi_2WO_6$ was reproducible by summations of the ERDT patterns of $BiVO_4$ and Bi_2WO_6 with ca. 0.4 eV negative (downward) shift of the Bi_2WO_6 pattern based on the assumption that ETs in $BiVO_4$ and Bi_2WO_6 gave ERDT patterns independently. Notably, degree of coincidence (ζ(a) = ERDT-pattern matching) = 0.589. This suggests that apparent VBT of Bi_2WO_6 is more anodic by ca. 0.4 eV than that of $BiVO_4$. As a result, apparent CBB of $BiVO_4$ and Bi_2WO_6 are almost the same position, being consistent with previous reports (Kang *et al.*, 2014). However, according to the fact that the ERDT patterns of $BiVO_4/Bi_2WO_6$ composite could be simulated only by summation of ERDT patterns of each component suggests negligible electron/positive hole transfer between two components (Ohtani *et al.*, 2010), which have been often presumed for the other composite photocatalysts (Jia *et al.*, 2014; Lin *et al.*, 2008).

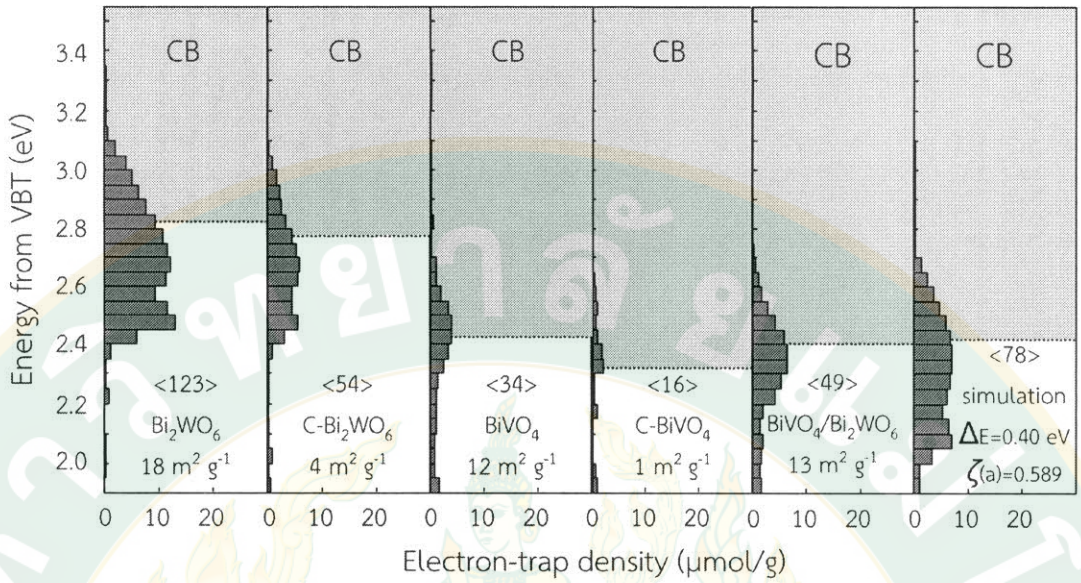

Figure 50 ERDT patterns of Bi_2WO_6, c-Bi_2WO_6, $BiVO_4$, c-$BiVO_4$, $BiVO_4/Bi_2WO_6$ and simulated $BiVO_4/Bi_2WO_6$. Numbers in < > denote the total density of ETs in the unit of μmol g^{-1}. The last row is specific surface area in the unit of $m^2 \cdot g^{-1}$.

5. Photocatalytic oxygen liberation over $BiVO_4/Bi_2WO_6$

5.1 Photocatalysis under UV light irradiation

Figure 51 shows photocatalytic activities of Bi_2WO_6, $BiVO_4$, $BiVO_4/Bi_2WO_6$ and their calcined samples in various f(V) under UV-visible and visible light irradiation, respectively. It was found that amount of oxygen liberation increased as light irradiation time and the UV-visible light with powerful photon energy accelerated photocatalysis to give higher amount of oxygen gas than the visible light.

At the beginning of photocatalysis under UV-visible light irradiation (Fig. 51), $BiVO_4$ and Bi_2WO_6 showed the highest and lowest-level photocatalytic activities, 14 and 2 μmol in 1.5 h, respectively. However, the activity of $BiVO_4$ was dropped down and became to be lower than that of $BiVO_4/Bi_2WO_6$_0.91 after irradiation for 1 h. It was obviously showed that the $BiVO_4/Bi_2WO_6$_0.91 composite exhibited the highest activity for prolonged reaction time to 1.5 h. On the other hand,

photocatalytic activity of c-$BiVO_4$ was lower than calcined composites and much decreased when compared to $BiVO_4$ (Fig. 51A). The highest activity among the calcined samples was observed for c-$BiVO_4$/Bi_2WO_6_0.91.

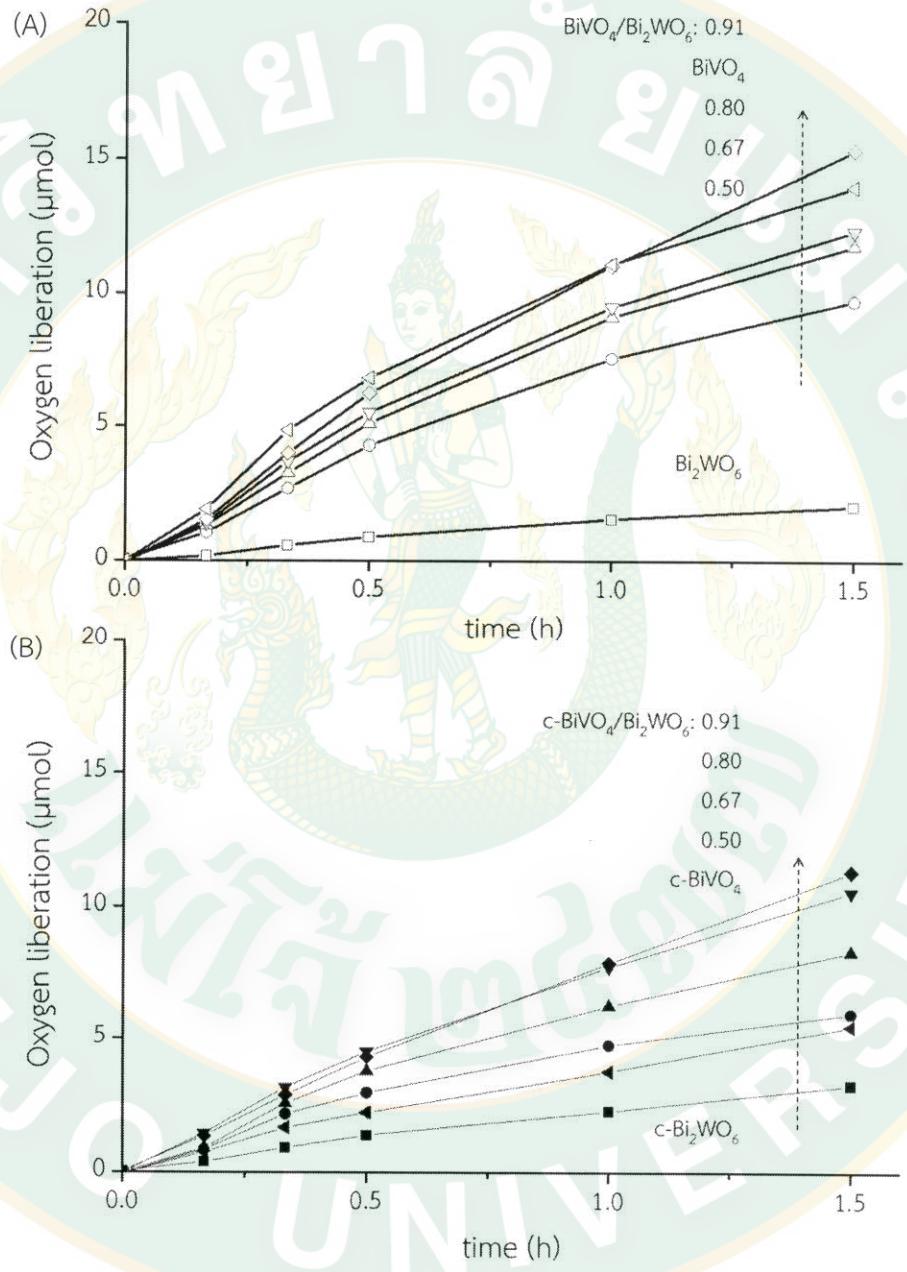

Figure 51 Photocatalytic oxygen liberations under UV-Vis light using (A) uncalcined and (B) calcined Bi_2WO_6, $BiVO_4$ and $BiVO_4$/Bi_2WO_6 composites.

5.2 Photocatalysis under visible light irradiation

Photocatalytic activity of present photocatalyst powders under visible light irradiation (Fig. 52) showed similar results to under UV-Vis irradiation.

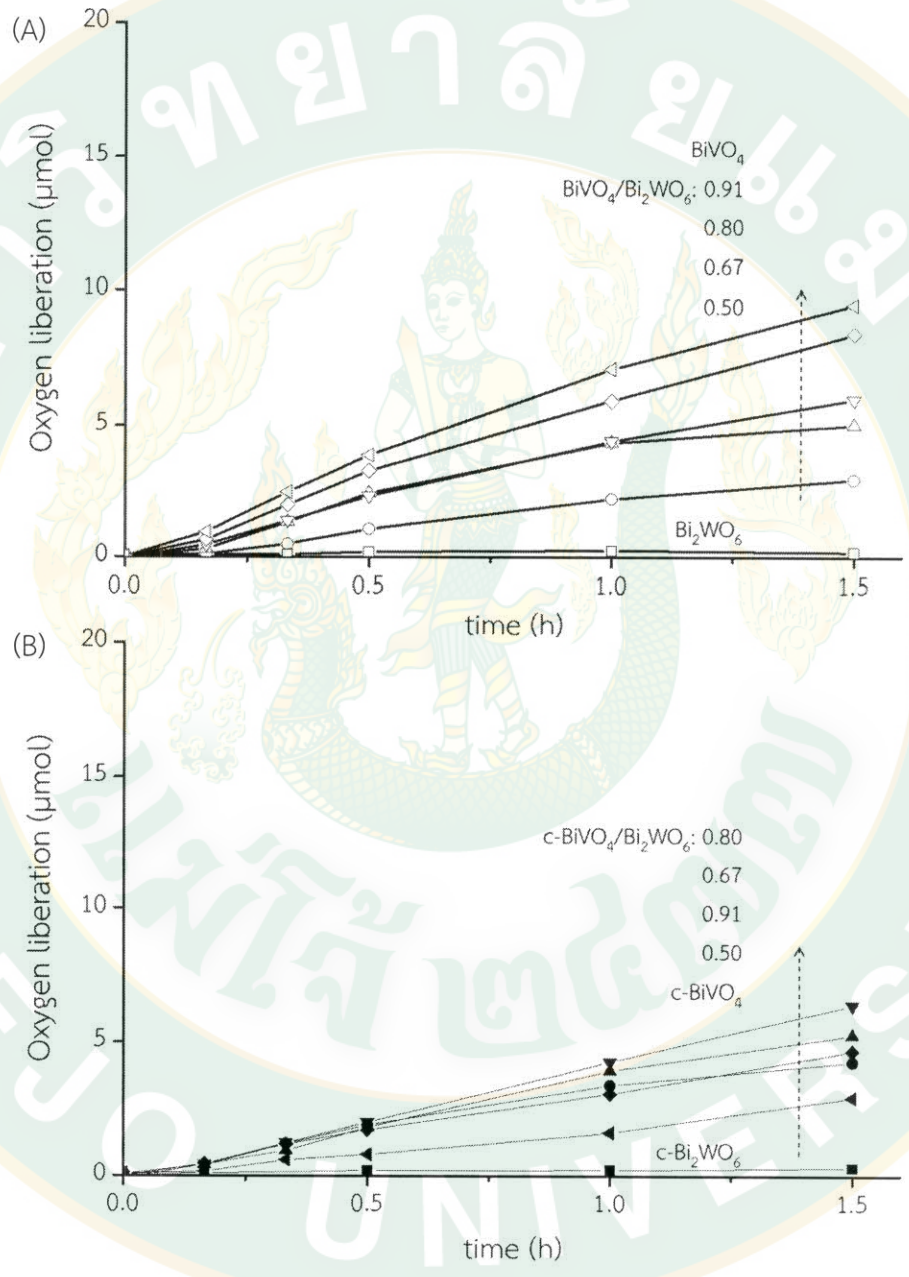

Figure 52 Photocatalytic oxygen liberations under visible light using (A) uncalcined and (B) calcined Bi_2WO_6, $BiVO_4$ and $BiVO_4/Bi_2WO_6$ composites.

In differently, $BiVO_4/Bi_2WO_6$_0.80 showed the highest activity among the calcined samples, while $BiVO_4$ showed the most active photocatalyst even after visible-light irradiation for 1.5 h.

Change of reaction rate after photocatalysis for 0.5 h as a function of $BiVO_4$ content in composites; *f*(V), was plotted as showed in Fig. 53. Photocatalytic activity was obviously increased with *f*(V) for the uncalcined samples under both UV-Vis and visible-light irradiations. On the other hand, the activities of calcined composites samples increased with *f*(V) to attain maximum at *f*(V) = 0.8 and then decreased to result in the relatively lower activity of c-$BiVO_4$. In other words, both UV-Vis and visible-light activities of uncalcined $BiVO_4$ was largely decreased to be ca. 30% by calcination (c-$BiVO_4$), while the activity of $BiVO_4/Bi_2WO_6$ composites, owing predominantly to vanadate component, was kept almost the same degree (or slightly decreased) even with calcination. Note that, the relatively lower activity of Bi_2WO_6 and almost linear increase with *f*(V).) It could say that tungsten components were negligibly active, but it helped to stabilize the activity of $BiVO_4$ when it was calcined.

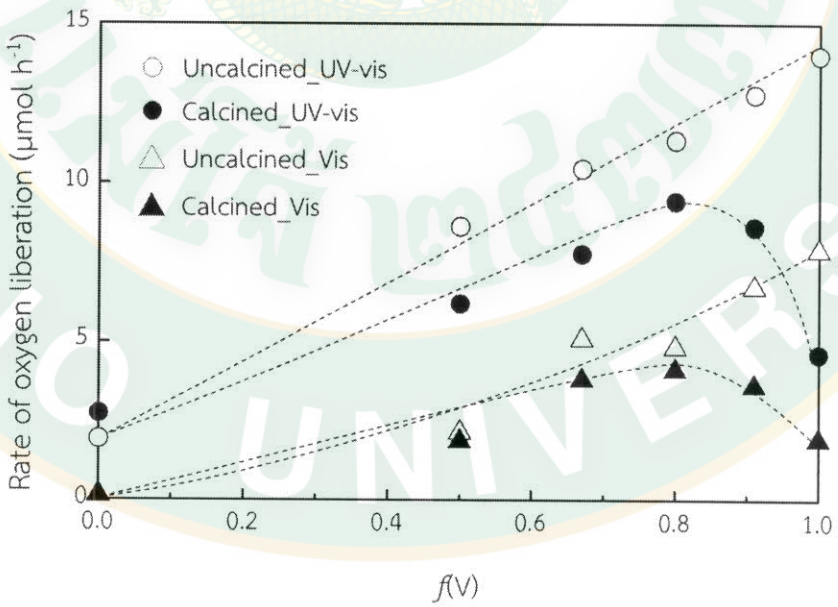

Figure 53 Change in photocatalytic activities of $BiVO_4/Bi_2WO_6$ and c-$BiVO_4/Bi_2WO_6$ composites as a function of *f*(V).

To understand electron-hole transfer and photocatalytic mechanism, CB and VB potentials of $BiVO_4$ and Bi_2WO_6 were calculated from an empirical equation and evaluated by E_g which determined by UV-Vis DRS (see appendix) (Chen *et al.*, 2016; Ju *et al.*, 2016). According to the equation, the calculated CB and VB potentials of $BiVO_4$ were 0.27 and 2.80 eV, respectively. Moreover, the calculated CB and VB potentials of Bi_2WO_6 were 0.37 and 3.02 eV, respectively. Therefore, on the basis of calculated energy bands and photocatalytic results, possible photocatalytic oxygen liberation mechanism of c-$BiVO_4$/Bi_2WO_6 powder was proposed as shown in Fig. 54. Two metal oxides were in contact by calcination. Under visible light irradiation, electrons were excited from VB to CB of $BiVO_4$. At the same time, positive holes were left in VB. This process was also happened in Bi_2WO_6. Electrons in CB of the $BiVO_4$ were transfer to CB of the Bi_2WO_6 while holes in VB of Bi_2WO_6 were migrated to VB of $BiVO_4$. Redox reactions were occurred at the surface. Notably; uncalcined $BiVO_4$/Bi_2WO_6 composites were proved for negligible electron-hole transfer between them.

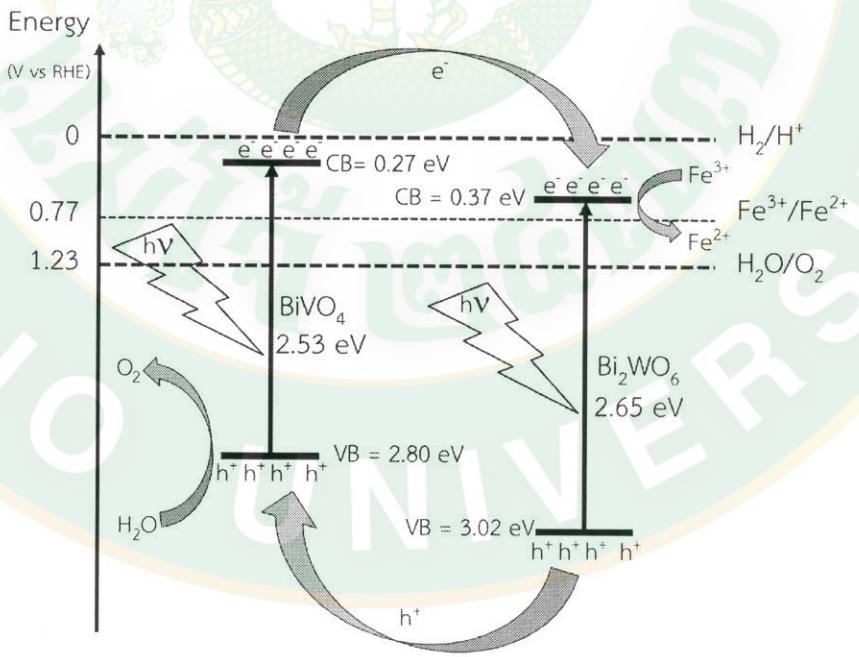

Figure 54 Schematic diagram of electron–hole pair separation and the possible photocatalytic mechanism over a c-$BiVO_4$/Bi_2WO_6 composite.

6. Stability of $BiVO_4/Bi_2WO_6$ composite

6.1 Sedimentation of $BiVO_4/Bi_2WO_6$ composite

Although $BiVO_4$ was the most active photocatalyst for oxygen liberation among the photocatalyst samples used in this study, c-$BiVO_4/Bi_2WO_6$ composite with a large overall particle size has potential for separating photocatalyst from reaction mixture after photoirradiation. Sedimentation test in Fig. 55 (A) showed dispersion of $BiVO_4$, c-$BiVO_4/Bi_2WO_6$_0.80 and titanium dioxide (TiO_2) powders in ultrapure water (pH = 7) after sonication for 15 min. Then, they were left in a room temperature. After 78 h (Fig. 55 (B)), the supernatant of a c-$BiVO_4/Bi_2WO_6$_0.80 suspension was the most clearly where the c-$BiVO_4/Bi_2WO_6$_0.80 precipitates were settled down at the bottom and some on the glass surface. On the other side, $BiVO_4$ powder and TiO_2 powder were stably dispersed in water even after standing for 78 h. This easy separated c-$BiVO_4/Bi_2WO_6$ photocatalyst is an advantage supporting practical applications in the future.

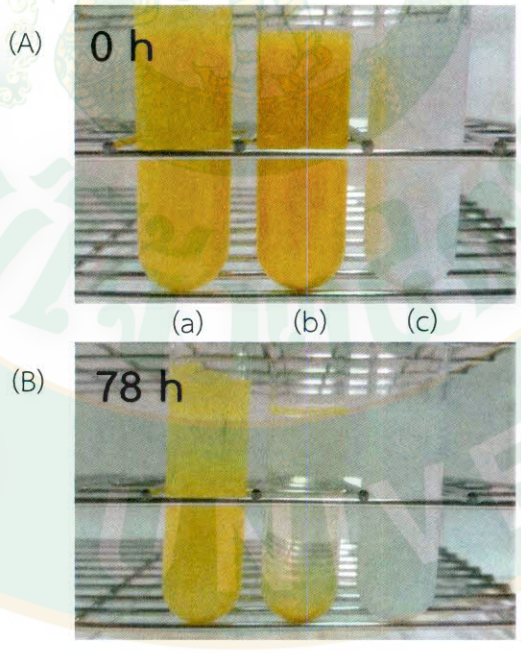

Figure 55 Sedimentation images of (a) $BiVO_4$, (b) c-$BiVO_4/Bi_2WO_6$_0.80 and (c) TiO_2 after (A) 0 h and (B) 78 h.

6.2 Reusability of $BiVO_4/Bi_2WO_6$ composite under visible light irradiation

Beside high photocatalytic activity and sedimentation property, long-life photocatalyst is also another important property for practical applications of a photocatalyst. Stability of $BiVO_4$, c-$BiVO_4$, $BiVO_4/Bi_2WO_6$_0.80 and c-$BiVO_4/Bi_2WO_6$_0.80 composite was tested by reusing them under the same environment (visible light irradiation). Photocatalytic oxygen liberations of 5 cycles were shown in Fig. 56. For each cycle, amount of oxygen at 0, 10, 20 and 30 min were determined by GC. $BiVO_4$ showed the highest photocatalytic activity in the initial cycles. However, rapid decreasing of photocatalytic activity was presented especially in the second cycle for all samples. After 5 cycles (2.5 h) irradiation, the activities of $BiVO_4$, c-$BiVO_4$, $BiVO_4/Bi_2WO_6$_0.80 and c-$BiVO_4/Bi_2WO_6$_0.80 were decreased to 16%, 24%, 25% and 45% of the first cycle, respectively. Thus, the c-$BiVO_4/Bi_2WO_6$ composite exhibited more stable in visible light irradiation than the others.

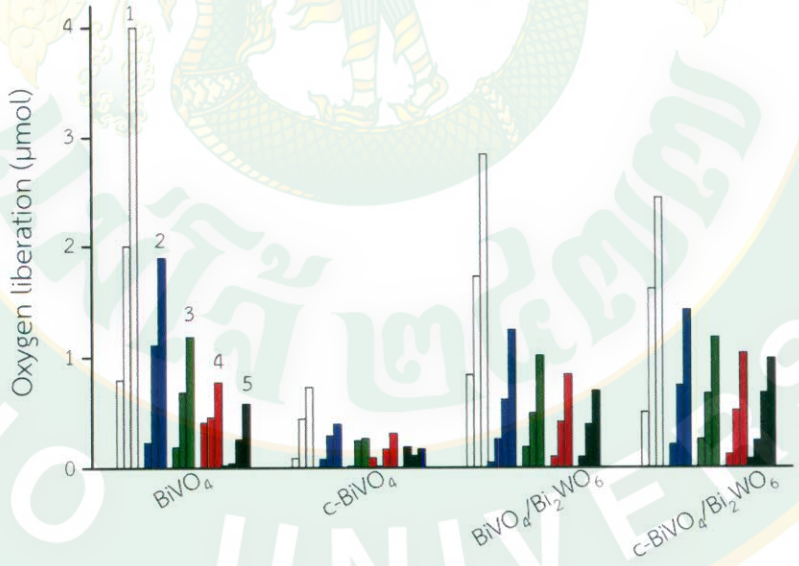

Figure 56 Reusability of uncalcined and calcined $BiVO_4$ and $BiVO_4/Bi_2WO_6$_0.8 composites in photocatalytic oxygen liberation under visible light. Numbers on top of the bar graph show cycles of photocatalysis.

6.3 Oxidation state and local structures of used photocatalysts

According to the sharply reduction of generated oxygen in the second cycles, used photocatalysts after the first cycle (15 min irradiation) were collected and analyzed. XANES spectra of fresh and used (U) were compared with vanadium oxide standards and showed in Fig. 57. It was illustrated that each spectrum had almost the same characteristic including pre-edge and absorption-edge position. In addition, the edges overlapped each other near V_2O_5 (V^{5+}) indicating that the oxidation states of vanadium in fresh and used $BiVO_4$ and $BiVO_4/Bi_2WO_6$_0.8 structures were +5. Moreover, EXAFS spectra in Fig. 58 showed V–O bond distances which were examined as the first shell distance from the vanadium atoms in terms of R-space. It was found that the V–O bond distances were almost the same for all fresh and used samples. As the results, it can be suggested that bulk structures of the used photocatalyst were not changed by photocatalysis under visible irradiation.

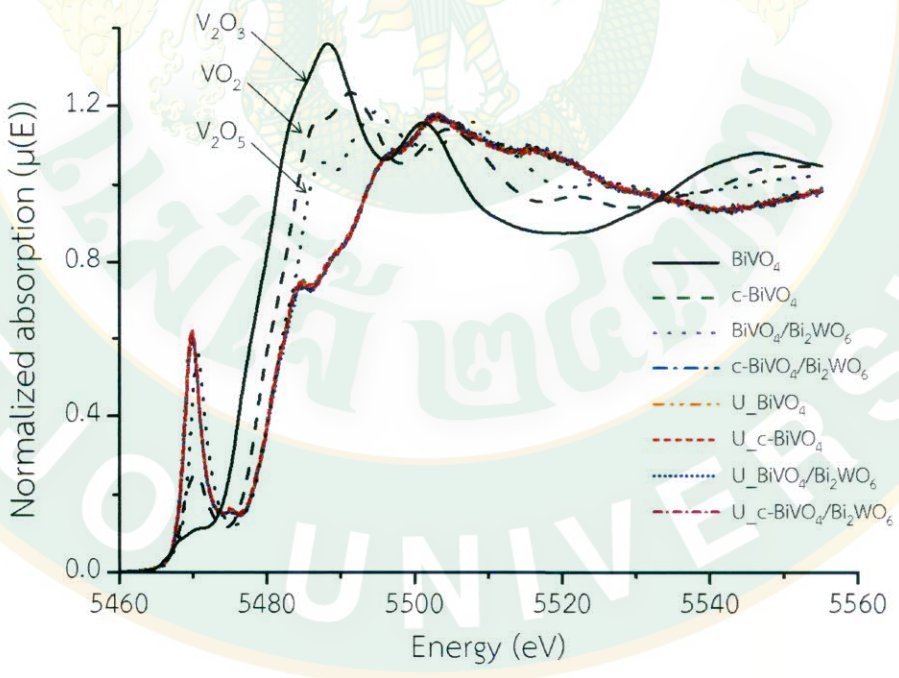

Figure 57 Normalization V K-edge XANES spectra of fresh and used $BiVO_4$, Bi_2WO_6 and $BiVO_4/Bi_2WO_6$_0.8 composite.

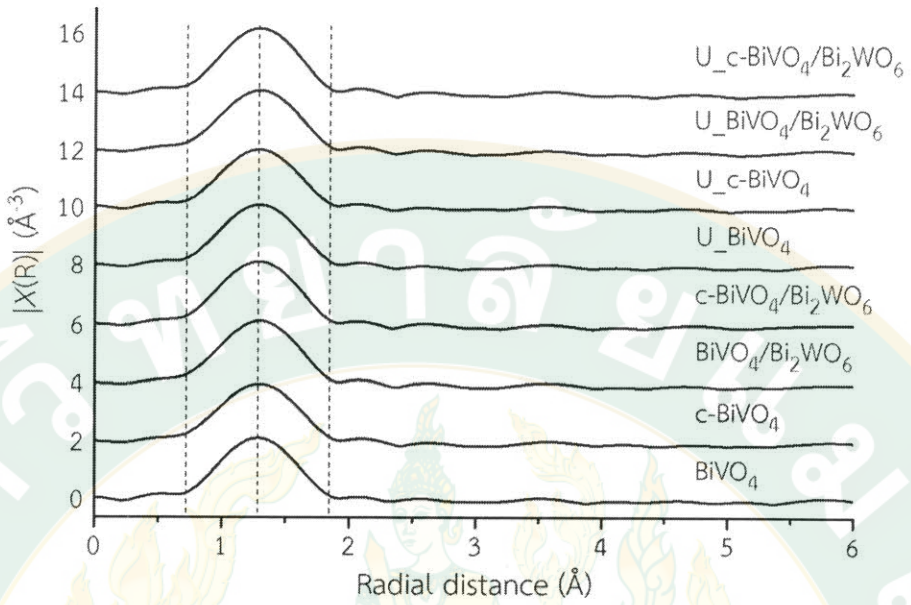

Figure 58 Normalized V K-edge EXAFS spectra of fresh and used $BiVO_4$ and $BiVO_4/Bi_2WO_6$_0.8 composite.

6.4 Morphology of used photocatalysts

Differentiation of particle surface and shape of photocatalysts samples after photoirradiation for 30 min were determined by FE-SEM and shown in Fig. 59. It was found that morphologies of $BiVO_4$, c-$BiVO_4$, $BiVO_4/Bi_2WO_6$_0.8 and c-$BiVO_4/Bi_2WO_6$_0.8 were almost unchanged as well as particle sizes were the same size as fresh particles suggesting that the declination of photocatalytic activities were not cause by photocorrosion.

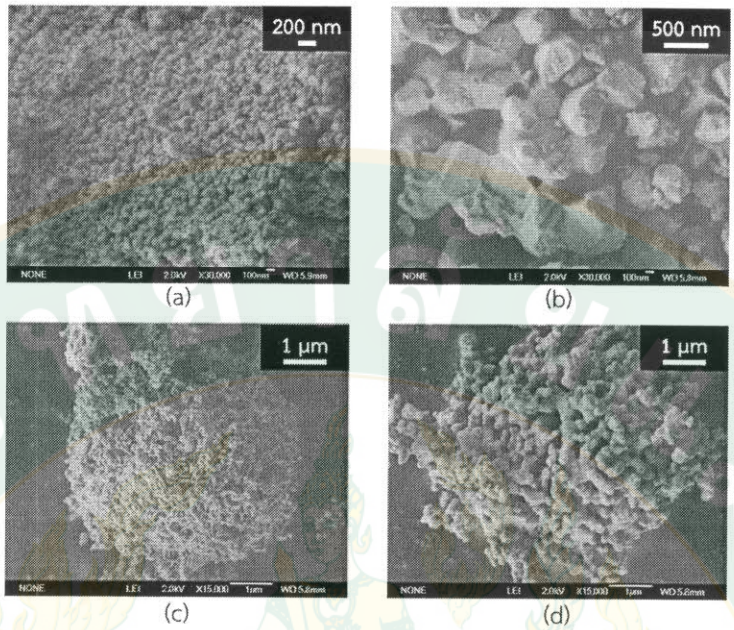

Figure 59 FE-SEM images of used (a) $BiVO_4$, (b) c-$BiVO_4$, (c) $BiVO_4/Bi_2WO_6$_0.8 and (d) c-$BiVO_4/Bi_2WO_6$_0.8 composites.

In fact, $BiVO_4$ is a stabilized semiconductor in wide range of electrolyte pH value (pH = 3 ~ 14) was accelerated by pH. Degradation of $BiVO_4$ in this research might be occurred due to low pH of iron(III) solution of 1.9. Additionally, surface of $BiVO_4$ tends to be damaged by V^{5+} ion leaching (Li *et al.*, 2013; Lichterman *et al.*, 2013; Park *et al.*, 2013; Sayama *et al.*, 2006). It was reported that ratio of V/Bi was significantly decreased during photoirradiation, resulting Bi-rich on the $BiVO_4$ surface and considerable reduction of photocurrent (Berglund *et al.*, 2011; Seabold and Choi, 2012). Thus, it was suggested that the reduction of photocatalytic activity of the studied samples might be due to a change of surface properties of the photocatalysts during photocatalysis.

CHAPTER 5

CONCLUSIONS

On the basis of previously mentioned results and discussion, it is concluded that ethanol is a key factor play role on $BiVO_4$ formation and enhances photocatalytic activity of a $BiVO_4$ semiconductor. The photocatalytic activity of obtained $BiVO_4$ powder depends on its crystalline structure; pure monoclinic phase is the most active photocatalyst over mixed phase. Moreover, pH value is another important parameter that influenced formation of $BiVO_4$ crystal as well as its morphology, particle size, specific surface area (SSA), band gap energy, electronic structure and local structure. In addition, reaction temperature and reaction time play role on morphology, particle size and SSA of the $BiVO_4$. It is also suggested that, XAS technique provided some useful data of local structure that a shorter V–O bond distance exhibits higher photocatalytic activity in case of photocatalytic oxygen liberation.

Furthermore, uncalcined $BiVO_4/Bi_2WO_6$ composites is proved that $BiVO_4$ and Bi_2WO_6 components exhibited photocatalytic activity independently without possible electron/positive hole transfer between them. The result of photocatalytic activity for oxygen liberation showed evident to support this finding since the linearly changing of photocatalytic activity with the composition for uncalcined $BiVO_4/Bi_2WO_6$ composites. Another support for the independency of two components is that ERDT of the uncalcined composite can be reproduced by summation of the ERDT patterns of each component by assuming VBT of Bi_2WO_6 is lower (more anodic) by ca. 0.4 eV than that of $BiVO_4$. If electron or positive-hole transfer happens between two components, the ERDT pattern of composites might not be a simple summation. On the other hand, calcined composites show maximum photocatalytic activity at 80% $BiVO_4$ fraction. This result is attributable to ability of Bi_2WO_6 to keep the $BiVO_4$ physical and chemical properties after calcination by retarding aggregation and fusion of $BiVO_4$ crystals into large and less active particles. In general, relatively higher photocatalytic activity of composite materials compared with those of single

components, often called "synergetic effect", has been defined to the interparticle electron/positive-hole transfers without showing the experimental evidence for the charge transfer. For the calcined $BiVO_4/Bi_2WO_6$ composite photocatalysts studied in this research, the maximum activity was observed due to stabilization of $BiVO_4$ particles by Bi_2WO_6 upon calcination rather than to possible charge transfer between the Bi_2WO_6 and $BiVO_4$. Thus, synergetic effects are not always owing to electronic effect, but, at least in the present case, to morphological effect or the others, and this must be important to design composite materials with high-level photocatalytic activity.

Long-term stability of a photocatalyst with strong reductive and oxidative properties and long life of photogenerated electron-hole pair still remain a challenge for future visible-light active photocatalyst. Reusability study for uncalcined and calcined pristine $BiVO_4$ and $BiVO_4/Bi_2WO_6$_0.8 composites shows stability of them for long-term photoirradiation.

BIBLIOGRAPHY

Barreca, D., Depero, L. E., Noto, V. D., Rizzi, G. A., Sangaletti, L. & Tondello, E. 1999. Thin films of bismuth vanadates with modifiable conduction properties. **Chemistry of Materials**, 11(2), 255–261.

Barthelmy, D. 2014. **The mineralogy database**. [Online]. Available http://www.webmineral.com/. (11 September 2017).

Berglund, S. P., Flaherty, D. W., Hahn, N. T., Bard, A. J. & Mullins, C. B. 2011. Photoelectrochemical oxidation of water using nanostructured $BiVO_4$ films. **The Journal of Physical Chemistry C**, 115(9), 3794–3802.

Bhattacharya, A. K., Mallick, K. K. & Hartridge, A. 1997. Phase transition in $BiVO_4$. **Materials Letters**, 30(1), 7–13.

Chaurand, P., Rose, J., Briois, V., Salome, M., Proux, O., Nassif, V., Olivi, L., Susini, J., Hazemann, J.-L. & Bottero, J.-Y. 2007. New methodological approach for the vanadium K-edge X-ray absorption near-edge structure interpretation: Application to the speciation of vanadium in oxide phases from steel slag. **The Journal of Physical Chemistry B**, 111(19), 5101–5110.

Chen, S., Takata, T. & Domen, K. 2017. Particulate photocatalysts for overall water splitting. **Nature Reviews Materials**, 2, 1–17.

Chen, L., Meng, D., Wu, X., Wang, A., Wang, J., Yu, M. & Liang, Y. 2016. Enhanced visible light photocatalytic performances of self-assembled hierarchically structured $BiVO_4/Bi_2WO_6$ heterojunction composites with different morphologies. **RSC Advances**, 6(57), 52300–52309.

Cooper, J. K., Gul, S., Toma, F. M., Chen, L., Glans, P.-A., Guo, J., Ager, J. W., Yano, J. & Sharp, I. D. 2014. Electronic structure of monoclinic $BiVO_4$. **Chemistry of Materials**, 26(18), 5365–5373.

Ding, K., Chen, B., Fang, Z. & Zhang, Y. 2013. Density functional theory study on the electronic and optical properties of three crystalline phases of $BiVO_4$. **Theoretical Chemistry Accounts**, 132(5), 1–7.

Dong, S., Feng, J., Li, Y., Hu, L., Liu, M., Wang, Y., Pi, Y., Sun, J. & Sun, J. 2014. Shape-controlled synthesis of $BiVO_4$ hierarchical structures with unique natural-sunlight-driven photocatalytic activity. **Applied Catalysis B: Environmental**, 152–153, 413–424.

Dong, S., Yu, C., Li, Y., Li, Y., Sun, J. & Geng, X. 2014. Controlled synthesis of T-shaped $BiVO_4$ and enhanced visible light responsive photocatalytic activity. **Journal of Solid State Chemistry**, 211, 176–183.

Dumrongrojthanath, P. 2015. **Synthesis and characterization of bismuth tungstate and molybdate nanostructures for photocatalysis.** Doctor of Philosophy (Chemistry). Chiang Mai University.

Fan, H., Jiang, T., Li, H., Wang, D., Wang, L., Zhai, J., He, D., Wang, P. & Xie, T. 2012. Effect of $BiVO_4$ crystalline phases on the photoinduced carriers behavior and photocatalytic activity. **The Journal of Physical Chemistry C**, 116(3), 2425–2430.

Fu, H., Pan, C., Yao, W. & Zhu, Y. 2005. Visible-light-induced degradation of rhodamine B by nanosized Bi_2WO_6. **The Journal of Physical Chemistry B**, 109(47), 22432–22439.

Fu, H., Zhang, L., Yao, W. & Zhu, Y. 2006. Photocatalytic properties of nanosized Bi_2WO_6 catalysts synthesized via a hydrothermal process. **Applied Catalysis B: Environmental**, 66(1), 100–110.

Fujishima, A., Rao, T. N. & Tryk, D. A. 2000. Titanium dioxide photocatalysis. **Journal of Photochemistry and Photobiology C: Photochemistry Reviews**, 1(1), 1–21.

Fumiaki, A., Kohei, N., Ryu, A. & Bunsho, O. 2007. Facile hydrothermal preparation and photocatalytic activity of bismuth tungstate polycrystalline flake-ball particles. **Chemistry Letters**, 36(11), 1314–1315.

Gotić, M., Musić, S., Ivanda, M., Šoufek, M. & Popović, S. 2005. Synthesis and characterisation of bismuth (III) vanadate. **Journal of Molecular Structure**, 744, 535–540.

Guo, Y., Yang, X., Ma, F., Li, K., Xu, L., Yuan, X. & Guo, Y. 2010. Additive-free controllable fabrication of bismuth vanadates and their photocatalytic activity toward dye degradation. **Applied Surface Science**, 256(7), 2215–2222.

He, R., Cao, S., Zhou, P. & Yu, J. 2014. Recent advances in visible light Bi-based photocatalysts. **Chinese Journal of Catalysis**, 35(7), 989–1007.

Hori, H., Takase, M., Amano, F. & Ohtani, B. 2015. Mechanism of the formation of hierarchical-structured bismuth tungstate photocatalyst particles through counter-flow supply of bismuth and tungsten sources. **Chemistry Letters**, 44(12), 1723–1725.

Hori, H., Takase, M., Takashima, M., Amano, F., Shibayama, T. & Ohtani, B. 2017. Mechanism of formation, structural characteristics and photocatalytic activities of hierarchical-structured bismuth-tungstate particles. **Catalysis Today**. (In press, Corrected Proof)

Jackson, S. D. & Hargreaves, J. S. J. 2009. **Metal Oxide Catalysis**. Germany: Wiley.

Jia, Q., Iwase, A. & Kudo, A. 2014. $BiVO_4$-Ru/$SrTiO_3$:Rh composite Z-scheme photocatalyst for solar water splitting. **Chemical Science**, 5(4), 1513–1519.

Jiang, H., Dai, H., Meng, X., Zhang, L., Deng, J. & Ji, K. 2011. Morphology-dependent photocatalytic performance of monoclinic $BiVO_4$ for methyl orange degradation under visible-light irradiation. **Chinese Journal of Catalysis**, 32(6–8), 939–949.

Ju, P., Wang, P., Li, B., Fan, H., Ai, S., Zhang, D. & Wang, Y. 2014. A novel calcined Bi_2WO_6/$BiVO_4$ heterojunction photocatalyst with highly enhanced photocatalytic activity. **Chemical Engineering Journal**, 236, 430–437.

Ju, P., Wang, Y., Sun, Y. & Zhang, D. 2016. Controllable one-pot synthesis of a nest-like Bi_2WO_6/$BiVO_4$ composite with enhanced photocatalytic antifouling performance under visible light irradiation. **Dalton Transactions**, 45(11), 4588–4602.

Kang, D., Park, Y., Hill, J. C. & Choi, K.-S. 2014. Preparation of Bi-based ternary oxide photoanodes $BiVO_4$, Bi_2WO_6, and $Bi_2Mo_3O_{12}$ using dendritic Bi metal electrodes. **The Journal of Physical Chemistry Letters**, 5(17), 2994–2999.

Ke, D., Peng, T., Ma, L., Cai, P. & Dai, K. 2009. Effects of hydrothermal temperature on the microstructures of $BiVO_4$ and its photocatalytic O_2 evolution activity under visible light. **Inorganic Chemistry**, 48(11), 4685–4691.

Kim, J. H. & Lee, J. S. 2014. $BiVO_4$-based heterostructured photocatalysts for solar water splitting: A review. **Energy and Environment Focus**, 3(4), 339–353.

Kudo, A. & Hijii, S. 1999. H_2 or O_2 evolution from aqueous solutions on layered oxide photocatalysts consisting of Bi^{3+} with $6s^2$ configuration and d^0 transition metal ions. **Chemistry Letters**, 28(10), 1103–1104.

Kudo, A., Omori, K. & Kato, H. 1999. A novel aqueous process for preparation of crystal form-controlled and highly crystalline $BiVO_4$ powder from layered vanadates at room temperature and its photocatalytic and photophysical properties. **Journal of the American Chemical Society**, 121(49), 11459–11467.

Lai, H. F., Chen, C. C., Chang, Y. K., Lu, C. S. & Wu, R. J. 2014. Efficient photocatalytic degradation of thiobencarb over $BiVO_4$ driven by visible light: Parameter and reaction pathway investigations. **Separation and Purification Technology**, 122, 78–86.

Laorodphan, N., Pooddee, P., Kidkhunthod, P., Kunthadee, P., Tapala, W. & Puntharod, R. 2016. Boron and pentavalent vanadium local environments in binary vanadium borate glasses. **Journal of Non-Crystalline Solids**, 453(Supplement C), 118–124.

Lei, B. X., Zeng, L. L., Zhang, P., Sun, Z. F., Sun, W. & Zhang, X. X. 2014. Hydrothermal synthesis and photocatalytic properties of visible-light induced $BiVO_4$ with different morphologies. **Advanced Powder Technology**, 25(3), 946–951.

Li, J. & Wu, N. 2015. Semiconductor-based photocatalysts and photoelectrochemical cells for solar fuel generation: A review. **Catalysis Science & Technology**, 5(3), 1360–1384.

Li, Z., Luo, W., Zhang, M., Feng, J. & Zou, Z. 2013. Photoelectrochemical cells for solar hydrogen production: Current state of promising photoelectrodes, methods to improve their properties, and outlook. **Energy & Environmental Science**, 6(2), 347–370.

Lichterman, M. F., Shaner, M. R., Handler, S. G., Brunschwig, B. S., Gray, H. B., Lewis, N. S. & Spurgeon, J. M. 2013. Enhanced stability and activity for water oxidation in alkaline media with bismuth vanadate photoelectrodes modified with a cobalt oxide catalytic layer produced by atomic layer deposition. **The Journal of Physical Chemistry Letters**, 4(23), 4188–4191.

Lin, X., Huang, F., Xing, J., Wang, W. & Xu, F. 2008. Heterojunction semiconductor $SnO_2/SrNb_2O_6$ with an enhanced photocatalytic activity: The significance of chemically bonded interface. **Acta Materialia**, 56(12), 2699–2705.

Lin, X., Yu, L., Yan, L., Li, H., Yan, Y., Liu, C. & Zhai, H. 2014. Visible light photocatalytic activity of $BiVO_4$ particles with different morphologies. **Solid State Sciences**, 32, 61–66.

Lu, R., Lili, M., Lei, J., Jian-Bo, W., Mingqiang, Q. & Ying, Y. 2009. Template-free synthesis of $BiVO_4$ nanostructures: II. Relationship between various microstructures for monoclinic $BiVO_4$ and their photocatalytic activity for the degradation of rhodamine B under visible light. **Nanotechnology**, 20(40), 405602.

Lu, Y., Shang, H., Shi, F., Chao, C., Zhang, X. & Zhang, B. 2015. Preparation and efficient visible light-induced photocatalytic activity of m-$BiVO_4$ with different morphologies. **Journal of Physics and Chemistry of Solids**, 85(Supplement C), 44–50.

Ma, L., Li, W. H. & Luo, J. H. 2013. Solvothermal synthesis and characterization of well-dispersed monoclinic olive-like $BiVO_4$ aggregates. **Materials Letters**, 102, 65–67.

Marta Castellote, N. B. (2011). Principles of TiO_2 Photocatalysis. In Y. Ohama and D. V. Gemert (Eds.), **Application of Titanium Dioxide Photocatalysis to Construction Materials** (1 ed.). Netherlands: Springer.

Martínez-de la Cruz, A. & Perez, U. 2010. Photocatalytic properties of $BiVO_4$ prepared by the co-precipitation method: Degradation of rhodamine B and possible reaction mechanisms under visible irradiation. **Materials Research Bulletin**, 45(2), 135–141.

Misawa, H. 2017. **Solar cells utilizing the invisible light in the infrared region**. [Online]. Available http://www.cris.hokudai.ac.jp/cris/en/research/frontier/misawa.html. (11 September 2017).

Nitta, A., Takase, M., Takashima, M., Murakami, N. & Ohtani, B. 2016. A fingerprint of metal-oxide powders: Energy-resolved distribution of electron traps. **Chemical Communications**, 52(81), 12096–12099.

Ohtani, B. 2008. Preparing articles on photocatalysis—beyond the illusions, misconceptions, and speculation. **Chemistry Letters**, 37(3), 216–229.

Ohtani, B. 2016. Hidden but possibly fatal misconceptions in photocatalysis studies: a short critical review. **Catalysts**, 6(12), 192.

Ohtani, B., Prieto-Mahaney, O. O., Li, D. & Abe, R. 2010. What is Degussa (Evonik) P25? Crystalline composition analysis, reconstruction from isolated pure particles and photocatalytic activity test. **Journal of Photochemistry and Photobiology A: Chemistry**, 216(2), 179–182.

Opimakh, O. V., Kurilo, I. I. & Zharskii, I. M. 2014. A mechanism of bismuth orthovanadate structure formation during solvothermal synthesis. **Inorganic Materials**, 50(4), 415–418.

Park, Y., McDonald, K. J. & Choi, K. S. 2013. Progress in bismuth vanadate photoanodes for use in solar water oxidation. **Chemical Society Review**, 42(6), 2321–2337.

Ravidhas, C., Juliat Josephine, A., Sudhagar, P., Devadoss, A., Terashima, C., Nakata, K., Fujishima, A., Moses Ezhil Raj, A. & Sanjeeviraja, C. 2015. Facile synthesis of nanostructured monoclinic bismuth vanadate by a co-precipitation method: Structural, optical and photocatalytic properties. **Materials Science in Semiconductor Processing**, 30, 343–351.

Saison, T., Chemin, N., Chanéac, C., Durupthy, O., Ruaux, V., Mariey, L., Maugé, F., Beaunier, P. & Jolivet, J.-P. 2011. Bi_2O_3, $BiVO_4$, and Bi_2WO_6: Impact of surface properties on photocatalytic activity under visible light. **The Journal of Physical Chemistry C**, 115(13), 5657–5666.

Sayama, K., Nomura, A., Arai, T., Sugita, T., Abe, R., Yanagida, M., Oi, T., Iwasaki, Y., Abe, Y. & Sugihara, H. 2006. Photoelectrochemical decomposition of water into H_2 and O_2 on porous $BiVO_4$ thin-film electrodes under visible light and significant effect of Ag ion treatment. **The Journal of Physical Chemistry B**, 110(23), 11352–11360.

Seabold, J. A. & Choi, K.-S. 2012. Efficient and stable photo-oxidation of water by a bismuth vanadate photoanode coupled with an iron oxyhydroxide oxygen evolution catalyst. **Journal of the American Chemical Society**, 134(4), 2186–2192.

Soma, K., Iwase, A. & Kudo, A. 2014. Enhanced activity of $BiVO_4$ powdered photocatalyst under visible light irradiation by preparing microwave-assisted aqueous solution methods. **Catalysis Letters**, 144(11), 1962–1967.

Sun, S. & Wang, W. 2014. Advanced chemical compositions and nanoarchitectures of bismuth based complex oxides for solar photocatalytic application. **RSC Advances**, 4(88), 47136–47152.

Sun, S., Wang, W., Li, D., Zhang, L. & Jiang, D. 2014. Solar light driven pure water splitting on quantum sized $BiVO_4$ without any cocatalyst. **ACS Catalysis**, 4(10), 3498–3503.

Tamirat, A. G., Rick, J., Dubale, A. A., Su, W.-N. & Hwang, B.-J. 2016. Using hematite for photoelectrochemical water splitting: A review of current progress and challenges. **Nanoscale Horizons**, 1(4), 243–267.

Tan, G., Zhang, L., Ren, H., Wei, S., Huang, J. & Xia, A. 2013. Effects of pH on the hierarchical structures and photocatalytic performance of $BiVO_4$ powders prepared via the microwave hydrothermal method. **ACS Applied Materials & Interfaces**, 5(11), 5186–5193.

Thalluri, S. M., Martinez Suarez, C., Hussain, M., Hernandez, S., Virga, A., Saracco, G. & Russo, N. 2013. Evaluation of the parameters affecting the visible-light-induced photocatalytic activity of monoclinic $BiVO_4$ for water oxidation. **Industrial & Engineering Chemistry Research**, 52(49), 17414–17418.

Tokunaga, S., Kato, H. & Kudo, A. 2001. Selective preparation of monoclinic and tetragonal $BiVO_4$ with scheelite structure and their photocatalytic properties. **Chemistry of Materials**, 13(12), 4624–4628.

Venkatesan, R., Velumani, S. & Kassiba, A. 2012. Mechanochemical synthesis of nanostructured $BiVO_4$ and investigations of related features. **Materials Chemistry and Physics**, 135(2), 842–848.

Wan, Y., Wang, S., Luo, W. & Zhao, L. 2012. Impact of preparative pH on the morphology and photocatalytic activity of $BiVO_4$. **International Journal of Photoenergy**, 2012, 1–7.

Wood, P. & Glasser, F. P. 2004. Preparation and properties of pigmentary grade $BiVO_4$ precipitated from aqueous solution. **Ceramics International**, 30(6), 875–882.

Yan, X., Ohno, T., Nishijima, K., Abe, R. & Ohtani, B. 2006. Is methylene blue an appropriate substrate for a photocatalytic activity test? A study with visible-light responsive titania. **Chemical Physics Letters**, 429(4), 606–610.

Yang, J., Wang, D., Zhou, X. & Li, C. 2013. A theoretical study on the mechanism of photocatalytic oxygen evolution on $BiVO_4$ in aqueous solution. **Chemistry-A European Journal**, 19(4), 1320–1326.

Yu, J., Zhang, Y. & Kudo, A. 2009. Synthesis and photocatalytic performances of $BiVO_4$ by ammonia co-precipitation process. **Journal of Solid State Chemistry**, 182(2), 223–228.

Zhai, Z., Getsoian, A. B. & Bell, A. T. 2013. The kinetics of selective oxidation of propene on bismuth vanadium molybdenum oxide catalysts. **Journal of Catalysis**, 308(Supplement C), 25–36.

Zhang, A. & Zhang, J. 2009a. Characterization of visible-light-driven $BiVO_4$ photocatalysts synthesized via a surfactant-assisted hydrothermal method. **Spectrochimica Acta Part A: Molecular and Biomolecular Spectroscopy**, 73(2), 336–341.

Zhang, A. & Zhang, J. 2009b. Hydrothermal processing for obtaining of $BiVO_4$ nanoparticles. **Materials Letters**, 63(22), 1939–1942.

Zhang, A., Zhang, J., Cui, N., Tie, X., An, Y. & Li, L. 2009. Effects of pH on hydrothermal synthesis and characterization of visible-light-driven $BiVO_4$ photocatalyst. **Journal of Molecular Catalysis A: Chemical**, 304(1–2), 28–32.

Zhang, L., Chen, D. & Jiao, X. 2006. Monoclinic structured $BiVO_4$ nanosheets: Hydrothermal preparation, formation mechanism, and coloristic and photocatalytic properties. **The Journal of Physical Chemistry B**, 110(6), 2668–2673.

Zhang, L., Long, J., Pan, W., Zhou, S., Zhu, J., Zhao, Y., Wang, X. & Cao, G. 2012. Efficient removal of methylene blue over composite-phase $BiVO_4$ fabricated by hydrothermal control synthesis. **Materials Chemistry and Physics**, 136(2), 897–902.

Zhang, X., Ai, Z., Jia, F., Zhang, L., Fan, X. & Zou, Z. 2007. Selective synthesis and visible-light photocatalytic activities of $BiVO_4$ with different crystalline phases. **Materials Chemistry and Physics**, 103(1), 162–167.

Zhang, Z., Wang, W., Shang, M. & Yin, W. 2010. Photocatalytic degradation of rhodamine B and phenol by solution combustion synthesized $BiVO_4$ photocatalyst. **catalysis communications**, 11(11), 982–986.

Zhou, L., Wang, W., Liu, S., Zhang, L., Xu, H. & Zhu, W. 2006. A sonochemical route to visible-light-driven high-activity $BiVO_4$ photocatalyst. **Journal of Molecular Catalysis A: Chemical**, 252(1), 120–124.

APPENDIX

CHARACTERIZATIONS

The Joint Committee on Powder Diffraction Standards (JCPDS)

Name and formula

Reference code:	00-014-0133
Mineral name:	Dreyerite, syn
PDF index name:	Bismuth Vanadium Oxide
Empirical formula:	BiO_4V
Chemical formula:	$BiVO_4$

Crystallographic parameters

Crystal system:	Tetragonal
Space group:	I41/amd
Space group number:	141
a (Å):	7.2999
b (Å):	7.2999
c (Å):	6.4573
Alpha (°):	90.0000
Beta (°):	90.0000
Gamma (°):	90.0000
Calculated density (g cm^{-3}):	6.25
Volume of cell (10^6 pm^3):	344.10
Z:	4.00

Subfiles and Quality

Subfiles:	Inorganic
	Mineral
	Common Phase
	NBS pattern
Quality:	Star (S)

Comments

Color:	Orange-yellow
General comments:	Changes to stable monoclinic form on heating to 400-500 °C.
Sample source:	Sample was obtained from City Chemical Corp., New York, USA.
Sample preparation:	Sample was also precipitated at NBS, Gaithersburg, Maryland, USA, from solutions of Na_3VO_4 and $Bi(NO_3)_3$.
Analysis:	Spectrographic analysis: 0.0001-0.01% each of Al and Si.
Temperature:	Pattern taken at 26 °C.

References

Primary reference: *Natl. Bur. Stand. (U.S.) Monogr. 25*, **3**, 14, (1964)

Stick Pattern

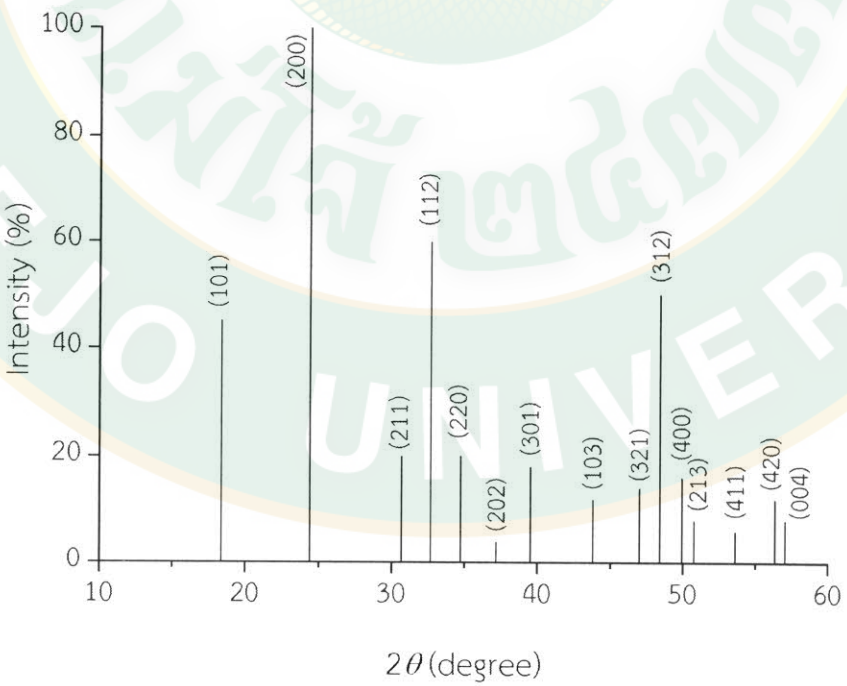

Peak list of bismuth vanadium oxide

No.	h	k	l	d [Å]	2θ	Intensity [%]
1	1	0	1	4.83900	18.319	45.0
2	2	0	0	3.64900	24.374	100.0
3	2	1	1	2.91200	30.678	20.0
4	1	1	2	2.73800	32.680	60.0
5	2	2	0	2.58200	34.715	20.0
6	2	0	2	2.41900	37.137	4.0
7	3	0	1	2.27800	39.528	18.0
8	1	0	3	2.06500	43.805	12.0
9	3	2	1	1.93200	46.995	14.0
10	3	1	2	1.87900	48.404	50.0
11	4	0	0	1.82500	49.932	16.0
12	2	1	3	1.79700	50.765	8.0
13	4	1	1	1.70800	53.615	6.0
14	4	2	0	1.63200	56.328	12.0
15	0	0	4	1.61400	57.013	8.0
16	3	3	2	1.51830	60.974	10.0

Name and formula

Reference code:	00-014-0688
Mineral name:	Clinobisvanite, syn
PDF index name:	Bismuth Vanadium Oxide
Empirical formula:	BiO_4V
Chemical formula:	$BiVO_4$

Crystallographic parameters

Crystal system:	Monoclinic
Space group:	I2/a
Space group number:	15
a (Å):	5.1950
b (Å):	11.7010
c (Å):	5.0920
Alpha (°):	90.0000
Beta (°):	90.3800
Gamma (°):	90.0000
Calculated density (g cm^{-3}):	6.95
Volume of cell (10^6 pm^3):	309.52
Z:	4.00

Subfiles and Quality

Subfiles:	Inorganic
	Mineral
	Common Phase
	NBS pattern
Quality:	Indexed (I)

Comments

Color:	Orange-yellow
Sample preparation:	Sample was prepared at NBS, Gaithersburg, Maryland, USA, by heating stoichiometric mixtures of bismuth oxide and vanadium oxide at 895 C for 16 hours.
Analysis:	Spectrographic analysis: 0.001 to 0.01% each of Al and Si.
Additional pattern:	See ICSD 100602, 100603, 100604 and 100605 (PDF 83-1697, 83-1698, 83-1699 and 83-1700).
Temperature:	Pattern taken at 26 °C.

References

Primary reference: *Natl. Bur. Stand. (U.S.) Monogr. 25*, **3**, 14, (1964)

Stick Pattern

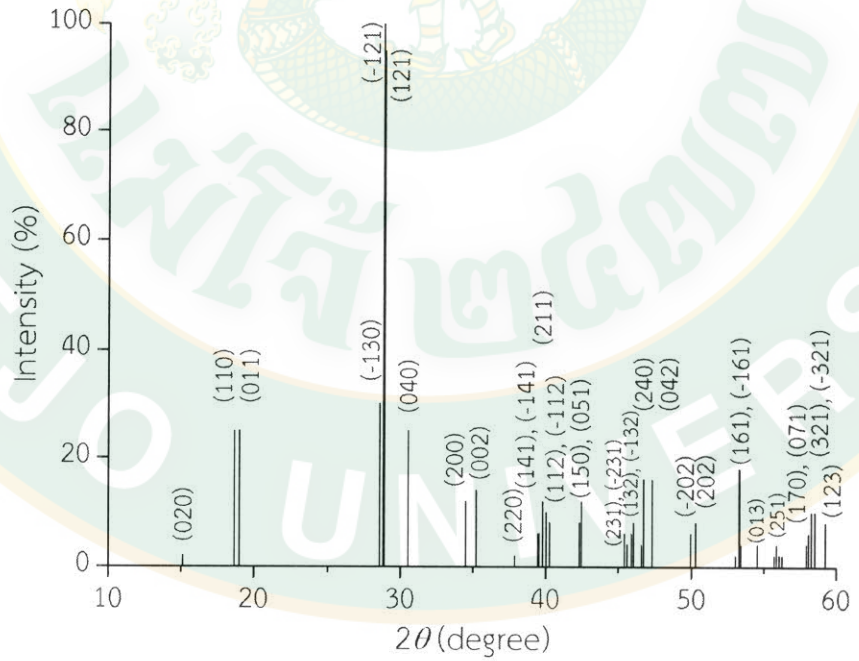

Peak list of bismuth vanadium oxide

No.	h	k	l	d [Å]	2θ	Intensity [%]
1	0	2	0	5.84700	15.141	2.0
2	1	1	0	4.74900	18.670	25.0
3	0	1	1	4.67000	18.988	25.0
4	-1	3	0	3.12000	28.587	30.0
5	-1	2	1	3.09500	28.823	100.0
6	1	2	1	3.08200	28.947	95.0
7	0	4	0	2.92400	30.549	25.0
8	2	0	0	2.59800	34.495	12.0
9	0	0	2	2.54600	35.222	14.0
10	2	2	0	2.37400	37.867	2.0
11	-1	4	1	2.28200	39.456	6.0
12	1	4	1	2.27700	39.546	6.0
13	2	1	1	2.26400	39.783	12.0
14	-1	1	2	2.25000	40.041	10.0
15	1	1	2	2.23900	40.246	8.0
16	1	5	0	2.13300	42.340	8.0
17	0	5	1	2.12700	42.465	12.0
18	-2	3	1	1.99500	45.426	6.0
19	2	3	1	1.98800	45.595	4.0
20	-1	3	2	1.97600	45.888	6.0
21	1	3	2	1.97000	46.035	8.0
22	0	6	0	1.94900	46.560	4.0
23	2	4	0	1.94300	46.713	16.0
24	0	4	2	1.92000	47.306	16.0
25	-2	0	2	1.82400	49.961	6.0
26	2	0	2	1.81200	50.315	8.0
27	2	2	2	1.72600	53.012	2.0
28	-1	6	1	1.71900	53.245	18.0

29	1	6	1	1.71700	53.312	18.0
30	3	1	0	1.71300	53.446	4.0
31	0	1	3	1.68000	54.582	4.0
32	-2	5	1	1.64800	55.733	2.0
33	2	5	1	1.64400	55.881	4.0
34	-1	5	2	1.63900	56.066	2.0
35	1	5	2	1.63300	56.291	2.0
36	1	7	0	1.59100	57.915	4.0
37	0	7	1	1.58700	58.075	6.0
38	-3	2	1	1.58200	58.276	10.0
39	3	2	1	1.57570	58.532	10.0
40	1	2	3	1.55800	59.262	8.0

Name and formula

Reference code:	01-079-2381
Mineral name:	Russellite, syn
PDF index name:	Bismuth Tungsten Oxide
Empirical formula:	Bi_2O_6W
Chemical formula:	$Bi_2(WO_6)$

Crystallographic parameters

Crystal system:	Orthorhombic
Space group:	Pca21
Space group number:	29
a (Å):	5.4373
b (Å):	16.4302
c (Å):	5.4584
Alpha (°):	90.0000
Beta (°):	90.0000
Gamma (°):	90.0000
Calculated density (g cm^{-3}):	9.50
Volume of cell (10^6 pm^3):	487.63
Z:	4.00

Subfiles and Quality

Subfiles:	Inorganic
	Mineral
	Corrosion
	Modelled additional pattern
Quality:	Calculated (C)

Comments

ICSD collection code: 067647

Test from ICSD: At least one TF implausible

References

Primary reference: *Calculated from ICSD using POWD-12++*(1997)

Structure: Knight, K.S., *Mineral. Mag.*, 56, 399, (1992)

Stick Pattern

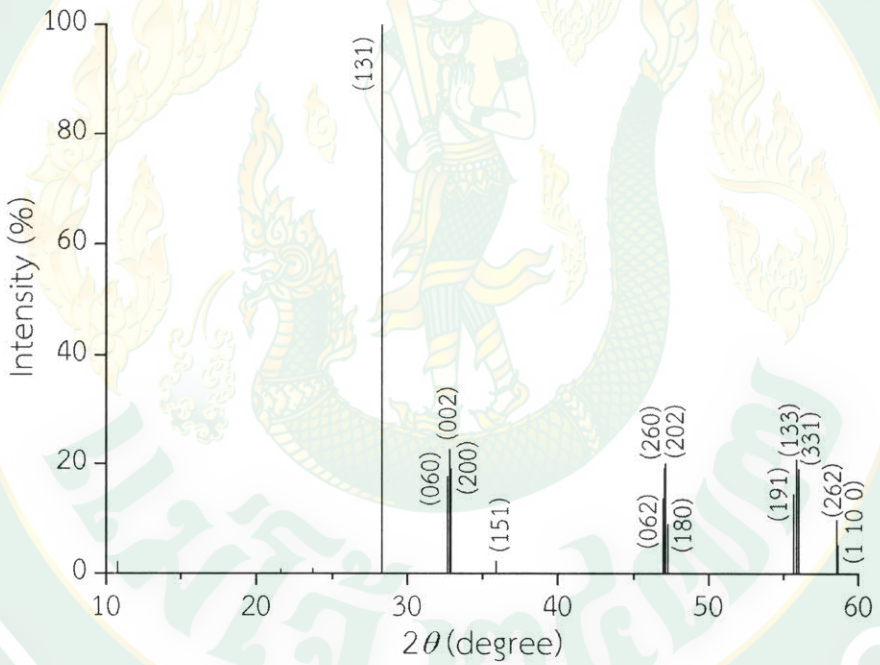

Peak list of bismuth tungsten oxide

No.	h	k	l	d [Å]	2θ	Intensity [%]
1	0	1	0	16.43020	5.374	0.1
2	0	2	0	8.21509	10.761	2.1
3	0	3	0	5.47673	16.171	0.1
4	1	1	0	5.16195	17.164	0.1
5	1	2	0	453410	19.563	1.0
6	0	4	0	4.10754	21.618	0.7
7	1	3	0	3.85860	23.031	0.1
8	1	1	1	3.75078	23.704	0.8
9	1	2	1	3.48777	25.519	0.1
10	1	4	0	3.27745	27.187	0.6
11	1	3	1	3.15083	28.302	100.0
12	0	6	0	2.73836	32.676	17.6
13	0	0	2	2.72921	32.788	22.7
14	2	0	0	2.71863	32.919	19.1
15	0	2	2	2.59002	34.604	0.4
16	2	2	0	2.58097	34.730	0.3
17	1	5	1	2.50002	35.892	2.2
18	1	6	0	2.44571	36.717	0.1
19	2	3	0	2.43350	36.908	0.1
20	2	1	1	2.40724	37.325	0.8
21	1	2	2	2.33829	38.468	0.4
22	2	2	1	2.33328	38.554	0.2
23	0	4	2	2.27318	39.615	0.1
24	2	4	0	2.26705	39.727	0.2
25	1	3	2	2.22818	40.450	0.1
26	2	3	1	2.22385	40.532	0.1
27	1	7	0	2.15495	41.888	0.1
28	1	4	2	2.09727	43.097	0.1

29	2	4	1	2.09365	43.175	0.1
30	0	8	0	2.05377	44.057	0.1
31	1	7	1	2.00440	45.201	0.5
32	2	5	1	1.95563	46.393	0.5
33	0	6	2	1.93307	46.967	13.6
34	2	6	0	1.92930	47.064	19.2
35	2	0	2	1.92609	47.148	20.0
36	1	8	0	1.92128	47.273	9.0
37	2	2	2	1.87524	48.507	0.5
38	2	6	1	1.81902	50.108	0.1
39	3	1	0	1.80149	50.629	0.1
40	0	7	2	1.77957	51.298	0.1
41	3	2	0	1.76986	51.600	0.6
42	2	4	2	1.74389	52.427	0.3
43	1	9	0	1.73063	52.859	0.1
44	1	1	3	1.71599	53.346	0.5
45	3	1	1	1.71073	53.523	0.3
46	2	7	1	1.68940	54.254	0.5
47	3	2	1	1.68357	54.457	0.3
48	3	4	0	1.65818	55.362	0.7
49	1	9	1	1.64970	55.671	14.4
50	1	3	3	1.64569	55.818	20.8
51	3	3	1	1.64104	55.990	19.0
52	1	4	3	1.59078	57.924	0.1
53	3	5	0	1.58703	58.074	0.1
54	2	6	2	1.57541	58.543	9.8
55	1	10	0	1.57278	58.651	5.3
56	1	5	3	1.52764	60.562	0.4

XRD pattern of $BiVO_4$ synthesized at pH 6

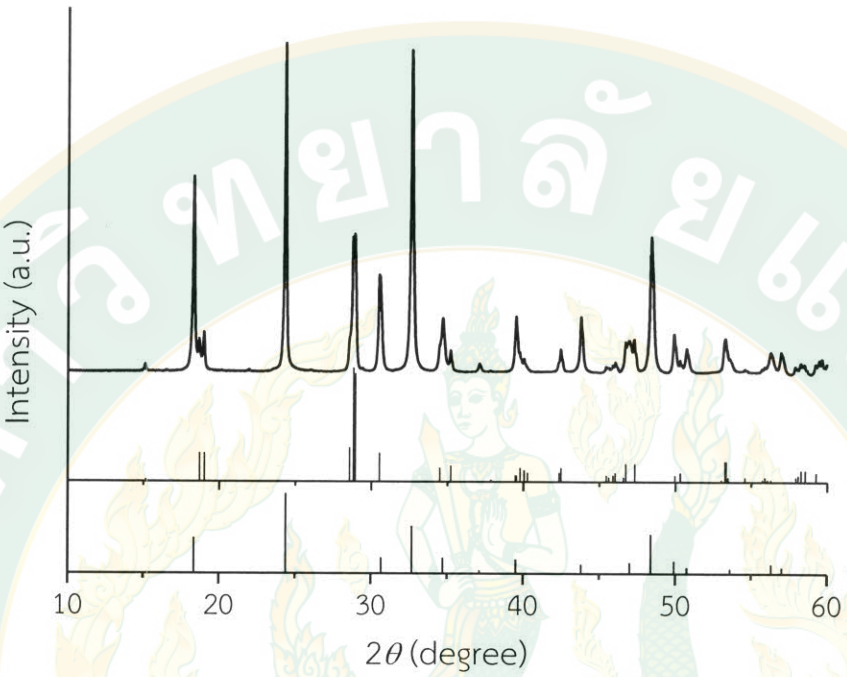

XRD patterns of $BiVO_4$ powder synthesized at pH 6 by ET method at 200 °C for 4 h.

It was found that $BiVO_4$ powder synthesized at pH 6 showed mixed phases of tetragonal and monoclinic phase where tetragonal phase was more than monoclinic phase (69.6 : 30.4).

Percentage of phase composition was calculated from ratio of intensity of the highest peak as following equation (Bhattacharya et al., 1997):

$$\%\text{monoclinic phase} = \frac{I_{mono}}{I_{tetra} + I_{mono}} \times 100$$

I_{mono} is the intensity of [-121] plane

I_{tetra} is the intensity of [200] plane

For example: from above XRD pattern;

$$\%\text{monoclinic phase} = \frac{69501}{162869 + 69501} \times 100$$

$$= 29.90\%$$

So that %monoclinic phase is about 30%.

Scherrer's equation

Crystalline size was estimated from the Scherrer equation (Ohtani, 2008).

$$D = \frac{K\lambda}{\beta \cos\theta}$$

where

D is the crystalline size

λ is the wavelength of the X-ray radiation (0.154 nm)

K is taken as 0.89

β is peak widths at haft-maximum intensity of the sample

2θ is around 28.9°

For example: from XRD pattern of $BiVO_4$ powder synthesized at pH 7,

Peak intensity at 2θ = 28.9 is 259445.8 a.u., then, peak width at 129722.9 a.u. is 29.0 - 28.7 = 0.3 degree.

So that, β = 0.005236 radian

and θ = 28.9/2 degree

= 0.252287 radian

Substitute values in the equation

$$D = \frac{(0.89)(0.154)}{(0.0052)(\cos(0.25))}$$

$$= 27 \text{ nm}$$

UV–Visible Diffuse Reflectance Spectroscopy (UV-Vis DRS)

Barium sulphate ($BaSO_4$) powder is used as a reference material. First, $BaSO_4$ powder is put in a circular sample holder and press it to make it uniform. It is analyzed as a blank sample. Then amount of your sample press and rotate to make uniform and smooth surface. Then it is monitored by UV/Vis. spectroscopy in term of %reflectance (%R).

Principal of UV-Vis DRS.

UV-Vis DRS brand Shimadzu UV-2600.

Comparison between general UV-Vis spectroscopy and DRS

UV-Vis.	DRS
H_2/D_2 lamp , Tungsten lamp	
Excite valence electrons to empty orbitals	
Solution	Solid
Relative change of transmittance of light	Relative change of reflected light of surface
Blank = Clear solution	Blank = White powder

The band gap energy (E_g) was evaluated using the modified Kubelka-Munk method as the following equation:

$$F(R) = \frac{(1-R)^2}{2R}$$

where R is the reflectance.

F(R) is functioning of reflectance which proportional to absorbance coefficient (α).

$$(\alpha h\nu)^2 = A(h\nu - E_g)^n$$

where A, α, and $h\nu$ are a constant, the absorption coefficient, and the incident photon energy, respectively, while n is 1 for bismuth vanadate ($BiVO_4$)

$$(\alpha h\nu)^2 = Ah\nu - AE_g$$

$$(\alpha E)^2 = AE - AE_g$$

Or

$$(F(R)E)^2 = AE - AE_g$$

From figures below, E_g = 2.6 eV.

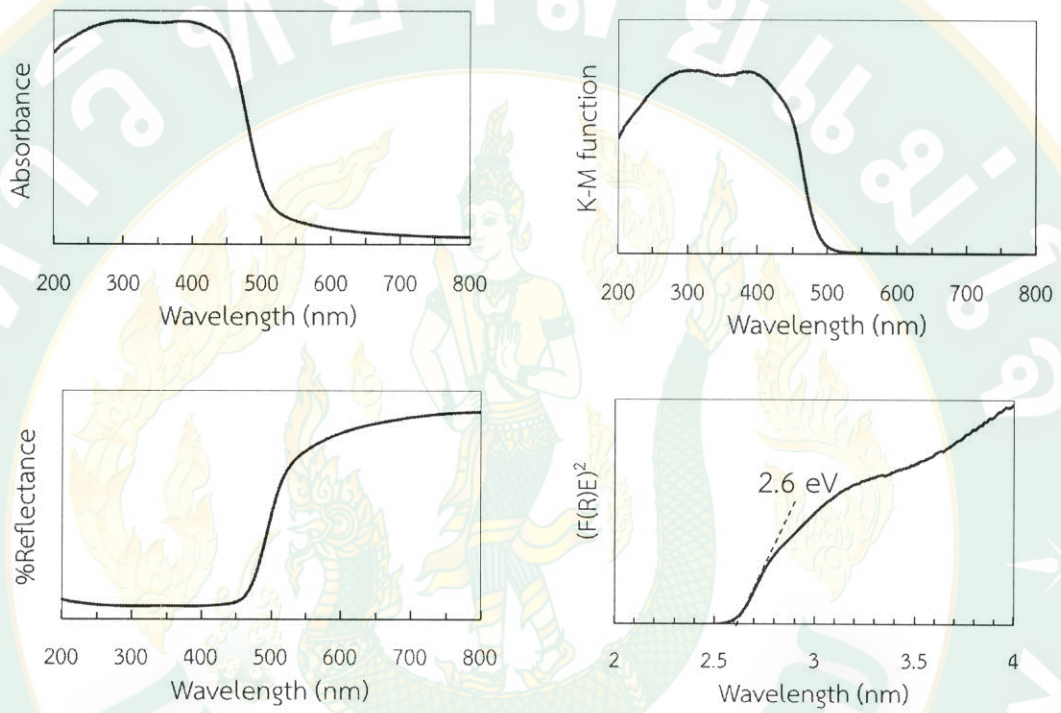

Measuring of E_g of $BiVO_4$ sample synthesized by ET method at 200 °C 4 h.

X-ray Absorption Spectroscopy (XAS)

X-ray Absorption or XAS is the spectroscopy use to observe fine structure and oscillation of X-ray absorption when scanning photon energy. The X-ray is a tunable monochromatic X-rays with enough photon energy for absorption of a selected element.

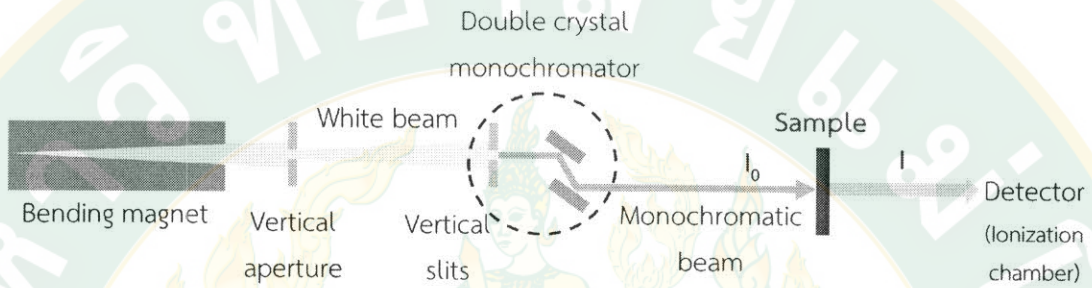

Schematic of XAS instrument.

Absorption is measured directly by measuring what is transmitted through the sample.

$$I = I_0 e^{-\mu T}$$

I = Intensity of X-ray after absorption

I_0 = Intensity of X-ray before absorption

μ = Linear absorption coefficient

T = Thickness of sample

Transmission mode which absorption is measured directly is suitable for a sample contain more than 5%wt of absorbing element. Sample environment are air and helium. I_0 and I are measured by using ionization chambers detector.

$$\mu(E) = \ln(I_0/I)$$

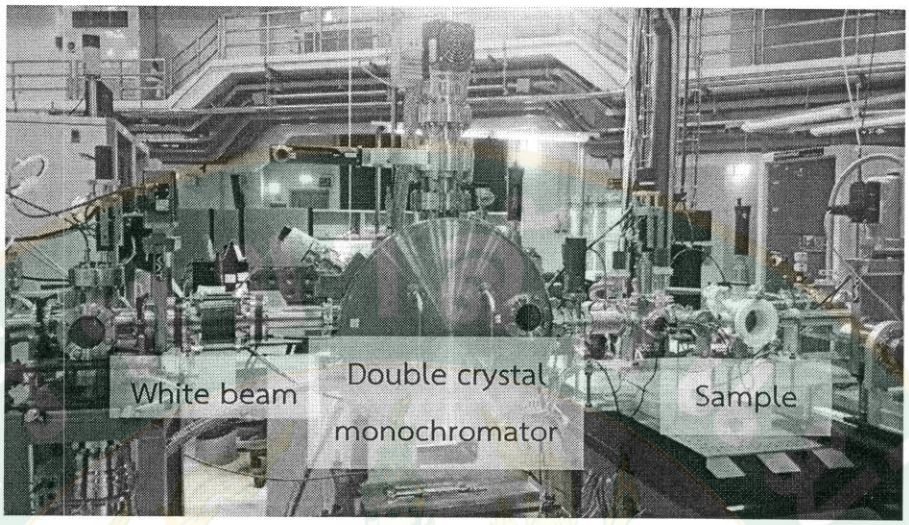

XAS at BL 5.2 of The Synchrotron Light Research Institute,
Nakhon Ratchasima, Thailand.

X-ray Absorption Near Edge Structure (XANES)

- caused by electronic transition from a core level to unoccupied state
- information of oxidation states, local geometry

Extended X-ray Absorption Fine Structure (EXAFS)

- spectrum conforms constructive and destructive scattering of a photoelectron
- information of local environmental around probing atom

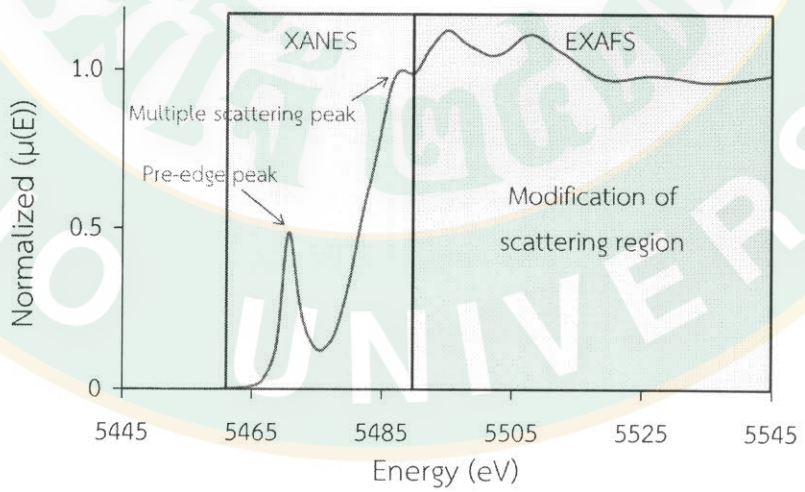

XAS spectrum of standard vanadium (V) oxide (V_2O_5).

Pre-edge: Small (or large, certainly meaningful) feature between the Femi energy and the threshold (equal to K-edge energy). This peak causes by transitions to unoccupied orbitals.

Edge: The main rising part of XAS spectrum. They are multiple scattering peaks.

Near-edge: Characteristic features above the edge

EXAFS oscillations come from constructive scattering (CS) and destructive scattering (DS) as showed in this figure:

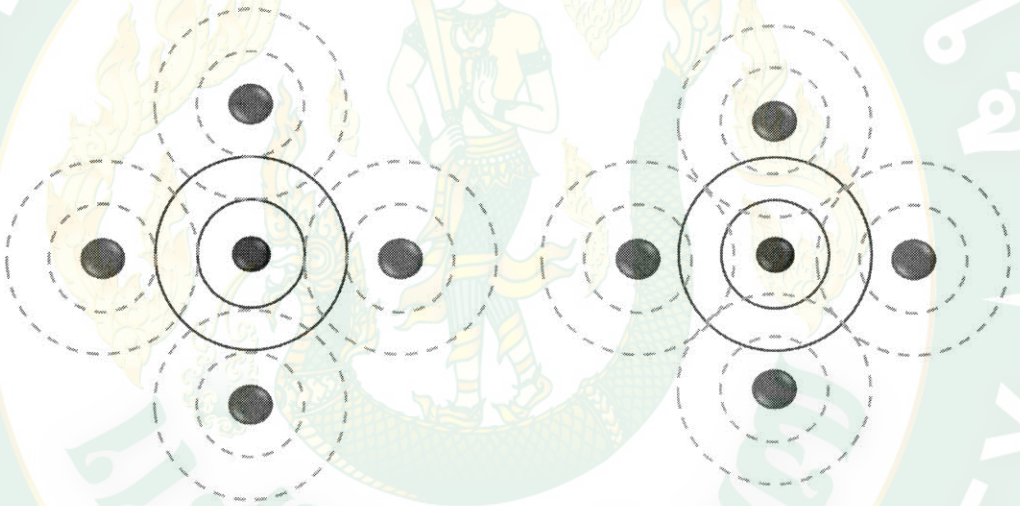

Constructive scattering (CS). Destructive scattering (DS).

EXAFS structure (χ(k)) arises from scattering wave from all neighbor atoms around the absorbing element. Frequency of the wave represents distance from the neighbors and amplitude represent number and type of neighbors.

k = Wave number of photon

$$k = \sqrt{\frac{2m}{\hbar^2}(E - E_0)}$$

m = Electron mass

E_0 = Threshold energy or ionization energy

Number of neighbors Back-scattering amplitude Disorder in interatomic distance

$$\chi(k) = \sum \frac{NjS_0^2 f_i(k) e^{-2k^2\sigma_j^2}}{kR_j^2} \sin\left[2kR_j + \delta_j(k)\right]$$

Neighbors distance Atomic phase shift

Atom of the same type at the same distance from the absorber groups in a shell indexed by j.

N = Number of neighbor atoms at the same distance (R) (coordination number)

S_0^2 = passive electron reduction factor (relaxation effect in presence of core hole)

R = Distance between the absorbing atom and the neighbor atoms (bond distance)

σ^2 = mean square displacement in distance (R)

f(k) = effective scatterin amplitutde of atom type j

$\lambda(k)$ = photoelectron mean free path (to ensure elastic scattering)

$\delta(k)$ = effective scattering phase shift of photoelectron scattered wave

Note: N, S_0^2, R, σ^2 and E_0 are parameters determined by modeling data

f(k), $\lambda(k)$ and $\delta(k)$ are parameters calculated by theoretical calculations (FEFF)

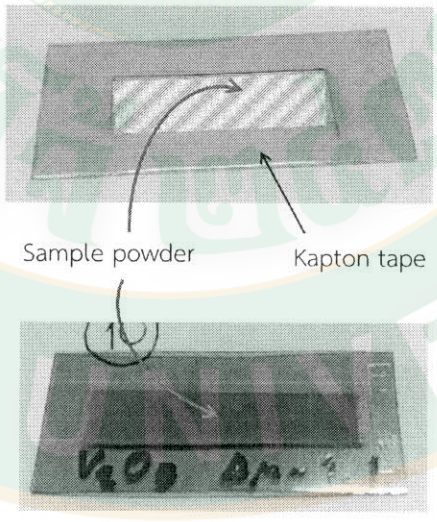

Sample preparation by two-side kapton for high concentrate sample.

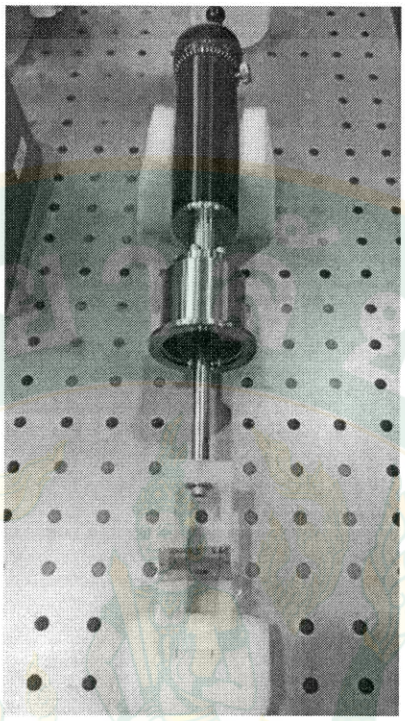

Sample holder for XAS measurement.

Revered double-beam photoacoustic spectroscopy (RDB-PAS)

Photoacoustic spectroscopy (PAS) is one of the photothermal spectroscopic techniques and the PA spectrum corresponds to photoabsortption spectrum.

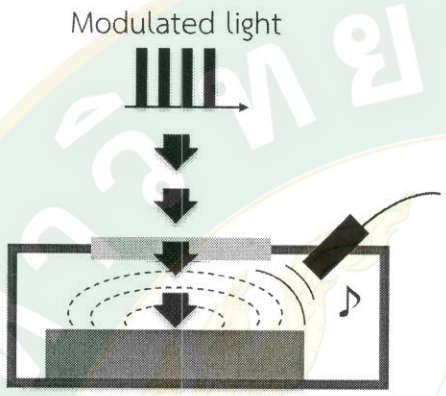

PAS spectroscopy.

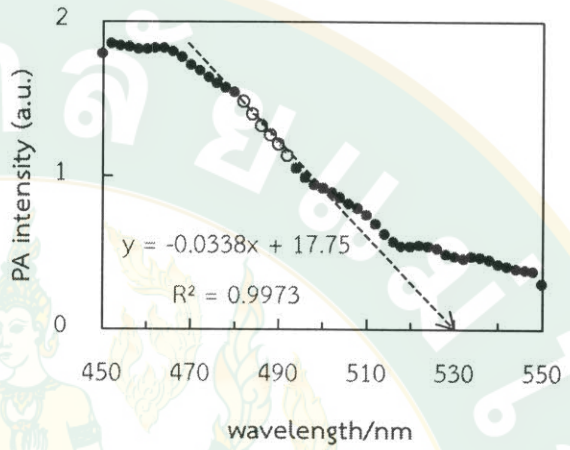

RDB-PA spectrum.

From the equation of straight line of PA spectrum of $BiVO_4$;

$$y = -0.0338x + 17.75$$

According to raw data at 530 nm, PA intensity (y) = 0.46019;

$$x = (0.46019-17.75)/(-0.0338)$$

$$x = 511.5$$

$$CBB = 1240/x$$

$$= 2.424 \text{ eV}$$

In the RDB-PAS measurement, electrons are accumulated in ETs from deeper side to shallower side under irradiation of scanned continuous light for excitation of valence-band (VB) electrons directly to ETs. About 220 g of sample powder is put into a home-made aluminum PAS cell with a quartz window sample holder. During the process, photoabsorption of the accumulated electrons is detected by modulated LED light of 625 nm at 80 Hz. Under methanol saturated argon gas atmosphere, the obtained spectrum corresponds to an action spectrum of reactions for direct excitation from VB to ETs.

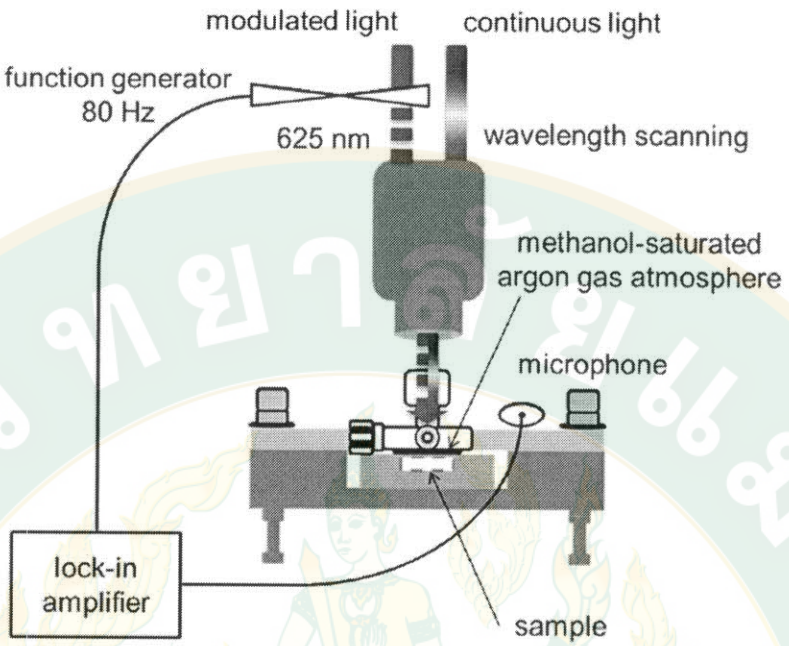

Schematic representation of the setup for RDB-PAS.

[A. Nitta, M. Takase, M. Takashima, N. Murakami, B. Ohtani, *Chem. Commun.*, 52, 12096–12099 (2016).]

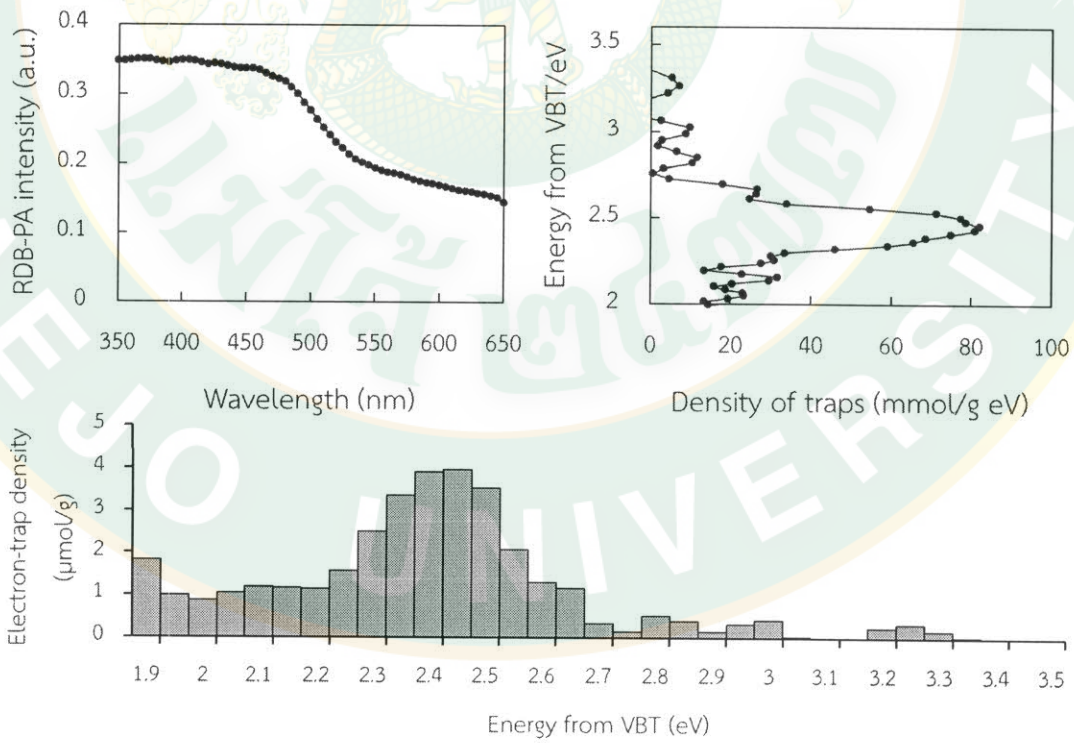

RDB-PAS data analysis.

Calculation of band edge position of conduction band and valence band

The conduction band (CB) and valence band (VB) potentials of a semiconductor can be calculated using the following equation:

$$E^{\circ}_{CB} = X - E^{c} - (1/2)E_g$$

X is the absolute electronegativity; defined as the arithmetic mean of the electron affinity and the first ionization of the constituent atoms

X of $BiVO_4$ = 6.035 eV

X of Bi_2WO_6 = 6.2 eV

E^{c} is the energy of free electron on the hydrogen scale (4.5 eV)

E_g is band gap energy of the semiconductor evaluated by UV-Vis DRS spectroscopy

For $BiVO_4$;

$$E^{\circ}_{CB} = 6.035 - 4.5 - (1/2)2.53$$

$$= 0.27 \text{ eV}$$

$$E^{\circ}_{VB} = E^{\circ}_{CB} + E_g$$

So that $E^{\circ}_{VB} = 2.53 + 0.27$ eV

$$= 2.80 \text{ eV}$$

CB and VB band positions are 0.27 and

For Bi_2WO_6;

$$E^{\circ}_{CB} = 6.2 - 4.5 - (1/2)2.65$$

$$= 0.37 \text{ eV}$$

So that $E^{\circ}_{VB} = 2.65 + 0.37$ eV

$$= 3.02 \text{ eV}$$

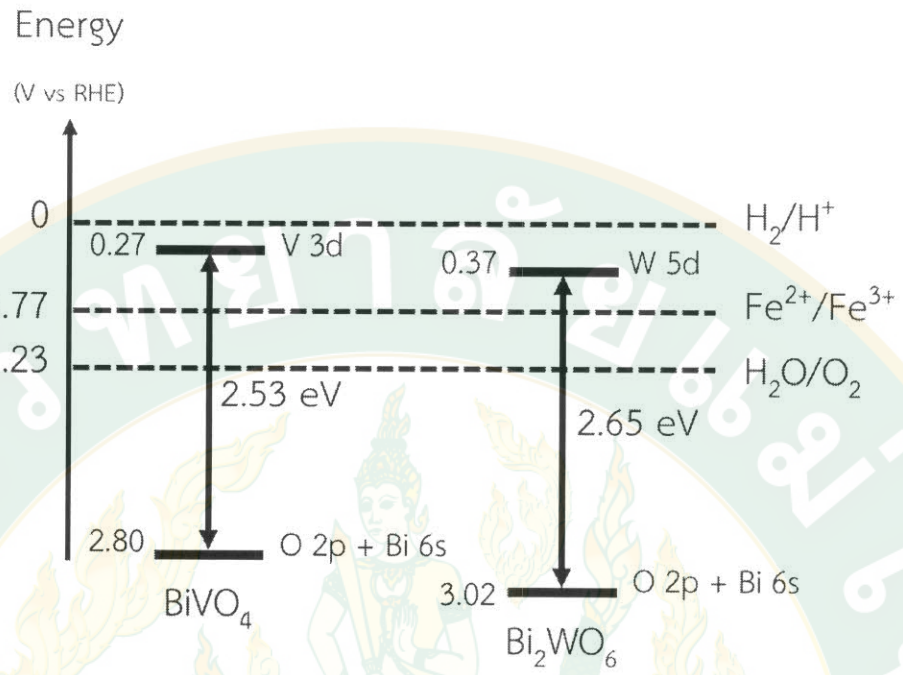

Presumption of possible CB and VB potential positions of synthesized $BiVO_4$ powder and FB-Bi_2WO_6 powder.

PHOTOCATALYSIS

Photodegradation mechanism of methyl orange (MO) (Luan et al., 2014)

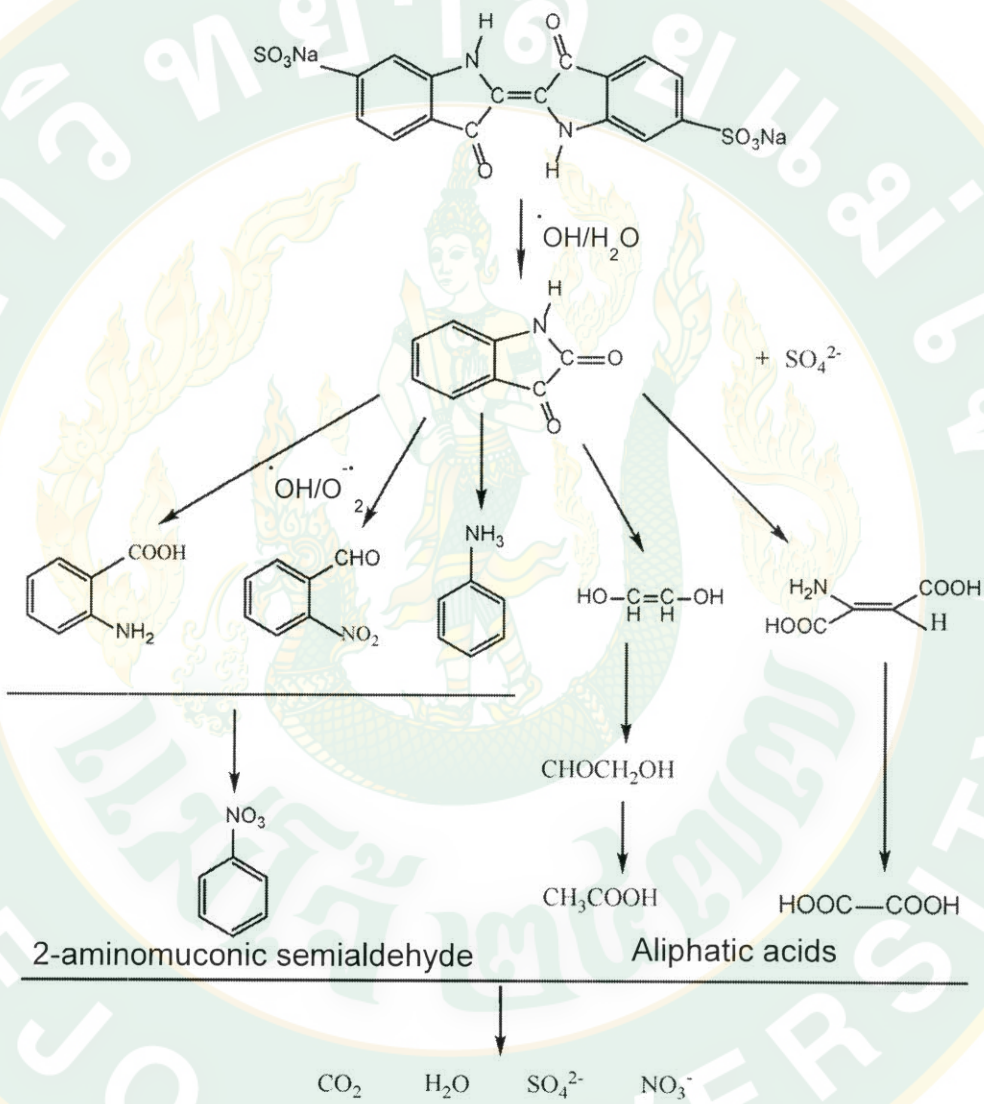

Degradation mechanism of a MO molecule.

Calibration graph for MO

Table of absorbance of MO at various concentrations

Concentration (ppm)	Absorbance
0	0
1	0.0604
3	0.211
5	0.353
6	0.419
7.5	0.525
10	0.699
15	1.04
20	1.39

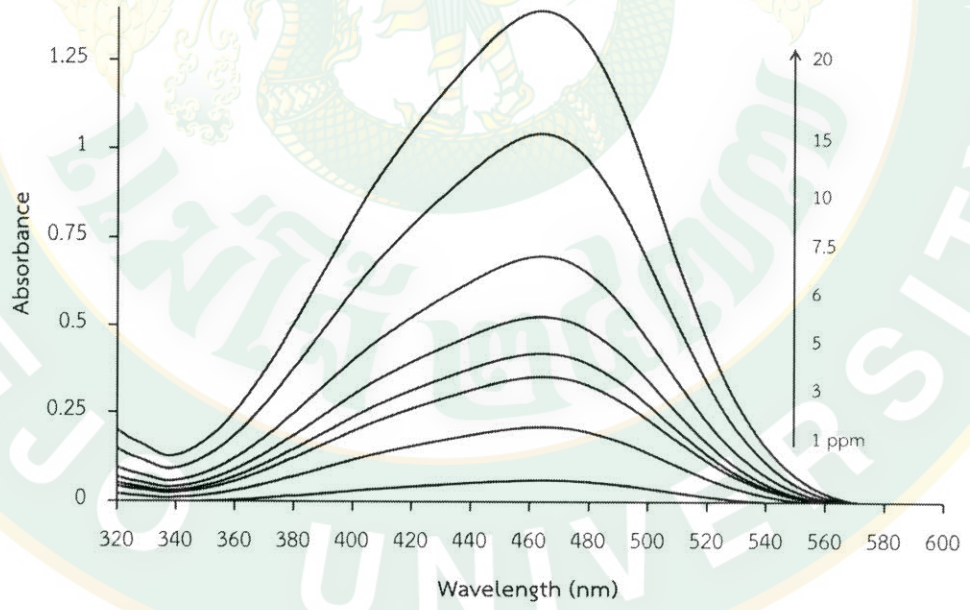

Absorption spectrum: scanning from 200 to 800 nm using deionized water as a blank solution.

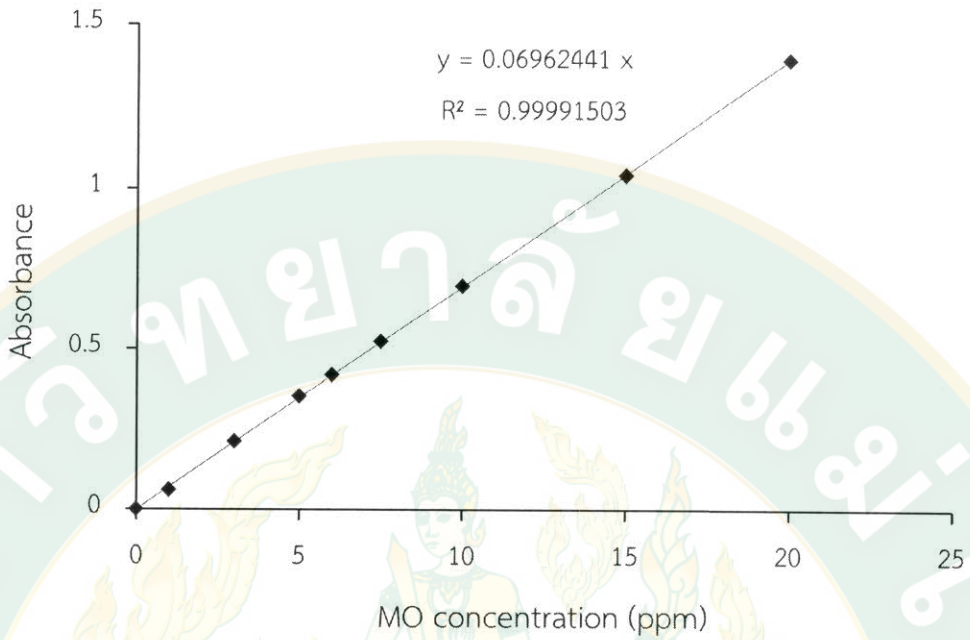

Calibration graph for standard MO.

Amount of MO calculates from calibration equation.

$$\%\text{degradation} = \frac{C_0 - C_t}{C_0} \times 100$$

C_0 = Concentration of MO at time = 0

C_t = Concentration of MO at time = t

Calculation of amount of oxygen generated from photocatalysis

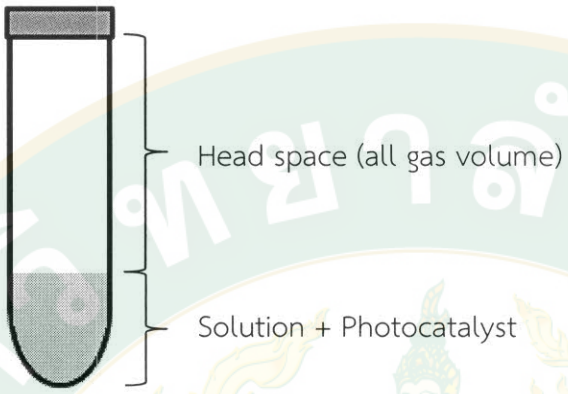

A glass reactor for studying oxygen liberation photocatalysis.

After photoirradiation, oxygen gas is liberated. Amount of the liberated gas is calculated by following equations;

According to ratio of amount of injected gas per injected gas volume is equal to amount of all gas per all volume

Injection volume : All volume

$$v\ (L) / Y\ (mol) = (Z + 22.4X)\ (L) / X\ (mol)$$

Z = Head space (L)

v = Injected volume (L)

X = Mole of generated gas (mol)

Y = Mole of injected gas (mol)

From ideal gas; 1 mol of gas = 22.4 L at 1 atm, 273K

So that X mol of gas = 22.4X

From relation of mole of gas in injection and all volume we will get;

$$Y = \frac{Xv}{(V + 22.4X)}$$

$$Y(Z + 22.4X) = Xv$$

$$YZ + 22.4XY = Xv$$

$$Xv - 22.4XY = YZ$$

$$X(v - 22.4Y) = Y$$

So that amount of oxygen X is;

$$X = \frac{YZ}{(v - 22.4Y)}$$

However, there is some nitrogen gas and oxygen gas from air that should be eliminates to get the correct area of oxygen ($A_{correct}$). The $A_{correct}$ is amount of oxygen liberation minute amount of oxygen from air flow.

$$A_{correct} = A - (B \times \frac{\beta}{\alpha})$$

A = Peak area of oxygen gas

B = Peak area of nitrogen gas from air in flow

β = Peak area of oxygen gas in air

α = Peak area of nitrogen gas in air

$$Y = A_{correct} \times a$$

a = factor (slope of oxygen calibration graph)

Calibration graph for oxygen

Table of amount of oxygen gas in various injection volumes

Injection volume (mL)	Area	O_2 (μmol)	Time (min)
0.05	11471	0.42832188	1.316
0.10	22766	0.856643761	1.318
0.15	34549	1.284965641	1.315
0.20	45869	1.713287521	1.313
0.25	57217	2.141609402	1.315

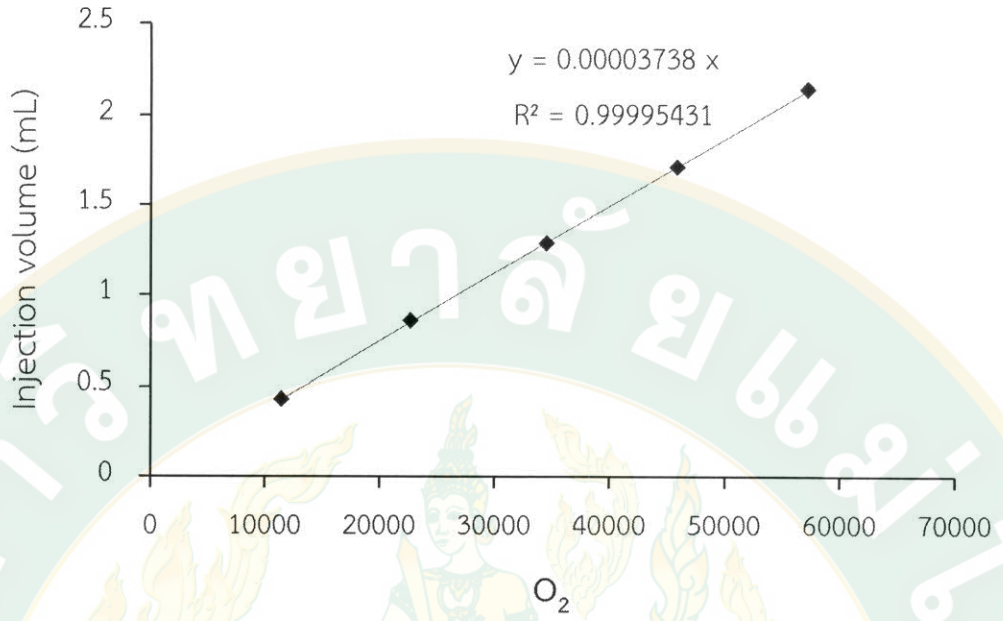

Calibration graph for oxygen gas liberation; a = 3.738×10^{-5}.

VITA

NAME	Miss Pradudnet Ketwong	
DATE OF BIRTH	March 25, 1986	
EDUCATION	2004 – 2008	B.Sc. in Chemistry, Faculty of Science, Maejo University, Thailand
	2008 – 2011	M.Sc. in Physical Chemistry, Faculty of Science, Mahidol University, Thailand
	2014 – 2018	Ph.D. in Applied Chemistry Faculty of Science, Maejo University, Thailand
WORK EXPERIENCE	2008 – 2011	Teaching Assistant, Mahidol University, Thailand
	2011	Chemistry teacher, Regina Coeli College, Chiang Mai, Thailand
	2012	Research Assistant at Energy, Fuel and Petrochemicals Research Laboratory, Chiang Mai University, Thailand
	2014	Researcher, CPF - Charoen Pokphand Foods Public Company Limited
	2015	Teaching Assistant, Maejo University, Thailand
EMAIL:	pradudnet@gmail.com	

PUBLICATIONS

1. Ketwong, P., Kidkhunthod, P. & Pookmanee, P. 2016. Effect of ethanol assistance on chemical structure of ferroelectric bismuth vanadate via solvothermal method. **Integrated Ferroelectrics**, 175(1), 9–17.

2. Ketwong, P., Takashima, M., Nitta, A., Pookmanee, P., & Ohtani, B. 2018. Hydrothermal synthesis and photocatalytic activities of stabilized bismuth vanadate/bismuth tungstate composites. **Journal of Environmental Chemical Engineering**, (In Press) DOI: https://doi.org/10.1016/j.jece.2018.01.062.

CONFERENCES

1. Oral presentation: Low-temperature ethanothermal synthesis and characterization of bismuth vanadate nanoparticle. The 7th International Workshop on Advanced Materials Science and Nanotechnology (IWAMSN2014) on November 2 – 6, 2014 in Ha Long City, Vietnam.

2. Poster presentation: Effect of ethanol assistance on chemical structure of ferroelectric bismuth vanadate via solvothermal method. 10th International Conference on the Physical Properties and Application of Advanced Materials (ICPMAT2015) on November 17–21, 2015 in Chiang Mai, Thailand.

3. Poster presentation: Rapid preparation and oxygen-evolution photocatalytic activity of monoclinic scheelite bismuth vanadate powder. The 35th Photocatalytic Chemical Symposium on June 10, 2016 at the Tokyo Institute of Technology, Tokyo, Japan.

4. Poster presentation: Photocatalytic oxygen evolution by bismuth vanadate-bismuth tungstate composites under visible-light irradiation. The 56th Aurora Seminar on July 24–25, 2016 at the Biratori Onsen Yukara, Biratori, Hokkaido, Japan.

5. Poster presentation: Preparation and photocatalytic activity of bismuth-vanadate particles stabilized on bismuth-tungstate macroparticles. Electric Chemistry Conference of Hokkaido-Tokai Branch on November 23–24, 2016 at Hokkaido University, Sapporo, Hokkaido, Japan.

6. Oral presentation: Visible light-induced photocatalytic oxygen evolution using bismuth vanadate/bismuth tungstate composites. Winter Conference of Hokkaido Branch on January 17–18, 2017 at Hokkaido University, Sapporo, Hokkaido, Japan.

7. Poster presentation: Stabilization of bismuth vanadate on bismuth tungstate flake-ball particles for sustainable photocatalysis under visible light. The 1st ACS Asia-Pacific International Chapters Conference (APICC) on November 5–8, 2017 at International Convention Center Jeju, Jeju, South Korea.

SCHORLARSHIPS

1. Science Achievement Scholarship of Thailand (SAST) from August 1, 2014 to July 31, 2017.

2. Short-term research scholarship from SAST to do research at Institute for Catalysis (ICAT), Hokkaido University, Sapporo, Japan from February 1, 2016 to January 31, 2017.

OTHER ACTIVITIES

1. XAS Tutorial on Selected Topics Training Program on July 16 – 17, 2014 at The Tide Resort, Chonburi, Thailand.

2. Applications of Synchrotron Radiation on Materials Science Training Program on October 1 – 2, 2014 at Faculty of Science, Chiang Mai University, Chiang Mai, Thailand.

3. Applications of XAS technique for in-depth analysis of elemental and structural components of compounds on December 1 , 2014 at Chiang Mai Grandview Hotel & Convention Center, Chiang Mai, Thailand.

4. Work as a staff of the 35th International Conference of The Microscopy Society of Thailand (MST35) on January 30 to February 2, 2018 at The Imperial Mae Ping Hotel, Chiang Mai, Thailand.

INTEGRATED FERROELECTRICS
2016, VOL. 175, 9–17
http://dx.doi.org/10.1080/10584587.2016.1199239

Taylor & Francis
Taylor & Francis Group

Effect of ethanol assistance on chemical structure of ferroelectric bismuth vanadate *via* solvothermal method

Pradudnet Ketwong[a], Pinit Kidkhunthod[b], and Pusit Pookmanee[a]

[a]Department of Applied Chemistry, Faculty of Science, Maejo University, Chiang Mai, Thailand; [b]Synchrotron Light Research Institute (Public Organization), Nakhon Ratchasima, Thailand

ABSTRACT

Bismuth vanadate ($BiVO_4$) was synthesized *via* ethanol-assisted solvothermal method performing at heating temperature of 200°C for 2–6 h. Characteristics of $BiVO_4$ were investigated by X-ray diffraction, field emission-scanning microscopy and Brunauer, Emmett and Teller technique. Single monoclinic phase with T-shape like particles was obtained and average crystalline sizes as well as surface area were improved by a prolonged reaction time. Electron transitions in the structure were described by diffuse reflectance of the $BiVO_4$. Moreover, X-ray absorption spectra at vanadium K-edge were presented in more information of chemical structure of vanadium's oxidation state and bond distance between vanadium and oxygen.

ARTICLE HISTORY
Received 28 November 2015
Accepted 28 March 2016

KEYWORDS
Bismuth vanadate; ethanol-assisted solvothermal; chemical structure; X-ray absorption spectroscopy

Introduction

$BiVO_4$ is a ferroelectric/ferroelastic material that has attracted interest from many researchers [1–3]. There has also been a rapid increase in the number of international publications that have reported on its performance.

$BiVO_4$ has been studied in applications as a photocatalyst [4], non-toxic pigment [5] and conductor [6]. Crystalline structure of $BiVO_4$ is divided mainly into three types: monoclinic scheelite, tetragonal scheelite and tetragonal zircon structure [7]. Among these, the monoclinic structure presents ferroelectric and ferroelastic properties due to phase transition by external pressure and stress inducement [8]. Moreover, it shows the highest photocatalytic activity under visible light due to band gap energy of the monoclinic structure $BiVO_4$ ranges from 2.4 to 2.5 eV. This narrow band gap allows the catalyst to absorb energy in the visible light region [7, 9]. Although the monoclinic structure can be synthesized by various methods such as: solid-state reaction [10], co-precipitation method [11], hydrothermal method [12] and solvothermal method [13], however, these methods result in different crystal formations, particle sizes, surface areas and photocatalytic efficiency of $BiVO_4$. Nanoparticle with homogeneous particle size distribution and high efficiency can be obtained in mild conditions by the hydrothermal [14] or solvothermal [15]. In

CONTACT Pusit Pookmanee pusit@mju.ac.th

addition, the chemical structure of $BiVO_4$ has an extremely high impact on its photocatalytic performance. Crystalline structures of the $BiVO_4$ synthesized by hydrothermal method showed that the crystalline structures were depending on hydrothermal temperature. Mixed phases of tetragonal and monoclinic $BiVO_4$ were obtained at 140°C, after increasing heating temperature, the tetragonal structure was transferred to monoclinic structure and pure monoclinic was performed at 180°C [16]. Furthermore, the pure monoclinic had significantly higher photoactivity than the tetragonal. Photocatalytic performance of monoclinic $BiVO_4$ synthesized by surfactant-ethanol-assisted hydrothermal using sodium hydroxide (NaOH) for pH adjustment was studied and showed that surface area, crystalline phase and chemical structure of $BiVO_4$ had a strong influence on photocatalytic activity for photodegradation of methyl orange (MO) [17]. In addition, $BiVO_4$ synthesized by the solvothermal method using binary green solvent of water and ethanol compared with pure water were studied [18]. The result showed that the crystalline phase of $BiVO_4$ prepared by both binary solvent and pure water were presenting a monoclinic phase. However, percentage of degradation of rhodamine B (RhB) under visible-light irradiation using $BiVO_4$ synthesized by ethanol-water mixed solvent was exhibiting extremely higher than pure water.

In this research, $BiVO_4$ was synthesized *via* ethanol-assisted solvothermal at various heat treatment times without a surfactant and calcination process. Effect of ethanol assistance on crystalline phase, morphology, physical properties such as surface area and band gap energy and chemical structure of the $BiVO_4$ was investigated and discussed.

Experimental

Synthesis

$BiVO_4$ was synthesized using the ethanol-assisted solvothermal method with the Bi and V ratio of 1:1. Solution A was prepared by dissolving 10 mmol bismuth nitrate pentahydrate ($Bi(NO_3)_3.5H_2O$) (Ajax Finechem, New Zealand) in 20 mL of 6 M nitric acid (HNO_3) (RCI Labscan, Thailand). Meanwhile, solution B was prepared by dissolving 10 mmol ammonium metavanadate (NH_4VO_3) (Ajax Finechem, New Zealand) in 40 mL of 5 M ammonium hydroxide (NH_4OH) (J.T. Baker, USA). After that, solution B was slowly and carefully dropped into solution A while continuously stirring. The pH of the mixture was adjusted to 7. The mixture became yellow slurry. Then, 100 mL of absolute ethanol (C_2H_5OH) (Liquor Distillery Organization Excise Department, Thailand) was poured into the mixture. It was stirred for 60 minutes before adding some absolute ethanol to make the final volume 200 mL and transferred to a 1,000 mL Teflon-lined stainless steel reactor (Thailand). The ethanol-assisted solvothermal conditions were controlled by heat treatment at 200°C for 2–6 h. Finally, yellow precipitate was obtained and then it was separated by a centrifuge (Labquip Centurion 1000 series, England) at 3000 rpm for 10 minutes, washed with deionized water three times and dried in an oven (Hotbox Oven Size 2, Gallenkamp, UK) at 100°C for 24 h.

Characterization

The crystalline phase of $BiVO_4$ was determined by X-ray diffractometer (XRD, JEOL, JDX-3530, Japan) using CuK_α radiation ($\lambda = 0.15418$ nm), and the monoclinic and tetragonal structure were confirmed by comparing JCPDS file no. 14–0688 and 14-0133, respectively. Morphologies of $BiVO_4$ were investigated by field emission scanning electron microscope (FE-SEM, JEOL JSM-6335F, Japan) at a voltage of 15 kV. $BiVO_4$ powder was dispersed in absolute ethanol, sonicated for 15 min and dropped onto a stub. After drying in a desiccator, it was coated with a gold coater (SPI sputter coater, USA) using standard method. Surface area of the particles were measured by nitrogen absorption and calculated by Brunauer-Emmett-Teller (BET) method (Autosorb 1 MP, Quantachrome, USA). Absorption spectrum was recorded by UV-vis absorption spectrometer (Shimadzu 2600, Japan). Then, band gap energy (E_g) was calculated by a plot of $[F(R)E]^2$ versus absorbed light energy (E) from the Kubelka-Munk equation. Oxidation state and bonding distance between vanadium and oxygen atoms were studied by X-ray absorption spectroscopy (XAS) technique at the SUT-NANOTEC-SLRI XAS beamline (BL. 5.2), Synchrotron Light Research Institute (SLRI, Nakhon Ratchasima, Thailand). XAS measurements were collected at V K-edge energy (5465 eV) in transmission mode. The measured XAS data were analyzed using Athena software as implement in the IFEFFIT package [19, 20].

Results and discussion

X-ray diffraction peaks of $BiVO_4$ synthesized *via* ethanol-assisted solvothermal method were compared with the Joint Committee on Powder Diffraction Standards (JCPDS) file No. 14-0688 (monoclinic structure) as shown in Fig. 1. All diffraction patterns of different reaction times were in agreement with the standard monoclinic scheelite structure and no impurities were detected. The percentage volume of monoclinic phase in Table 1 was calculated according to $V_{monoclinic} = I_{[121]}/(I_{[121]} + I_{[200]})$ where $I_{[121]}$ is the highest intensity of monoclinic peak (at [121] plane) and

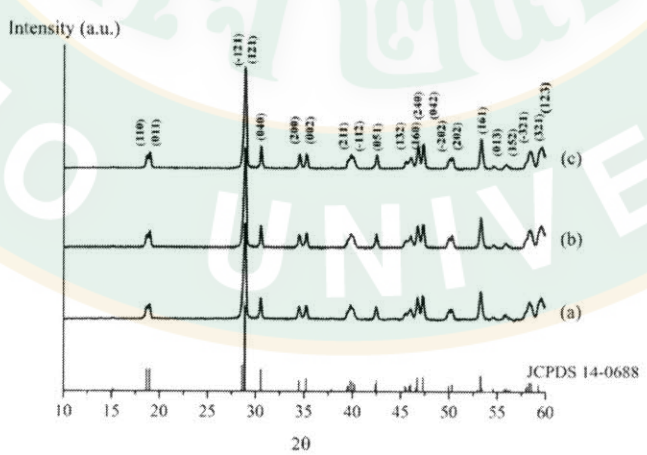

Figure 1. XRD patterns of $BiVO_4$ synthesized *via* solvothermal method at 200°C for (a) 2, (b) 4 and (c) 6 h.

Table 1. Physical properties of $BiVO_4$ synthesized *via* solvothermal method at 200°C for 2–6 h.

Time(h)	Monoclinic phase volume(%)	Crystalline size (nm)	Surface area (m^2/g)	Band gap energy (eV)
2	100	24	8.79	2.60
4	100	25	9.80	2.58
6	100	25	7.74	2.58

$I_{[200]}$ is the highest intensity of tetragonal pattern (peak at [200] plane). The peaks at [110], [011] and [200], [002] were clearly separated after a prolonged reaction time. These results suggested that the crystallinities had improved [21].

Average crystalline sizes (D) of the obtained bismuth vanadate powders were calculated using the Scherrer equation:

$$D = \frac{K\lambda}{\beta\cos\theta} \tag{1}$$

where λ is the wavelength of the X-ray radiation (0.154 nm), K is taken as 0.89, β is a peak at half-maximum intensity of the peak at $2\theta = 28.8$. $BiVO_4$ crystalline sizes were slightly increased from 24–25 nm after prolongation of time as shown in Table 1. In addition, obtained $BiVO_4$ crystal was compared to other methods and showed smaller in size than the $BiVO_4$ synthesized by the solid state method (>100 nm), the coprecipitation method (32 nm) [22] and the surfactant-assisted (polyvinyl pyrrolidone, PVPK30) hydrothermal method (34 nm) [23]. Conversely, it was found that $BiVO_4$ prepared by the diethylene glycal-assisted hydrothermal method resulted in a similar crystalline size (23.6 nm) [24].

SEM images of $BiVO_4$ in Fig. 2 illustrate that particle sizes were increased as reaction times increased. At 200°C for 2 h, agglomerated ellipse shapes were formed with a large range of particle size distribution between 100–500 nm. As heat treatment times increased to 4 h, particle size also increased with a narrow size distribution and their grains became clearer. Longer reaction times, larger in width and length were detected. The SEM results related to surface area results calculated by BET as summarized in Table 1. It was found that the surface areas of $BiVO_4$ synthesized under ethanol-assisted solvothermal for 2, 4 and 6 h were 8.79, 9.80 and 7.74 m^2/g, respectively. Compared to previous reports of $BiVO_4$ synthesized via ethanol-hydrothermal strategy [17], this method improved the surface area in shorter reaction times and without adding surfactant.

Electronic structure of $BiVO_4$ were also studied by UV-vis diffuse reflectance spectroscopy. The band gap energy (E_g) was evaluated using the modified Kubelka-Munk method [25] as the following equation:

$$F(R) = \frac{(1-R)^2}{2R} \tag{2}$$

where R is the reflectance, F(R) is function of reflectance which is proportional to absorbance coefficient (α).

Absorption spectra of $BiVO_4$ in Fig. 3 were assigned to the monoclinic structures as the absorption edge found in the visible region [26]. E_g was evaluated by this

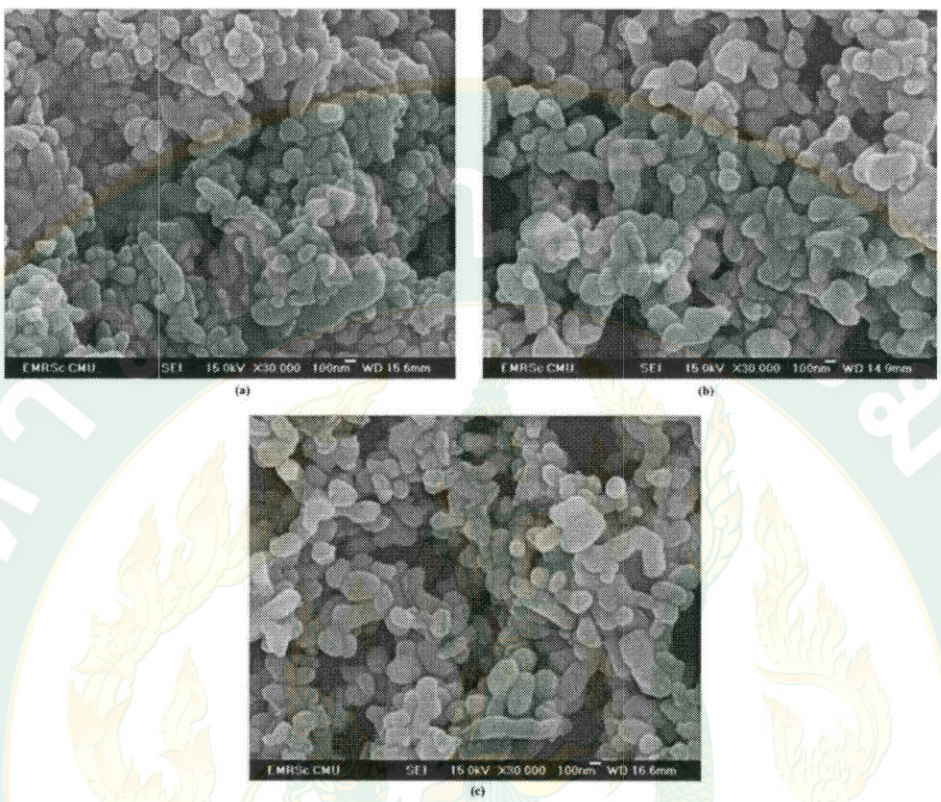

Figure 2. FE-SEM images of $BiVO_4$ synthesized *via* solvothermal method at 200°C for (a) 2, (b) 4 and (c) 6 h.

equation:

$$F(R)E = A(E - Eg)^n \quad (3)$$

where A is a constant and E is the photon energy (eV); $E = 1240/\lambda$ (λ = wavelength in nm unit). In the case of $BiVO_4$, $n = 1/2$ for direct band gap transition so that $(F(R)E)^2$ versus E was plotted as shown in Fig. 4. Band-gap energies of the $BiVO_4$ were 2.58–2.60 eV larger than in theory (2.4–2.5 eV) [27] and the longer heat treatment process reduced the band gap.

Moreover, the oxidation state of vanadium and the bond length between vanadium atoms and oxygen atoms (V–O) were determined by XAS. X-ray absorption near-edge structure (XANES) spectra of $BiVO_4$ were compared with vanadium oxide standards and shown in Fig. 5. It was obvious that the pre-edge decreased with time. Nevertheless, the edges overlapped each other near V_2O_5 (V^{+5}) indicating that the oxidation states of vanadium in $BiVO_4$ structures were reduced from 5+ to 4+ [28]. In addition, it was reported that co-presence of V^{5+} and V^{4+} in $BiVO_4$ structures with a high molar ratio of V^{4+}/V^{5+} led to high oxygen vacancies that enhanced photocatalytic performance [17]. The V–O bond distance was examined as the first shell distance from the vanadium atoms in terms of R-space. Fig. 6 showed extended X-ray absorption fine structure (EXAFS) spectra that lengthening

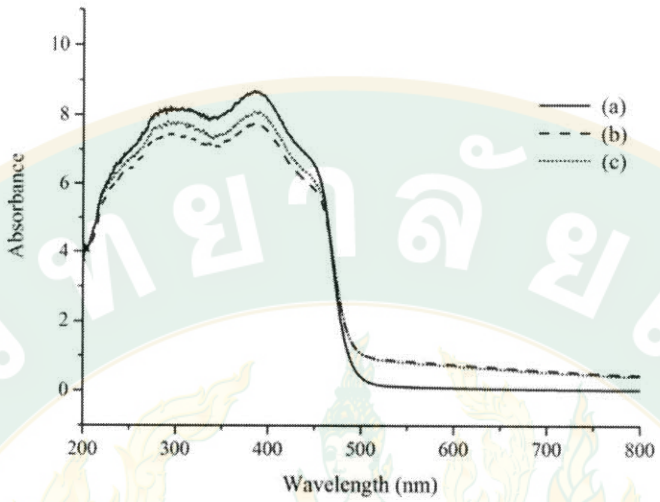

Figure 3. Absorption spectra of $BiVO_4$ synthesized *via* solvothermal method at 200°C for (a) 2, (b) 4 and (c) 6 h.

of the V–O bond distance occurred from 1.24 to 1.38 Å after prolongation of time from 2 to 6 h, respectively. This may be due to an influence of the Bi atom because the Bi–O bond distance was changed.

It is noted that no phase shift was applied to the $\chi(R)$ functions, thus the peak position of $\chi(R)$ functions will shift from the actual value by approximately 0.2 – 0.3 Å. Additionally, previous reports showed that the V–O bond lengths of the monoclinic $BiVO_4$ structures from the experimental value were 1.692 and 1.767 Å as well as from theoretical calculation using the density functional theory (DFT), which were 1.718 and 1.769 Å [29]. Therefore, the V–O bond lengths obtained from $BiVO_4$ powders resembled the previous reports.

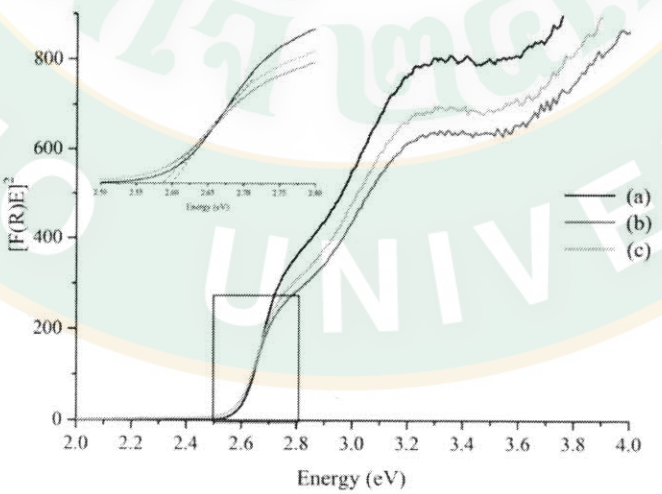

Figure 4. Plot of $[F(R)E]^2$ versus E of $BiVO_4$ synthesized *via* solvothermal method at 200°C for (a) 2, (b) 4 and (c) 6 h.

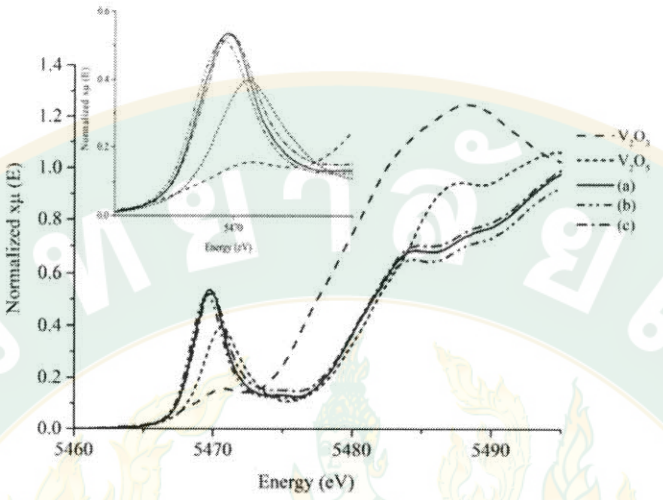

Figure 5. Normalized V K-edge XANES spectra of $BiVO_4$ synthesized *via* solvothermal method at 200°C for (a) 2, (b) 4 and (c) 6 h.

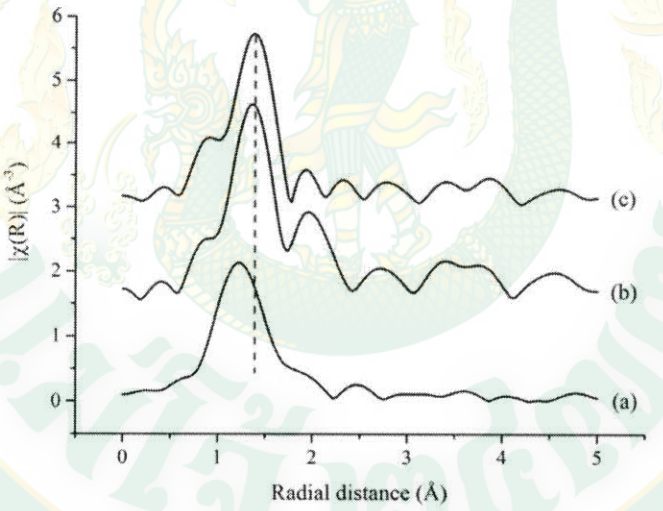

Figure 6. Normalized V K-edge EXAFS spectra of $BiVO_4$ synthesized *via* solvothermal method at 200°C for (a) 2, (b) 4 and (c) 6 h.

Conclusions

In conclusion, the monoclinic structure $BiVO_4$ was successfully synthesized *via* ethanol-assisted solvothermal method. Characterization results confirmed that crystalline phases, physical properties and bond distance between vanadium and oxygen were influenced by reaction times. Moreover, crystalline sizes and surface areas of $BiVO_4$ were improved by our synthesizing method with shorter reaction times without surfactant assist and calcination process. Therefore, obtained $BiVO_4$ is a candidate for application in photocatalysis under visible light in water purification and energy production.

Acknowledgments

The authors would like to express our appreciation to the Science Achievement Scholarship of Thailand (SAST), the Office of Agricultural Research and Extension of Maejo University and the National Research Council of Thailand (NRCT) for financial scholarship, the Science Lab Centre, Faculty of Science, Naresuan University for X-ray diffractometer (XRD) providing, the Science and Technology Service Center (STSC), Chiang Mai University for field emission scanning electron microscope (FE-SEM) assistant, Assoc. Prof. Dr. Siwaporn Meejoo Smith, Department of Chemistry, Faculty of Science, Mahidol University, Bangkok, Thailand for UV-vis diffuse reflectance spectroscopy (UV-vis DRS) and the SUT-NANOTEC-SLRI XAS beamline (BL5.2) at the Synchrotron Light Research Institute, Nakhon Ratchasima, Thailand for XAS measurement.

References

1. K. Shantha, and K. B. Varma Characterization of fine-grained bismuth vanadate ceramics obtained using nanosized powders. *J Am Ceram Soc.* **83**(5), 1122 (2000).
2. R. Munprom, P. A. Salvador, and G. S. Rohrer Polar Domains at the Surface of Centrosymmetric $BiVO_4$. *Chem Mater.* **26**(9), 2774 (2014).
3. Y. Tae Ho, C. Sung Ho, S. Kyu Jeong, and J. Min Su The domain structure of ferroelastic $BiVO_4$ studied by magnetic resonances. *J. Phys.: Condens. Matter.* **6**(2), 383 (1994).
4. S. Dong, J. Feng, Y. Li, L. Hu, M. Liu, Y. Wang, Y. Pi, J. Sun, and J. Sun Shape-controlled synthesis of $BiVO_4$ hierarchical structures with unique natural-sunlight-driven photocatalytic activity. *Appl Catal B.* 152–153 413 (2014).
5. P. Wood, and F. P. Glasser Preparation and properties of pigmentary grade $BiVO_4$ precipitated from aqueous solution. *Ceram Int.* **30**(6), 875 (2004).
6. L. Chen, E. Alarcón-Lladó, M. Hettick, I. D. Sharp, Y. Lin, A. Javey, and J. W. Ager Reactive sputtering of bismuth vanadate photoanodes for solar water splitting. *J Phys Chem C.* **117**(42), 21635 (2013).
7. H. Fan, T. Jiang, H. Li, D. Wang, L. Wang, J. Zhai, D. He, P. Wang, and T. Xie Effect of $BiVO_4$ crystalline phases on the photoinduced carriers behavior and photocatalytic activity. *J Phys Chem C.* **116**(3), 2425 (2012).
8. A. K. Bhattacharya, K. K. Mallick, and A. Hartridge Phase transition in $BiVO_4$. *Mater Lett.* **30**(1), 7 (1997).
9. A. Kudo, K. Omori, and H. Kato A novel aqueous process for preparation of crystal form-controlled and highly crystalline $BiVO_4$ powder from layered vanadates at room temperature and its photocatalytic and photophysical properties. *J Am Chem Soc.* **121**(49), 11459 (1999).
10. R. Venkatesan, S. Velumani, and A. Kassiba Mechanochemical synthesis of nanostructured $BiVO_4$ and investigations of related features. *Mater Chem Phys.* **135**(2), 842 (2012).
11. C. Ravidhas, A. Juliat Josephine, P. Sudhagar, A. Devadoss, C. Terashima, K. Nakata, A. Fujishima, A. Moses Ezhil Raj, and C. Sanjeeviraja Facile synthesis of nanostructured monoclinic bismuth vanadate by a co-precipitation method: Structural, optical and photocatalytic properties. *Mat Sci Semicon Proc.* **30**, 343 (2015).
12. L. Zhang, J. Long, W. Pan, S. Zhou, J. Zhu, Y. Zhao, X. Wang, and G. Cao Efficient removal of methylene blue over composite-phase $BiVO_4$ fabricated by hydrothermal control synthesis. *Mater Chem Phys.* **136**(2–3), 897 (2012).
13. Y. Ma, H. Jiang, X. Zhang, J. Xing, and Y. Guan Synthesis of hierarchical m-$BiVO_4$ particles via hydro-solvothermal method and their photocatalytic properties. *Ceram Int.* **40**, 16485 (2014).

14. A. Zhang, and J. Zhang Hydrothermal processing for obtaining of $BiVO_4$ nanoparticles. *Mater Lett.* **63**(22), 1939 (2009).
15. X. Wang, G. Li, J. Ding, H. Peng, and K. Chen Facile synthesis and photocatalytic activity of monoclinic $BiVO_4$ micro/nanostructures with controllable morphologies. *Mater Res Bull.* **47**(11), 3814 (2012).
16. X. Zhang, Z. Ai, F. Jia, L. Zhang, X. Fan, and Z. Zou Selective synthesis and visible-light photocatalytic activities of $BiVO_4$ with different crystalline phases. *Mater Chem Phys.* **103**(1), 162 (2007).
17. H. Jiang, H. Dai, X. Meng, L. Zhang, J. Deng, and K. Ji Morphology-dependent photocatalytic performance of monoclinic $BiVO_4$ for methyl orange degradation under visible-light irradiation. *Chinese J Catal.* **32**(6–8), 939 (2011).
18. R. Lu, M. Lili, J. Lei, W. Jian-Bo, Q. Mingqiang, and Y. Ying Template-free synthesis of $BiVO_4$ nanostructures: II. Relationship between various microstructures for monoclinic $BiVO_4$ and their photocatalytic activity for the degradation of rhodamine B under visible light. *Nanotechnology.* **20**(40), 405602 (2009).
19. M. Newville IFEFFIT : interactive XAFS analysis and FEFF fitting. *J. Synchrotron Radiat.* **8**(2), 322 (2001).
20. B. Ravel, and M. Newville ATHENA, ARTEMIS, HEPHAESTUS: data analysis for X-ray absorption spectroscopy using IFEFFIT. *J. Synchrotron Radiat.* **12**(4), 537 (2005).
21. R. Venkatesan, S. Velumani, and A. Kassiba Mechanochemical synthesis of nanostructured $BiVO_4$ and investigations of related features. *Mater Chem Phys.* **135**(2–3), 842 (2012).
22. J. Yu, Y. Zhang, and A. Kudo Synthesis and photocatalytic performances of $BiVO_4$ by ammonia co-precipitation process. *J Solid State Chem.* **182**(2), 223 (2009).
23. H. Fan, D. Wang, L. Wang, H. Li, P. Wang, T. Jiang, and T. Xie Hydrothermal synthesis and photoelectric properties of $BiVO_4$ with different morphologies: An efficient visible-light photocatalyst. *Appl Surf Sci.* **257**(17), 7758 (2011).
24. B. X. Lei, L. L. Zeng, P. Zhang, Z. F. Sun, W. Sun, and X. X. Zhang Hydrothermal synthesis and photocatalytic properties of visible-light induced $BiVO_4$ with different morphologies. *Adv Powder Technol.* **25**(3), 946 (2014).
25. R. López, and R. Gómez Band-gap energy estimation from diffuse reflectance measurements on sol–gel and commercial TiO_2: a comparative study. *J Sol-Gel Sci Techn.* **61**(1), 1 (2012).
26. S. Tokunaga, H. Kato, and A. Kudo Selective preparation of monoclinic and tetragonal $BiVO_4$ with scheelite structure and their photocatalytic properties. *Chem Mater.* **13**(12), 4624 (2001).
27. J. K. Cooper, S. Gul, F. M. Toma, L. Chen, P-A. Glans, J. Guo, J. W. Ager, J. Yano, and I. D. Sharp Electronic structure of monoclinic $BiVO_4$. *Chem Mater.* **26**(18), 5365 (2014).
28. Z. Zhai, A. B. Getsoian, and A. T. Bell The kinetics of selective oxidation of propene on bismuth vanadium molybdenum oxide catalysts. *J Catal.* **308**, 25 (2013).
29. K. Ding, B. Chen, Z. Fang, and Y. Zhang Density functional theory study on the electronic and optical properties of three crystalline phases of $BiVO_4$. *Theor Chem Acc.* **132**(5), 1 (2013).

Journal of Environmental Chemical Engineering xxx (2018) xxx-xxx

Contents lists available at ScienceDirect

Journal of Environmental Chemical Engineering

journal homepage: www.elsevier.com

Hydrothermal synthesis and photocatalytic activities of stabilized bismuth vanadate/bismuth tungstate composites

Pradudnet Ketwong[a, *], Mai Takashima[b, c], Akio Nitta[b], Pusit Pookmanee[a], Bunsho Ohtani[b, c]

[a] Department of Chemistry, Faculty of Science, Maejo University, Chiang Mai, 50290, Thailand
[b] Graduate School of Environmental Science, Hokkaido University, Sapporo, 060-0810, Japan
[c] Institute for Catalysis, Hokkaido University, Sapporo, 001-0021, Japan

ARTICLE INFO

Keywords:
Bismuth vanadate/bismuth tungstate
Photocatalyst
Stabilization
Photoacoustic spectroscopy

ABSTRACT

Bismuth vanadate/bismuth tungstate (BVO/BWO) composites in various BVO fractions (f(V)) were synthesized through hydrothermal reaction. Morphology analysis of the composites showed that rod-like BVO structures were partially deposited on flake-ball (FB) BWO particles. In addition, surface structures of BWO, BVO and BVO/BWO were studied in energy-resolved distribution of electron traps and conduction band-bottom (CBB) position by household reversed double-beam photoacoustic spectroscopy (PAS) and single-beam PAS, respectively. Apparent CBB of BVO/BWO was ca. 0.4 eV anodically shifted from BWO and almost similar to BVO. Moreover, photocatalytic oxygen liberation under irradiation of by UV–vis and visible lights demonstrated that photocatalytic activities of the BVO/BWO composites were depended on f(V) and calcined BVO/BWO composites in which BVO was stabilized on BWO showed enhancement of photocatalytic activity comparing to a pristine BVO. The prolonged and the highest active photocatalyst under visible light was calcined 0.80f(V) due to BVO stabilization on FB-BWO particles.

1. Introduction

Photocatalysts used for solar photocatalysis, which is a photochemical reaction, have been developed for environmental treatment applications and energy production [1–4]. A famous stable metal oxide, titanium(IV) oxide (TiO_2) was reported as a high photocatalytic-performance photocatalyst under ultraviolet (UV) light irradiation [5]. However, pristine TiO_2 cannot absorb sun light effectively due to large band gap energy of 3.2 eV (absorb only 5% of sun light). Therefore, visible light-active photocatalysts become more attractive for the solar photocatalysis.

In recent years, bismuth-based oxides were reported as visible light-active photocatalysts owing to the interaction between Bi (6s) and O (2p) making band-gap energy small corresponding to visible light region [6–8]. Monoclinic bismuth vanadate ($BiVO_4$, BVO) with narrow band gap energy of 2.4 eV and high visible-light absorption is a good candidate and has been developed for the more effective visible- light photocatalyst since there are some disadvantages such as slow charge transportation, rapid electron-hole recombination rate and photocorrosion [7–12]. Coupling BVO with appropriate band structure metal oxides (FeOOH/BVO [13], TiO_2/BVO [14] and BVO/BiOCl [15]) is an effective strategy to enhance photocatalytic activity and long-life reaction of the BVO. Similarly, bismuth tungstate (Bi_2WO_6, BWO) is another suitable support with a unique morphology and band-gap energy of 2.8 eV [16]. It was reported that photocatalytic activity of BWO for oxygen liberation under visible light ($\lambda > 420$ nm) [16,17] and the photocatalytic activity was increased by increasing specific surface area and reducing lattice defect density [16]. Bismuth vanadate/bismuth tungstate ($BiVO_4$/Bi_2WO_6, BVO/BWO) heterojunction was firstly reported to show an improvement of decomposition of phenol under visible light over the individual components [18]. Furthermore, fraction of BVO content in composites (f(V)) played an important role in photocatalytic activity and the sample of f(V) = 1 showed the best activity in photodegradation of methylene blue [19], photocatalytic degradation of Rhodamine B (RhB) [20] and photocatalytic antifouling activity [21]. Two-step process (hydrothermal and calcination) was applied to obtain uniform morphology and better crystallinity of the BVO/BWO

* Corresponding author.
Email addresses: pradudnet@gmail.com (P. Ketwong); takashima.m@cat.hokudai.ac.jp (M. Takashima); nitta-salut-akio@cat.hokudai.ac.jp (A. Nitta); pusit@mju.ac.th (P. Pookmanee); ohtani@cat.hokudai.ac.jp (B. Ohtani)

https://doi.org/10.1016/j.jece.2018.01.062
Received 24 August 2017; Received in revised form 1 December 2017; Accepted 25 January 2018
Available online xxx
2213-3437/

composite leading to superior visible-light absorption and higher photodegradation activity for RhB [22]. Moreover, forming of BVO/BWO heterojunction facilitated electron-hole separation and charge transfer, which promoted photocatalytic activity [23,24].

Herein, we synthesized BVO/BWO composites in various (f(V)) and firstly report the results of photocatalytic oxygen liberation. The results of energy-resolved distribution of electron traps (ERDT) and conduction band positions of BWO, BVO and BVO/BWO composite were also for the first time analyzed and discussed. In addition, we found that BVO could be stabilized by loading on BWO and calcination at 873 K for 4 h was an important step to make better connection between BVO and BWO particles. In case of calcination, photocatalytic activity was enhanced by adding BWO into the composite and it was depended on BVO fraction.

2. Experimental

2.1. Sample preparation

2.1.1. Synthesis of BVO

BVO was synthesized by using 1.0 mmol bismuth(III) nitrate pentahydrate ($Bi(NO_3)_3{\cdot}5H_2O$, 99.9%, Wako Pure Chemical) dissolved in 2-mol L^{-1} nitric acid (60%, Wako Pure Chemical) and 1.0 mmol ammonium metavanadate (NH_4VO_3, 99.0%, Wako Pure Chemical) dissolved in 5-mol L^{-1} aqueous ammonia (25%, Wako Pure Chemical) as starting materials. The vanadate solution was added dropwise to the bismuth solution and then the mixture was stirred. The pH of the mixture was adjusted to 7 by 2-mol L^{-1} nitric acid to obtain a bright yellow suspension. Then, 10 mL of ethanol (99.5%; Wako Pure Chemical) was added to obtain a feed suspension. After stirred for 60 min, the feed suspension was poured in a Teflon (PTFE) bottle in a stainless-steel outer bottle (San-ai Science HUT-100), heated at 473 K for 2 h in an oven and left to be cooled down to ambient temperature. The precipitate was collected by centrifugation at 3000 rpm, washed by Milli-Q water several times and dried at 393 K in an oven. The resultant yellow product, BVO, was calcined, if needed, at 873 K in air for 4 h (c-BVO).

2.1.2. Synthesis of BVO/BWO composites

Firstly, flake ball-shaped (FB) BWO particles were synthesized by hydrothermal reaction of an aqueous suspension containing bismuth(III) hydroxide and tungstic acid at 433 K for 20 h according to previous papers [25,26]. Then, BWO was added into a BVO feed suspension (see *2.1.1*). The resultant suspension was vigorously stirred for 60 min and underwent hydrothermal reaction under the same conditions as those for the BVO preparation to obtain a BVO/BWO composite. It was continuously stirred for 15 min before heat treatment at 473 K for 2 h. Molar fraction of BVO (f(V)) was controlled by changing the ratio of the feed BVO and BWO to be 0.50 (BVO/BWO_0.50), 0.67 (BVO/BWO_0.67), 0.80 (BVO/BWO_0.80) or 0.91 (BVO/BWO_0.91). For calcined samples at 873 K in air for 4 h, "c-" was put before their names; e.g. 'c-BVO/BWO_0.50'.

2.2. Characterization of samples

Surface morphologies of obtained powders were observed by a field-emission scanning electron microscope (FE-SEM, JSM-7400F, JEOL) in secondary-electron image (SEI) mode and scanning transmission electron microscopy (STEM, HD2000 ultrathin film evaluation system, Hitachi). The FE-SEM was operated at 5.0 kV electron-acceleration voltage, 10.0 μA current and 5–6 mm working distance. Dried sample powder was placed onto a carbon tape (Okenshoji #15-1096) stuck on a specimen stub (12 mm in diameter; 10 mm in height). In case of STEM, sample powders were dispersed in methanol and sonicated in an ultrasound bath for a few seconds. Then suspension was dropped and deposited on carbon covered cupper microgrid (NS-C15, Okenshoji). The images were observed using 3 mm working distance, 200 kV accelerating voltage and 20 μA emission current. Crystalline structures were analyzed by an X-ray diffractometer (XRD, SmartLab, Rigaku, Japan) with Cu K_α radiation (40 kV, 30 mA, 0.154 nm). XRD analysis was performed at scanning rate of 1.0° min^{-1} and steps of 0.01° in the 2θ range of 10–80°. Crystalline phases of BVO and BWO were compared with Joint Committee on Powder Diffraction Standards (JCPDS) file No. 14-0688 and 79-2381, respectively. Primary particle size (or crystallite size) was evaluated by corrected width of the most intensive XRD peak of each crystalline phase (121) for BVO and (131) for BWO using Scherrer equation [27,28]. Band gap energy was calculated by Kubelka-Munk (K-M) function analyzed by UV–vis diffuse reflectance spectrometer (UV-vis DRS, V670, Jasco). Barium sulfate was used as a white reflectance standard. Specific surface area (SSA) was estimated based on nitrogen adsorption measurement at 77 K (NOVA 1200e surface-area and pore-size analyzer, Quantachrome (previously Yuasa Ionics)) and calculated by Brunauer–Emmett–Teller (BET) method. A sample powder was pre-heated under nitrogen atmosphere at 423 K for 90 min before analysis. Energy-resolved density of electron traps (ERDT) and conduction band-bottom position (CBB) were measured by reversed double-beam photoacoustic spectroscopy (RDB-PAS) and single-beam PAS, respectively, using laboratory-made RDB-PAS apparatus [29].

2.3. Photocatalytic activity test

Photocatalytic activities of the samples were evaluated by the rate of oxygen liberation. A photocatalyst (50 mg) was suspended in an aqueous solution of iron(III) chloride (5.0 mL; 0.25 mmol) in a glass tube. After sonicated for 15 min, argon bubbling was applied for 15 min to purge off air and the suspension was photoirradiated by UV–vis light (a 400-W high-pressure mercury arc) or visible-light (a 300-W xenon arc with a Y44 cut-off glass filter (Hoya, Japan) transmitting light of wavelength > ca. 420 nm) in a thermostatic bath (298 K). The amount of liberated oxygen in the gas phase of a glass tube was measured by a TCD-gas chromatograph (GC, GC-8A, Shimadzu, Japan) with a molecular sieve 5A column to calculate the rate of oxygen liberation. Since contamination of air could not be excluded thoroughly, the amount of evolved oxygen was calibrated with amount of nitrogen calculated by the chromatograms on the assumption that air, as a mixture of nitrogen and oxygen, was contaminated in the samples tubes and the molar amount of corresponding contaminated oxygen can be calculated by that of nitrogen.

Reusability of BVO, BVO/BWO_0.80, c-BVO and c-BVO/BWO_0.80 photocatalysts was tested in the same condition under visible light for 5 cycles. After the visible-light irradiation for 30 min in every cycle, generated oxygen gas was removed by argon-gas bubbling for 15 min. The next cycle was started under visible-light irradiation and 0.20 mL of gas was sampled every 10 min until reached 30 min. Amount of produced oxygen was analyzed by TCD-GC.

3. Results and discussion

3.1. Morphologies of BVO, BWO and BVO/BWO composites

The morphology of synthesized BVO was small rod-like particles of ca. 100 nm in width and ca. 200 nm in length as shown in Fig. 1(a), and they were agglomerated and densified by calcination to produce larger particles with grain boundaries (Fig. 1(b)). In addition, hydrothermally synthesized FB-BWO was analysed by SEM images as shown in Fig. 1(c). All the BWO particles were assemblies of flakes

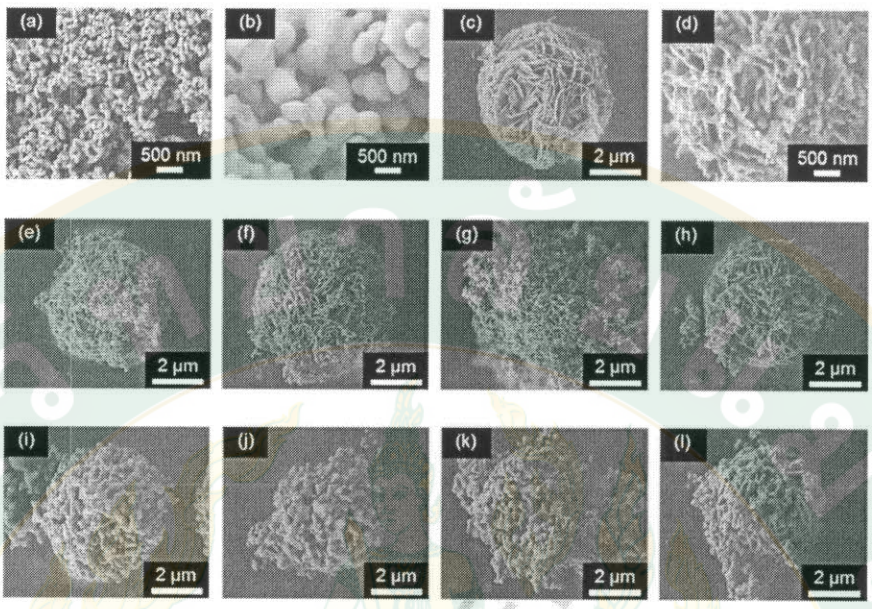

Fig. 1. FE-SEM images of (a) BVO, (b) c-BVO, (c) BWO, (d) c-BWO, (e)–(h) BVO/BWO composites and (i)–(l) c-BVO/BWO composites with $f(V)$ = 0.50, 0.67, 0.80 and 0.91, respectively.

with their outer diameter of ca. 5 μm as has been reported previously [26]. The particle size was decreased by ca. 10–20% by calcination at 873 K for 4 h (Fig. 1(d)) presumably due to shrinkage and fusion of flakes.

On the other hand, BVO/BWO showed different results when calcined. Figs. 1(e)–(h) show morphologies of BVO/BWO with $f(V)$ of 0.50, 0.67, 0.80 and 0.91, respectively, before calcination. As expected based on the preparation process, it seems that small BVO particles were partially deposited on and between flakes in FB-BWO particles. It was also noticed that although $f(V)$ was increased, morphologies of the composites were similar while BVO/BWO_0.80 particle was much more covered by rod-like BVO particles than other composites. Moreover, from the surface observation of the BVO/BWO_0.80 particles observed by STEM, it was confirmed that rod particles were deposited on flakes as shown in Fig. 2(a). On the other hand, by the 873-K calcination (Fig. 1(i)–(l)), the deposited small BVO particles were interconnected and grown larger. The same phenomenon could also be observed by STEM as shown in Fig. 2(b). The surface of c-BVO/BWO_0.80 composite was composed of BVO with smooth surface and various particles sizes, but not formed by large sintered particles as seen for c-BVO in Fig. 1(b). In other word, BVO particles were stabilized on FB-BWO particles against heat-induced sintering.

3.2. Crystalline structures of BVO, BWO and BVO/BWO composites

Crystalline phase structures of all samples were analyzed by XRD and shown in Fig. 3. XRD patterns of BWO (Fig. 3A(a)) and BVO (Fig. 3A(f)) were defined as orthorhombic and monoclinic structure, respectively, without any impurity peaks. Consequently, BVO/BWO composites were composed of monoclinic phase of BVO and orthorhombic phase of BWO peak intensities of which were related to BVO/BWO mole ratio as shown in Fig. 3A(b)–(e). Crystalline phases did not change even after calcination at 873 K for 4 h as showed in Fig. 3B. Diffraction patterns of calcined composites remained in the combination of the monoclinic and orthorhombic structures. However, marked increase in the peak intensities indicated improvement of the crystallinities of all samples and increase in the crystalline sizes indicated crystalline growth by calcination. All characteristics of the samples synthesized in this work were summarized in Table 1.

3.3. Photoabsorption properties of BVO, BWO and BVO/BWO composites

Fig. 4 shows diffuse reflectance spectra of uncalcined (Fig. 4A) and calcined (Fig. 4B) samples. It was found that all samples absorbed light in UV and visible region while BVO and BVO/BWO composites had wider light absorption in the visible region than BWO. Moreover, band gap energy (E_g) was evaluated by following equation:

$$F(R)E = A(E - E_g)^n \quad (1)$$

where A is a constant, E is the photon energy (eV); $E = 1240/\lambda$ (λ = wavelength in nm unit), n = 1/2 (in the case of BVO) and 2 (in the case of BWO), and E_g of the BVO and BWO were 2.53 and 2.65 eV, respectively. Moreover, E_g of composites were slightly wider (2.54 – 2.56 eV) than BVO, but they were not significantly affected by varying $f(V)$. As shown in Table 1, c-BVO and c-BVO/BWO were promised to be the most visible light-active photocatalysts due to narrow band-gap energies.

3.4. Surface structure of BVO, BWO and BVO/BWO composites

Fig. 5 shows ERDT and CBB position of samples plotted as a function of energy (eV) from the top of valence band (VBT) of each sample. As has been reported previously [29], metal-oxide powders may have electron traps (ETs), localized electronic states accepting electrons, with their energies close to CBB, and those ETs are presumed to be located mainly on the surface of powders, i.e., ERDT reflects the surface structure of metal-oxide powders. For the samples used in the present study, ERDT/CBB patterns were observed similar to the other metal ox-

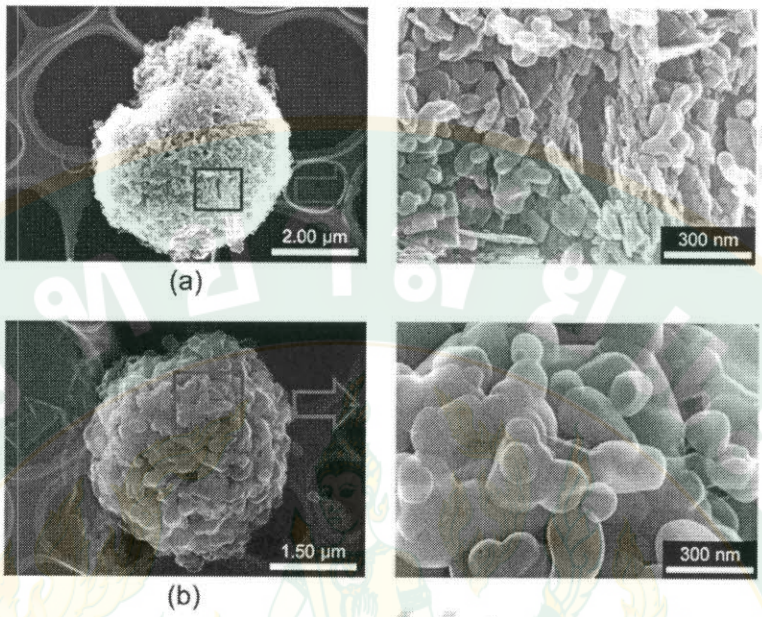

Fig. 2. STEM images of (a) BVO/BWO_0.80 and (b) c-BVO/BWO_0.80 composites.

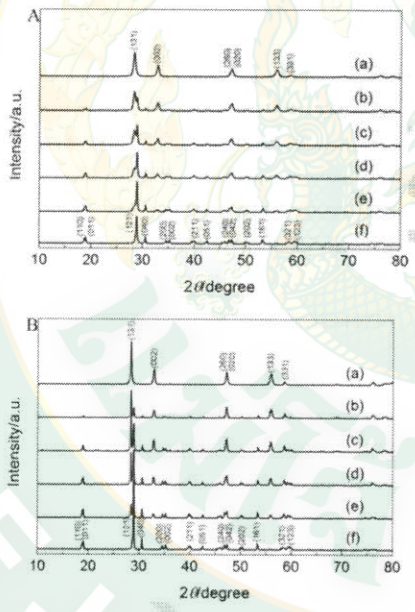

Fig. 3. X-ray diffraction patterns of (A) uncalcined and (B) calcined (a) BWO, (b)-(e) BVO/BWO composites with $f(V) = 0.50$, 0.67, 0.80 and 0.91, respectively, and (f) BVO.

ides. Being consistent with the results of band gaps measured by DRS as described above, apparent CBB, showing band gap energy with reference to VBT, of BWO was higher than that of BVO. The same as the other metal oxide particles, parts of ETs were located in the energy range close to or slightly above CBB for all samples (The reasons for presence of ETs in the conduction band has been discussed in the previous paper [29]).

Comparing ERDT patterns of BWO, BVO and BVO/BWO, the BVO/BWO pattern was found to be reproduced by summations of the ERDT patterns of BVO and BWO with ca. 0.4 eV anodic (downward) shift of the BWO pattern, on the assumption that ETs in BVO and BWO gave ERDT patterns independently. This suggests that apparent VBT of BWO is more anodic by ca. 0.4 eV than that of BVO and, as a result, apparent CBB of BVO and BWO are almost the same position, being consistent with previous reports [7,18,22,30]. Anyway, the fact that the ERDT pattern of composites could be reproduced only by summation of ERDT patterns of each component suggests negligible electron/positive hole transfer between two components [31], which have been often presumed for the other composite photocatalysts [32,33].

3.5. Photocatalytic activities

Fig. 6.1 and 6.2 show photocatalytic activities of BWO, BVO, BVO/BWO and their calcined samples in various $f(V)$ under UV–vis and visible-light irradiation, respectively. At the beginning of photocatalysis under UV–vis light irradiation (Fig. 6.1A), BVO and BWO showed the highest and lowest-level photocatalytic rate, 14 and 2 μmol h^{-1}, respectively. However, the activity of BVO was dropped down and became to be lower than that of BVO/BWO_0.91 after 1-h irradiation. Thus, BVO/BWO_0.91 sample exhibited the highest activity for prolonged reaction time to 1.5 h. In contrast, activity of c-BVO was lower than calcined composites and much decreased when compared to BVO (Fig. 6.1B). The highest activity among the calcined samples was observed for c-BVO/BWO_0.91. In the case of photocatalytic activities under visible-light irradiation, the similar results as in case of the under UV–vis irradiation were obtained, but c-BVO/BWO_0.80 showed the highest activity among the calcined samples (Fig. 6.2B), while BVO still kept higher activity after 1.5-h visible-light irradiation (Fig. 6.2A). It

Table 1
Physical properties and photocatalytic activities of uncalcined and calcined BWO, BVO and BVO/BWO composites under UV–vis and visible light.

Samples	f(V)	Uncalcined							Calcined				
		D^a/nm	E_g /eV	SSA^b/m^{2}g^{-1}	UV–vis		visible		D^a/nm	E_g/eV	SSA^b/m^{2}g^{-1}	UV–vis	
					Rate/μmol h^{-1}	R^2	Rate/μmol h^{-1}	R^2				Rate/μmol h^{-1}	R^2
BWO	0	16	2.65	19	1.91	0.9825	0.38	0.9440	29	2.65	4	2.71	0.9943
BVO/BWO	0.50	31	2.56	NA	8.64	0.9898	2.04	0.9734	47	2.49	NA	6.20	0.9908
	0.67	26	2.56	NA	10.45	0.9952	5.08	0.9525	60	2.50	NA	7.79	0.9880
	0.80	29	2.55	14	11.33	0.9932	4.82	0.9820	56	2.49	3	9.44	0.9909
	0.91	36	2.54	NA	12.77	0.9929	6.73	0.9790	58	2.51	NA	8.64	0.9865
BVO	1	42	2.53	12	14.01	0.9932	7.90	0.9910	62	2.47	1	4.62	0.9912

NA = Not analyzed

[a] Crystalline sizes (D) of BWO and BVO were calculated by (131) and (121) XRD peaks, respectively.

[b] Specific surface area.

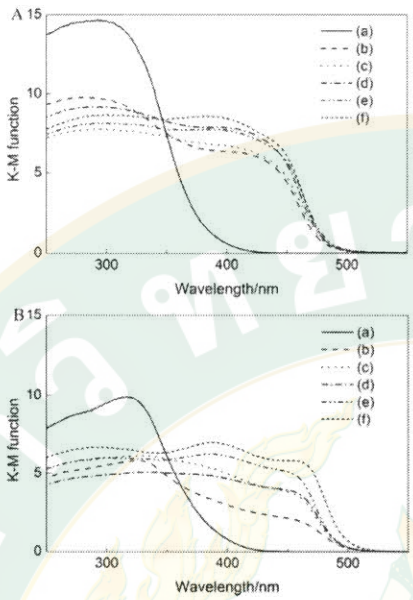

Fig. 4. KM spectra of (A) uncalcined and (B) calcined (a) BWO, (b)-(e) BVO/BWO composites with $f(V) = 0.50$, 0.67, 0.80 and 0.91, respectively, and (f) BVO.

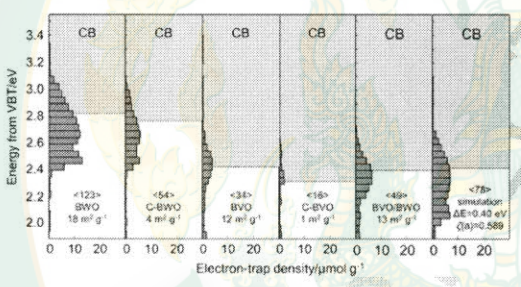

Fig. 5. ERDT patterns of BWO, c-BWO, BVO, c-BVO, BVO/BWO and c-BVO/BWO. Numbers in < > denote the total density of ETs in the unit of μmol g^{-1}. The last row is specific surface area in the unit of $m^2 g^{-1}$.

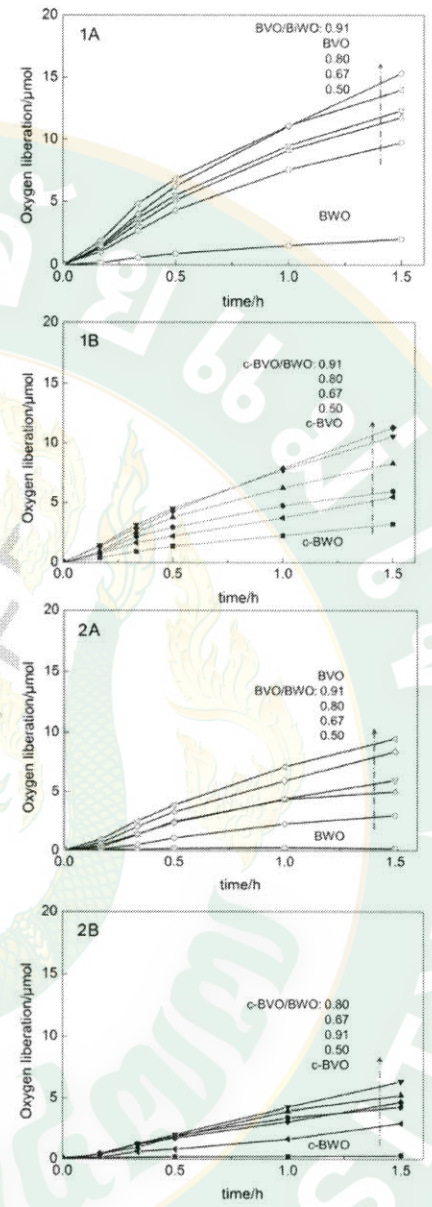

Fig. 6. 1 Photocatalytic oxygen liberations under UV–vis light using (A) uncalcined and (B) calcined BWO, BVO and BVO/BWO composites. 2 Photocatalytic oxygen liberations under visible light using (A) uncalcined and (B) calcined BWO, BVO and BVO/BWO composites.

seems strange, in the ordinary sense in the field of photocatalysis studies, that the c-BVO/BWO activities were higher than those of BVO/BWO though the SSA was a few times decreased by the calcination. However, as has been reported previously [34], photocatalytic activities of commercial titania samples for oxygen evolution in the presence of electron acceptors, but not ordinary organics decomposition reactions, were predominantly regulated by their secondary particle size (SPS) and the larger the SPS of samples were, the higher their photocatalytic activities became. This may be because the larger particle size is required to absorb multiple photons within the life time of an electron-positive hole pair to drive oxygen evolution with four-electron transfer process. The observed activity not so decreased by calcination of BVO/BWO composites ($f(V) < 0.8$) could be explained by the stabilization of loaded small BVO particles, not to be aggregated but keeping the high dispersion of BVO particles.

Fig. 7 is plots of 30-min rate of photocatalysis as a function of BVO content in composites, $f(V)$. Photocatalytic activities were obviously increased with increasing $f(V)$ for the uncalcined samples under both UV–vis and visible-light irradiations. For the calcined samples, on the other hand, the activities increased with increasing $f(V)$ to attain maximum at $f(V) = 0.8$ and then decreased to result in the relatively lower activity of c-BVO. In other words, both UV–vis and visible-light activi-

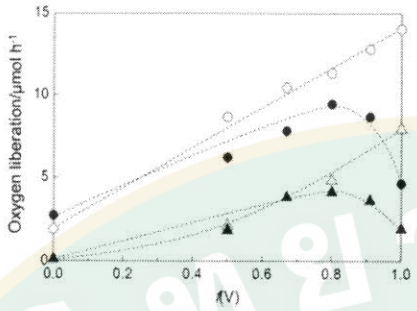

Fig. 7. Change in photocatalytic activities of BVO/BWO and c-BVO/BWO composites as a function of $f(V)$. Open and closed circles: uncalcined and calcined samples, respectively, under UV–vis irradiation. Open and closed triangles: uncalcined and calcined samples, respectively, under visible-light irradiation.

ties of BVO were largely decreased to be ca. 30% by calcination (c-BVO), while the activity of BVO/BWO composites, owing predominantly to vanadate component (Note the relatively lower activity of BWO and almost linearly increasing BVO activity with $f(V)$), was kept almost the same degree (or slightly decreased) even with calcination. It could be said that the photochemical reaction occurred mainly on BVO particles and tungsten components were negligibly active, but they helped to stabilize the BVO particles when they were calcined. In this sense, uncalcined pristine BVO was the best photocatalyst, but as shown in Fig. 8 and discussed in the following section, the stability of uncalcined BVO was worse than those of calcined samples.

The above-mentioned photocatalytic-activity trends can reasonably be interpreted by the change in morphology by calcination. As shown in Fig. 1 and 2, relatively smaller-sized BVO was fused and sintered to become larger-sized particles with possible grain boundaries, while no significant changes, by calcination, in morphology of BVO particles on BWO particles. Furthermore, these morphological changes could reflect ERDT/CBB patterns shown in Fig. 5. The total ET density of BVO (34 μmol g^{-1}) was reduced almost by half by calcination (16 μmol g^{-1}), though SSA was reduced to be less than 10% (Table 1). Taking into consideration that the partial density of shallower ETs located around CBB seemed to become less than half by calcination, the above-mentioned change in total density ETs suggests that deeper ETs might be increased by calcination presumably due to crystalline defects at the grain boundaries of c-BVO, as was claimed in a previous research [35]. Analysis of ERDT patterns of composites with various $f(V)$ and correlation between photocatalytic activities and ERDT/CBB patterns is another valuable target and further studies along this line as well as study on calculating absolute position of ERDT/CBB are now underway.

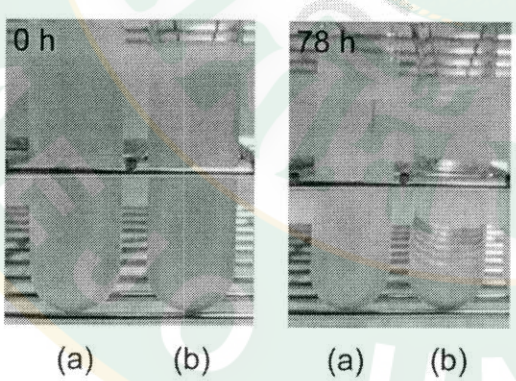

Fig. 8. Sedimentation images of (a) BVO and (b) c-BVO/BWO_0.80.

3.6. Sedimentation of BVO and BVO/BWO composites

Although BVO was the most active photocatalyst for oxygen liberation among the samples used in this study, c-BVO/BWO with a large overall particle size has potential for separating photocatalyst from reaction mixture after photoirradiation. Sedimentation test in Fig. 8 showed that the supernatant of a c-BVO/BWO_0.80 suspension was clear, but BVO powder was still stably dispersed in water even after 78-h standing. This is one of the advantages of c-BVO/BWO_0.80 for practical applications in the future.

3.7. Reusability

Long-life photocatalyst is an important property for practical applications. Reusability of c-BVO/BWO_0.80 composite was tested and compared to BVO, c-BVO and BVO/BWO_0.80 as showed in Fig. 9. In the first cycle, BVO showed the highest activity, however, rapid decreases of photocatalytic activity were presented in the second cycle for all the samples. After 2.5-h irradiation, the activities of BVO, c-BVO, BVO/BWO_0.80 and c-BVO/BWO_0.80 were reduced to 16%, 24%, 25% and 45% of the first cycle, respectively. It was illustrated that the c-BVO/BWO composite was more stable in visible light irradiation than the others.

4. Conclusion

On the basis of above-mentioned results and discussion, it is concluded that BVO and BWO components exhibit photocatalytic activity independently, i.e., without possible electron/positive hole transfer between two kinds of metal oxides since the photocatalytic activity for oxygen liberation changed linearly with changing BVO contents in uncalcined BVO/BWO composites. Another support for the independency of two components is that ERDT of the uncalcined composite can be reproduced by summation of the ERDT patterns of each component by assuming that VBT of BWO is lower (more anodic) by ca. 0.4 eV than that of BVO; if electron or positive-hole transfer happens between two components, the ERDT pattern of composites might not be a simple summation. The fact that the calcined composites showed the photocatalytic activity maximum at the BVO composition of 80% is attributable to the ability of BWO to keep the BVO activity after calcination by preventing the aggregation and fusion of the BVO crystallites into large, less active, particles. In general, relatively higher photocatalytic activity of composite materials compared with those of single components,

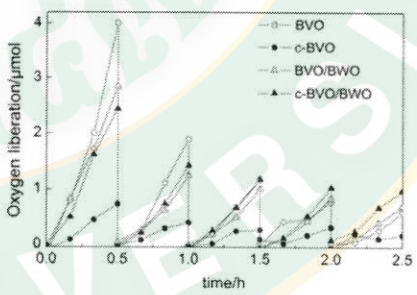

Fig. 9. Reusability of BVO, c-BVO, BVO/BWO_0.80 and c-BVO/BWO_0.80 composites.

often called "synergetic effect", has been attributed to the interparticle electron/positive-hole transfers without showing the experimental evidence for the charge transfer. For the c-BWO-BVO composite photocatalysts reported in this paper, the maximum activity was observed due to physically stabilized BVO particles by BWO in calcination rather than to possible charge transfer between two components. Thus, synergetic effects are not always owing to electronic effect, but, at least in the present case, to morphological effect or the others, and this must be important to design composite materials with high-level photocatalytic activity.

Acknowledgement

This work was financially supported by the Research Professional Development Project Under the Science Achievement Scholarship of Thailand (SAST). The analyses of photocatalyst particles were carried out using FE-SEM and STEM at the OPEN FACILITY, Hokkaido University Sousei Hall. We would also particularly like to thank Ms. Haruna Hori and Ms. Maya Endo for their valuable technical assistance and helpful suggestions.

References

[1] D. Ke, T. Peng, L. Ma, P. Cai, K. Dai, Effects of hydrothermal temperature on the microstructures of $BiVO_4$ and its photocatalytic O_2 evolution activity under visible light, Inorg. Chem. 48 (2009) 4685–4691.

[2] Z. Zhang, W. Wang, M. Shang, W. Yin, Photocatalytic degradation of rhodamine B and phenol by solution combustion synthesized $BiVO_4$ photocatalyst, Catal. Commun. 11 (2010) 982–986.

[3] D. Spasiano, R. Marotta, S. Malato, P. Fernandez-Ibañez, I. Di Somma, Solar photocatalysis: materials reactors, some commercial, and pre-industrialized applications. A comprehensive approach, Appl. Catal. B: Environ. 170 (2015) 90–123.

[4] T. Hisatomi, J. Kubota, K. Domen, Recent advances in semiconductors for photocatalytic and photoelectrochemical water splitting, Chem. Soc. Rev. 43 (2014) 7520–7535.

[5] A. Fujishima, T.N. Rao, D.A. Tryk, Titanium dioxide photocatalysis, J. Photochem. Photobiol. C: Photochem. Rev. 1 (2000) 1–21.

[6] T. Saison, N. Chemin, C. Chanéac, O. Durupthy, V. Ruaux, L. Mariey, F. Maugé, P. Beaunier, J.-P. Jolivet, Bi_2O_3, $BiVO_4$, and Bi_2WO_6: impact of surface properties on photocatalytic activity under visible light, J. Phys. Chem. C 115 (2011) 5657–5666.

[7] D. Kang, Y. Park, J.C. Hill, K.-S. Choi, Preparation of Bi-based ternary oxide photoanodes $BiVO_4$, Bi_2WO_6, and $Bi_2Mo_3O_{12}$ using dendritic Bi metal electrodes, J. Phys. Chem. Lett. 5 (2014) 2994–2999.

[8] J.K. Cooper, S. Gul, F.M. Toma, L. Chen, P.-A. Glans, J. Guo, J.W. Ager, J. Yano, I.D. Sharp, Electronic structure of monoclinic $BiVO_4$, Chem. Mater. 26 (2014) 5365–5373.

[9] A. Kudo, K. Omori, H. Kato, A novel aqueous process for preparation of crystal form-controlled and highly crystalline $BiVO_4$ powder from layered vanadates at room temperature and its photocatalytic and photophysical properties, J. Am. Chem. Soc. 121 (1999) 11459–11467.

[10] J. Su, L. Guo, N. Bao, C.A. Grimes, Nanostructured $WO_3/BiVO_4$ heterojunction films for efficient photoelectrochemical water splitting, Nano Lett. 11 (2011) 1928–1933.

[11] M. Yao, M. Liu, L. Gan, F. Zhao, X. Fan, D. Zhu, Z. Xu, Z. Hao, L. Chen, Monoclinic mesoporous $BiVO_4$: synthesis and visible-light-driven photocatalytic property, Colloids Surf. A Physicochem. Eng. Asp. 433 (2013) 132–138.

[12] T.S. Sinclair, B.M. Hunter, J.R. Winkler, H.B. Gray, A.M. Muller, Factors affecting bismuth vanadate photoelectrochemical performance, Mater. Horiz. 2 (2015) 330–337.

[13] J.A. Seabold, K.-S. Choi, Efficient and stable photo-oxidation of water by a bismuth vanadate photoanode coupled with an iron oxyhydroxide oxygen evolution catalyst, J. Am. Chem. Soc. 134 (2012) 2186–2192.

[14] M. Xie, X. Fu, L. Jing, P. Luan, Y. Feng, H. Fu, Long-lived, visible-light-excited charge carriers of $TiO_2/BiVO_4$ nanocomposites and their unexpected photoactivity for water splitting, Adv. Energy Mater. 4 (2014) 1300995.

[15] D. Lv, D. Zhang, X. Pu, D. Kong, Z. Lu, X. Shao, H. Ma, J. Dou, One-pot combustion synthesis of $BiVO_4/BiOCl$ composites with enhanced visible-light photocatalytic properties, Sep. Purif. Technol. 174 (2017) 97–103.

[16] F. Amano, K. Nogami, R. Abe, B. Ohtani, Preparation and characterization of bismuth tungstate polycrystalline flake-ball particles for photocatalytic reactions, J. Phys. Chem. C 112 (2008) 9320–9326.

[17] A. Kudo, S. Hijii, H_2 or O_2 evolution from aqueous solutions on layered oxide photocatalysts consisting of Bi^{3+} with $6s^2$ configuration and d^0 transition metal ions, Chem. Lett. 28 (1999) 1103–1104.

[18] X. Zhang, Y. Gong, X. Dong, X. Zhang, C. Ma, F. Shi, Fabrication and efficient visible light-induced photocatalytic activity of $Bi_2WO_6/BiVO_4$ heterojunction, Mater. Chem. Phys. 136 (2012) 472–476.

[19] S. Chaiwichian, B. Inceesungvorn, K. Wetchakun, S. Phanichphant, W. Kangwansupamonkon, N. Wetchakun, Highly efficient visible-light-induced photocatalytic activity of $Bi_2WO_6/BiVO_4$ heterojunction photocatalysts, Mater. Res. Bull. 54 (2014) 28–33.

[20] S. Xue, Z. Wei, X. Hou, W. Xie, S. Li, X. Shang, D. He, Enhanced visible-light photocatalytic activities and mechanism insight of $BiVO_4/Bi_2WO_6$ composites with virus-like structures, Appl. Surf. Sci. 355 (2015) 1107–1115.

[21] P. Ju, Y. Wang, Y. Sun, D. Zhang, Controllable one-pot synthesis of a nest-like $Bi_2WO_6/BiVO_4$ composite with enhanced photocatalytic antifouling performance under visible light irradiation, Dalton Trans. 45 (2016) 4588–4602.

[22] P. Ju, P. Wang, B. Li, H. Fan, S. Ai, D. Zhang, Y. Wang, A novel calcined $Bi_2WO_6/BiVO_4$ heterojunction photocatalyst with highly enhanced photocatalytic activity, Chem. Eng. J. 236 (2014) 430–437.

[23] H. Fan, D. Wang, Z. Liu, T. Xie, Y. Lin, Self-assembled $BiVO_4/Bi_2WO_6$ microspheres: synthesis, photoinduced charge transfer properties and photocatalytic activities, Dalton Trans. 44 (2015) 11725–11731.

[24] L. Chen, D. Meng, X. Wu, A. Wang, J. Wang, M. Yu, Y. Liang, Enhanced visible light photocatalytic performances of self-assembled hierarchically structured $BiVO_4/Bi_2WO_6$ heterojunction composites with different morphologies, RSC Adv. 6 (2016) 52300–52309.

[25] H. Hori, M. Takase, F. Amano, B. Ohtani, Mechanism of the formation of hierarchical-structured bismuth tungstate photocatalyst particles through counter-flow supply of bismuth and tungsten sources, Chem. Lett. 44 (2015) 1723–1725.

[26] H. Hori, M. Takase, M. Takashima, F. Amano, T. Shibayama, B. Ohtani, Mechanism of formation, structural characteristics and photocatalytic activities of hierarchical-structured bismuth-tungstate particles, Catal. Today (2017).

[27] B. Ohtani, Preparing articles on photocatalysis—beyond the illusions misconceptions, and speculation, Chem. Lett. 37 (2008) 216–229.

[28] A.K. Bhattacharya, K.K. Mallick, A. Hartridge, Phase transition in $BiVO_4$, Mater. Lett. 30 (1997) 7–13.

[29] A. Nitta, M. Takase, M. Takashima, N. Murakami, B. Ohtani, A fingerprint of metal-oxide powders: energy-resolved distribution of electron traps, Chem. Commun. 52 (2016) 12096–12099.

[30] J. Zhang, T. Wang, X. Chang, A. Li, J. Gong, Fabrication of porous nanoflake $BiMO_x$ (M = W, V, and Mo) photoanodes via hydrothermal anion exchange, Chem. Sci. 7 (2016) 6381–6386.

[31] B. Ohtani, O.O. Prieto-Mahaney, D. Li, R. Abe, What is Degussa (Evonik) P25? Crystalline composition analysis, reconstruction from isolated pure particles and photocatalytic activity test, J. Photochem. Photobiol. A: Chem. 216 (2010) 179–182.

[32] X. Lin, F. Huang, J. Xing, W. Wang, F. Xu, Heterojunction semiconductor $SnO_2/SrNb_2O_6$ with an enhanced photocatalytic activity: the significance of chemically bonded interface, Acta Mater. 56 (2008) 2699–2705.

[33] Q. Jia, A. Iwase, A. Kudo, $BiVO_4$-Ru/$SrTiO_3$:Rh composite Z-scheme photocatalyst for solar water splitting, Chem. Sci. 5 (2014) 1513–1519.

[34] B. Ohtani, O.-O. Prieto-Mahaney, F. Amano, N. Murakami, R. Abe, What are titania photocatalysts?—An exploratory correlation of photocatalytic activity with structural and physical properties, J. Adv. Oxid. Technol. 13 (2010) 247–261.

[35] J. Yu, A. Kudo, Effects of structural variation on the photocatalytic performance of hydrothermally synthesized $BiVO_4$, Adv. Funct. Mater. 16 (2006) 2163–2169.